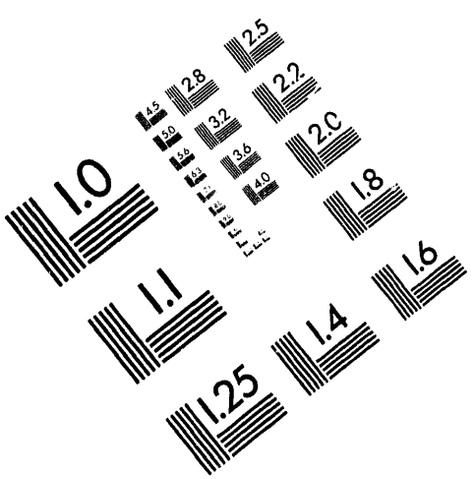
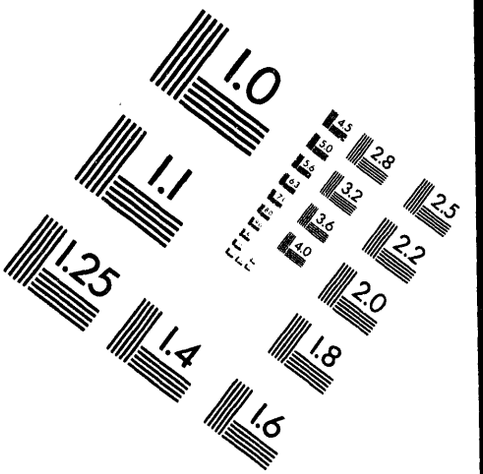

Association for Information and Image Management
1100 Wayne Avenue, Suite 1100
Silver Spring, Maryland 20910
301/587-8202

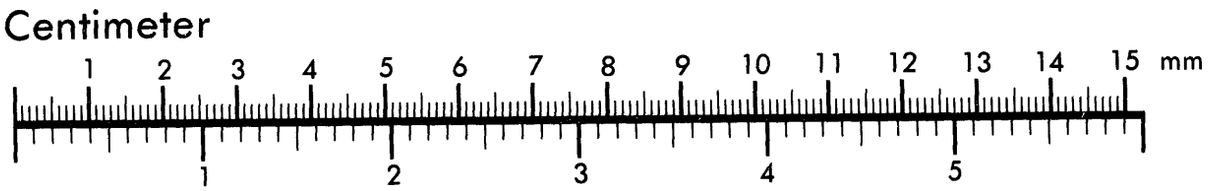

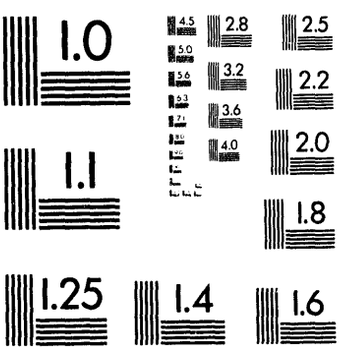

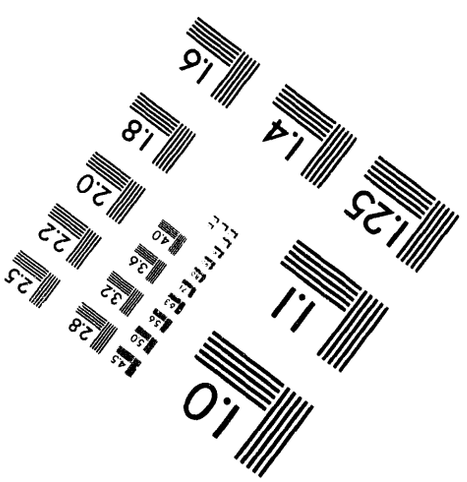
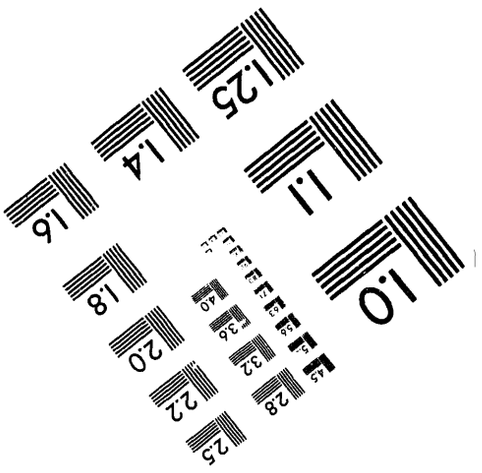

MANUFACTURED TO AIIM STANDARDS
BY APPLIED IMAGE, INC.

1 of 1

92PC92104-TPR-6

ADVANCED THERMALLY STABLE JET FUELS

Technical Progress Report
October 1993 - December 1993

H.H. Schobert, S. Eser, C. Song, P.G. Hatcher, P.M. Walsh, M.M. Coleman

Contributions from:

J. Bortiatynski, D. Clifford, R. Dutta, L. Hou, J. Li, D. McKinney, P. Sanghani, A. Schmitz, L. Selvaraj, M. Sobkowiak, J. Stallman, and J. Yu

January 1994

Prepared for U.S. Department of Energy
under
Contract No. DE-FG22-92PC92104

OBJECTIVES

The Penn State program in advanced thermally stable coal-based jet fuels has five broad objectives: 1) development of mechanisms of degradation and solids formation; 2) quantitative measurement of growth of sub-micrometer and micrometer-sized particles suspended in fuels during thermal stressing; 3) characterization of carbonaceous deposits by various instrumental and microscopic methods; 4) elucidation of the role of additives in retarding the formation of carbonaceous solids; and 5) assessment of the potential of production of high yields of cycloalkanes by direct liquefaction of coal.

SUMMARY

A study of the behavior of *n*-tetradecane was extended to examine the effects of initial phase behavior on its thermal degradation. It is possible that supercritical phenomena near the critical point, such as large partial molar volume, local anisotropy, and high compressibility, have significant effects on the thermal reactions.

Emphasis of studies of incipient deposition was shifted to the formation of deposits on the vertical walls of the reactor, by direct deposition of reactive species. Comparison of the particle formation rate per unit of particle surface area for suspended particles and particles on reactor walls showed that these rates were approximately the same, suggesting that similar species and reactions might be involved in both processes.

Filamentous carbon and fibrous carbon were detected on nickel and copper surfaces respectively, which may be a result of the catalytic effects of these metal surfaces. A common feature of carbon deposit on all metal surfaces studies was found to be the circular or oval ring structure, which is probably related to the further growth of deposit on previously formed carbon deposit surfaces. For nickel, and only nickel, the deposit produced from JP-8C is covered by another glassy layer of material. The formation of this glassy layer suggests that nickel is involved in the thermal degradation chemistry.

Infrared studies indicate that during the thermal degradation of dodecane the formation of alkenes occurs, followed by subsequent cyclization, aromatization, and condensation. In dodecane, aromatic species are directly derived from the parent hydrocarbon upon thermal stressing. Infrared studies have now been supplemented by proton nuclear magnetic resonance and gas chromatography / mass spectrometry to help develop mechanistic ramifications.

Carbon-13 nuclear magentic resonance was used to follow the decomposition of bibenzyl and benzyl alcohol and the formation of toluene in thermal stressing. No other ^{13}C labelled reaction products were detected in 24 h. Had any high-molecular-weight aromatics formed from bibenzyl, they would have implicated the reactive benzylic radical as a precursor to the formation of carbonaceous solid deposits. It was determined that the benzylic radicals instead acted as hydrogen scavengers and were capped to form toluene as the only significant product.

In the hydrogenation of Dammar resin, the low-molecular-weight dimers and trimers of cadinene start to crack into naphthalenes and benzenes. At long reaction times, undesirable recombination reactions occur, but the low-molecular-weight fraction has been almost totally converted to compounds that can be upgraded to cycloalkanes. The polymeric fraction of the resin is converted to dimethylnaphthalene and cadinane.

Several parameters concerning the alkylation of naphthalene have been investigated. Future work on this reaction will be extended to biphenyl.

TECHNICAL PROGRESS

Task 1. Investigation of the Quantitative Degradation Chemistry of Fuels

Effects of Initial Phase Behavior on the Thermal Degradation of n-Tetradecane (Contributed by Jian Yu and Semih Eser)

Introduction

The future fuel systems in advanced aircraft may be operating under supercritical conditions because of the increased thermal management requirements. It is clear that the thermal decomposition behavior of jet fuels under supercritical conditions must be understood to develop advanced thermally stable jet fuels. Considering that jet fuels consist of hundreds of compounds and that the thermal degradation behavior of single compounds under supercritical conditions is not well understood, a study of the behavior of selected model compounds and their mixtures should precede studying the thermal reactions of jet fuels under supercritical conditions.

n-Tetradecane is selected as a model compound since it is one of the major paraffins present in petroleum-derived jet fuels and its critical properties (419.15 °C, 15.73 bar [1]) are comparable with those of jet fuels (*e.g.*, 405 °C, 21 bar for JP-7 [2]). This report presents preliminary results on the effect of initial phase behavior on the thermal degradation of *n*-tetradecane.

Experimental

n-Tetradecane was obtained from Aldrich with 99+% purity and was used as received. The thermal stressing experiments were carried out in tubing bomb reactors for 5 hours. Three temperatures (400 °C, 425 °C, 450 °C) and six loading ratios, defined as the ratio of initial sample volume to reactor volume, were used to cover different phase conditions (liquid, gaseous, and supercritical, all referring to initial phase condition). After being loaded with a certain amount of sample, the reactor was sealed and purged with nitrogen at 6.9 MPa for five times to remove oxygen dissolved in the sample and final head space nitrogen pressure was maintained close to atmosphere to simplify analysis of phase behavior at reaction conditions. The reactor was then placed into a fluidized sand bath preheated to a desired temperature. After 5 hours the reactor was removed from the sand bath and quenched in cool water. The gaseous, liquid, and solid products were then collected as quantitatively as possible.

Liquid products were analyzed quantitatively using an Hewlett Packard GC with an FID detector. The column temperature was programmed from 40 °C to 280 °C at the rate of 4 °C/min with an initial isothermal period of 5 min at 40 °C and a final isothermal period of 10 min at 280 °C.

The compounds in the liquid products were identified using an Hewlett Packard GC interfaced with an HP mass selective detector.

Results and Discussion

1. Phase Behavior Calculations. It is important to understand the effects of phase behavior on thermal decomposition reactions. As soon as the thermal reactions start, the original reactant is converted into a complex mixture. It is, therefore, difficult to calculate the phase behavior of the reaction mixture. In this work, the initial phase behavior was estimated by calculating the initial pressure at any given temperature and sample loading using Soave-Redlich-Kwong equation of state (SRK EOS) [3]. SRK EOS has a high accuracy for predicting phase behavior of hydrocarbons. It works well at high pressures such as those under supercritical conditions. For pure compounds, SRK EOS can be expressed as follows:

$$P = RT / (V - b) - a / [V(V+b)] \quad (1)$$

where

$$b = 0.08664\, RT_c / P_c \quad (2)$$

$$a = a_c \alpha \quad (3)$$

$$ac = 0.42748\, (RT_c)^2 / P_c \quad (4)$$

$$\alpha^{0.5} = 1 + m\,(1 - T_r^{0.5}) \quad (5)$$

$$m = 0.48 + 1.574\,\omega - 0.176\,\omega^2 \quad (6)$$

where T_c is the critical temperature, P_c is the critical pressure, T_r, is the reduced temperature (T / T_c), and ω is the acentric factor.

Figures 1, 2, and 3 show the relationships between calculated reduced pressure P_r (P / P_c) and loading ratio r at three different temperatures. Since 400 °C is lower than the critical temperature of *n*-tetradecane, saturated vapor pressure was first calculated and Equation 1 was expressed in cubic form with respect to molar volume V. The resulted equation was solved using a FORTRAN subroutine CUBIC to get three roots for V's. The largest root corresponds to the molar volume of the saturated vapor V_v^{sa} and the smallest root corresponds to the molar volume of the saturated liquid V_l^{sat}. At r between the value corresponding to V_v^{sat} and the value corresponding to V_l^{sat} P_r is equal to P_r^{sat}.

2. Effects of Initial Phase Behavior on Conversion. Figures 4, 5, and 6 show the effect of the initial phase behavior on the conversion of n-tetradecane stressed at three different temperatures for 5 hours. At 400 °C the *n*-tetradecane conversion first increases, reaches a maximum, and then decreases with r. The initial phase of the reactant changes from a vapor phase through a vapor-liquid phase and to a liquid phase as the loading ratio increases. It seems that the effect of pressure on the *n*-tetradecane conversion is different depending on the phase in which the initial reactions take place.

At 425 °C (T_r = 1.008) the relationships between the *n*-tetradecane conversion and the loading ratio are more complicated. Since the initial phase changes from a gas phase to a supercritical phase, the conversion was plotted against P_r. It is found that conversion curve is much more complicated at the near-critical region than that in the gas phase and the far-supercritical region. At 450 °C (Tr = 1.045) the conversion curve also shows an unusual behavior at the near-critical region. While detailed mechanism governing this behavior is not yet clear, it is possible that supercritical phenomena near the critical point, such as large partial molar volume, local anisotropy, and high compressibility, have significant effects on the thermal reactions.

3. Effects of Initial Phase Behavior on Product Distribution. Figure 7, 8, and 9 show the effect of initial phase behavior on the overall mole ratio of C_5–C_{13} *n*-alkanes to the corresponding 1-alkenes. In all three cases products contain more n-paraffins than 1-alkenes. At 400 °C the mole ratio increases from 1 to around 3 as the loading ratio increases. At 425 °C the higher *n*-alkane selectivity is reached with a maximum in *n*-alkane selectivity at the near-critical region. The *n*-alkane selectivity at 450 °C is even higher and also exhibits a maximum at near-critical region. The higher *n*-alkane selectivity is due to relatively high pressure used in the present study. At high pressures, bimolecular reactions such as hydrogen abstraction, radical addition, and radical recombination are favored over the unimolecular radical decomposition. These bimolecular reactions will give higher paraffins as primary reaction products. When the *n*-alkanes/1-alkenes mole ratio curves at 425 °C and at 450 °C are compared with the corresponding *n*-tetradecane conversion curves, one will find that the mole ratio curve and conversion curve have similar shapes although the tendency of change with Pr is contrary. It is not clear whether these phenomena are typical. Since the critical conditions will change with chemical reactions and the critical properties of the reaction products after 5 hour reaction will be much different from those of the original reactant, it is surprising that the unusual behavior of both *n*-alkanes/1-alkenes mole ratio and *n*-tetradecane conversion can be correlated to the initial critical point. Future work will be focused on initial reactions to avoid large changes in the critical properties.

References

1. Teja, A. S., Lee, R. J., Rosenthal, D., and Anselme, M., Fluid Phase Equili., 56, 153, **1990.**
2. Schobert, H. H., Eser, S., Song, C., Hatcher, P. G., Walsh, P. M., and Coleman, M. M., Advanced Thermally Stable Jet Fuels, Technical Progress Report (July 1993 - September 1993), December **1993,** The Pennsylvania State University.
3. Soave, G., Chem. Eng. Sci., 27, 1197, **1972.**

Task 2. Investigation of Incipient Deposition

Growth and Deposition of Particles During Heating of Coal-Derived Aviation Gas Turbine Fuels (Contributed by Peter M. Walsh and Prashant C. Sanghani)

Previous work under this task has been focussed on the growth and deposition of suspended particles during thermal stressing of coal-derived fuel and mixtures of coal-derived fuel with tetradecane. During the period under review the emphasis was shifted to the formation of deposits on the vertical walls of the reactor, by direct deposition of reactive species. Comparison of the particle formation rate per unit of particle surface area with the deposition rate per unit of wall area showed that these rates were approximately the same, suggesting that similar species and reactions might be involved in both processes. If that were so, then the wall and suspended particles would compete for the same pool of reactive species. Sufficient data have been accumulated to begin the development of a global kinetic scheme for quantitative description of the factors controlling solid formation.

The mechanism is shown schematically in Figure 10. Precursors in the fuel are assumed to form reactive intermediates which deposit on the surfaces of the reactor and on the surfaces of suspended particles. The reactive intermediates also react with hydrogen donors to form stable products. Let F, R, H, D, and S represent the precursors, intermediates, hydrogen donors, deposits, and surface, respectively. The vapor species are present at concentrations expressed in kg/m^3; the deposit loading is specified in kg/m^2, and the wall surface area has units of m^2. For the present we ignore the particles, because the total amount of material forming particles and settling to the bottom of the reactor is small, although the deposition rate per unit area on the bottom is greater than on the vertical walls. The reactions are:

$F \xrightarrow{k_f} R$	formation of reactive species
$R + H \xrightarrow{k_h}$ stable products	hydrogenation of reactive species
$R + S \xrightarrow{k_s} D$	addition of reactive species to surface

The equations to be solved are then:

$$\frac{dF}{dt} = - k_f F$$

$$\frac{dR}{dt} = k_f F - k_h R H - k_s R S$$

$$\frac{dH}{dt} = - k_h R H$$

$$\frac{dD}{dt} = k_s R$$

The boundary conditions are $F = F_0$, $R = 0$, $H = H_0$, and $D = 0$ at $t = 0$.

Measurements of deposits formed on the vertical walls of the 20 mL batch reactor from mixtures containing 81.5 wt% JP-8C and 18.5 wt% tetradecane are shown as a function of time in Figure 11. The mixtures were treated at 450°C under nitrogen initially at 100 psi. The rate equations were integrated numerically using the following experimental data:

initial mass fraction of tetradecane, $F_0 = 0.202$ (includes the amount in neat JP-8C)
initial mass fraction hydrogen donors, $H_0 = 0.2644$ (substituted and unsubstituted tetralins and decalins)
density of vapor in the reactor, 400 kg/m^3
rate coefficient for disappearance of tetradecane, $k_f = 1.1 \times 10^{-4}$ s^{-1}

The rate coefficients for destruction of intermediates were adjusted to fit the measurements:

rate coefficient for hydrogenation of intermediates, $k_h = 5 \times 10^{-7}$ m^3/kg s
rate coefficient for deposition of intermediates, $k_s = 3.5 \times 10^{-8}$ m/s

The results of the calculation are shown as the curve in Figure 11. Although the profile exhibits an induction period, during which the pool of intermediates is building up to a steady value, it is much less pronounced than the observed induction period. In the simple mechanism each molecule of tetradecane which disappears produces a reactive intermediate. Because the steady concentration of intermediates is small and the rate of decomposition of tetradecane relatively fast, the calculated concentration of intermediates reaches the steady value very quickly. Not surprisingly, it appears that a more detailed mechanism will be needed to accurately describe the behavior of the system at short times. Formation and growth of particles is expected to have some influence on the direct addition of reactive species to deposits.

Task 3. Characterization of Solid Gums, Sediments, and Carbonaceous Deposits.

Carbonaceous Deposit Formation on Metal Foils from Thermal Stressing of Coal Derived Jet Fuels (JP-8C) (Contributed by J. Li and S. Eser)

Introduction

Our previous work indicated that the deposit formation from dodecane thermal stressing on a metal surface might be a two-step process: an initial catalytic deposition step on some clean metal surfaces and a subsequent deposition step on the previously formed deposit surface [1]. Filamentous carbon and fibrous carbon were detected on nickel and copper surfaces respectively, which may be as a result of the catalytic effects of these two metal surfaces in the system. Meanwhile, a common feature of carbon deposit on all the metal surfaces studied was found to be the circular or oval ring structure, which is probably related to the further growth of deposit on previously formed carbon deposit surface. In this work, a coal-derived jet fuel, JP-8C, was studied. The proposition of a two-step deposition process on metal surfaces is tested.

Experimental

The thermal stressing of JP-8C was conducted isothermally in 20 mL stainless steel (316) tubing bomb reactors heated in a fluidized sand bath. A 5 mL sample was used for all the tests. The sample was deoxygenated by repetitive pressurization and purging (at least 5 times) with ultra-high purity (UHP) nitrogen, and left with 0.69 MPa (100 psi) UHP N_2 as the initial pressure. At the end of the reaction, the reactor was quenched with cold water.

Ni, Cu, Al, Ti, and stainless steels 304 (Fe / Cr 18 / Ni 10), 316 (Fe / Cr 18 / Ni 8 / Mo 3), and 321 (Fe / Cr 18 / Ni 8 / Ti) foils were used as the substrate surface. The foils were 0.05 mm thick except Cu foils which had a thickness of 0.025 mm. They were cut into coupons of 5 mm wide, and 10, 15, 20 and 30 mm long. The coupons were cleaned with acetone in an ultrasonic bath

for 20 minutes, then dried and weighed. For each run, two coupons (5 x 10 and 5 x 20 mm) were hung on top of the reactor just below the reducer by a fine aluminum wire, and another two coupons (5 x 15 and 5 x 30 mm) were placed at the bottom of the reactor. After the reaction, coupons deposited with carbonaceous materials were rinsed with hexane, dried and weighed. Carbon morphologies were studied with an ISI DS 130 duel stage scanning electron microscope in the Materials Research Institute (MRI) at Penn State.

Observations and Discussion

1. Carbon deposition on nickel surface. After 3 hours reaction, nickel surfaces both on top and at the bottom of the reactor are covered by deposit which has a honey comb shape (Fig. 12). Under the SEM microscope, this deposit is difficult to focus. It is very likely that the deposit is coated with a glassy layer of carbonaceous material. After 5 hours reaction, deposit as well as the glassy layer are greatly thickened. The honey comb-like deposit is mostly filled to become rough on the surface (Fig. 13a and Fig. 13b). For deposit on the top nickel surface, there are lots of sticky deposit particles scattered on the glassy layer (Fig. 13a). In contrast, there is no such sticky deposit particles on the glassy layer at the bottom nickel surface (Fig. 13b).

The occurrence of the glassy layer is unique to the carbon deposition from JP-8C on a nickel surface. This layer apparently does not dissolve in hexane. The fact that no such layer exists on other metal surface indicates that a nickel surface can not only affect the deposition process itself, but also alter the chemistry that leads to the deposition formation.

2. Carbon deposition on titanium, aluminum, and copper surfaces. After 3 hours reaction, there is no carbon deposit seen on any of these metal surfaces. After 5 hours reaction, thick deposit layers can be seen on both top and bottom metal surfaces. The carbon deposit on titanium (Fig. 14) and copper (Fig. 15) is bulky with random cracks. In contrast, deposit on aluminum surface is also bulky but with regular straight strips (Fig. 16). For all top metal surfaces, there is an extra layer of particulate carbon (about 1 μ in diameter) loosely coalesced or aggregated to each other scattered on the bulky layer (Figs. 14a, 15a, and 16a). This particulate carbon layer is not seen on the bottom metal surfaces (Figs. 14b, 15b, and 16b).

3. Carbon Deposition on Stainless Steel Surfaces. Three different stainless steel foils (304, 316, 321) are used in the experiments. No deposits are seen on any of the surface after 3 hours reaction. After 5 hours reaction, morphologies of the deposit are similar to those found on Ti, Al, and Cu surfaces. On the bottom coupon surfaces, deposit is very smooth, and bulky with random cracks (Figs. 17b, 18b, and 19b). On top coupon surfaces, there is also an extra layer of porous particulate carbon on the smooth bulky carbon layer (Figs 18a and 19a). On top 304 stainless steel coupon surface, however, the bulky deposit layer is not flat (Fig. 17a). The

particulate carbon is much larger than that seen on the other top surfaces and seems to have grown from the bulky deposit layer.

4. Discussion. Thermal stressing experiments using coal-derived jet fuel JP-8C have shown different features from those obtained from the dodecane experiments. JP-8C is generally more stable than dodecane. Deposition occurs only after 3 hours of thermal stressing for JP-8C. For nickel and only on nickel surfaces, deposit is covered by another glassy layer of material. The formation of this glassy layer material suggests that nickel is involved in the thermal degradation chemistry. As for the other metal surfaces, it is consistently seen that deposit on bottom surfaces is a smooth, bulky layer. However, deposit on the top surfaces has the smooth, bulky carbon layer plus a loose particulate carbon layer. This is probably due to a phase separation existed between the top and the bottom of the reactor.

References

1. H. H. Schobert, S. Eser, C. Song, P.G. Hatcher, P.M. Walsh, and M.M. Coleman, *Advanced Thermally Stable Jet Fuels*, Technical Progress Report, 92PC92104-TPR-5, December, 1993

Task.4 Coal-based Fuel Stabilization Studies

Thermal stability studies Using the Model compound Dodecane (Contributed by Leena Selvaraj, Maria Sobkowiak, John B. Stallman, Chunshan Song and Michael M. Coleman)

Introduction

This study is in continuation of the work from the earlier quarterly report[1]. We have already reported the results obtained on FTIR and GC analysis of the effect of the additive benzyl alcohol on the model compound dodecane during pyrolysis. FTIR studies indicate that during the thermal degradation of dodecane the formation of alkenes occurs followed by subsequent cyclization, aromatization and condensation. In the case of the dodecane experiments aromatic species are directly derived from the parent hydrocarbon upon thermal stressing (in contrast, analogous studies on "pure" jet A-1 fuel are complicated because aromatic species are present in the jet fuel)[2]. Parallel ^{1}H NMR studies were performed to assist in the interpretation of the changes observed in the infrared spectra as a function of thermal stressing. GC-MS studies were performed on the liquid samples to gain insight on the components of the liquid sample. In this report the ^{1}H NMR and the GC-MS data are discussed and, finally, we will summarize our conclusions and consider the mechanistic ramifications of our results.

Experimental

Thermal stressing of pure dodecane and dodecane mixtures containing 5%(v/v) benzyl alcohol mixtures were performed as a function of time on 10 mL samples at 425°C in 15 mL type 316 stainless steel micro-reactors[2] under 100 psi (0.69 MPa) of air. The micro-reactor containing the sample was purged with UHP-grade N_2 five times at 1000 psi (6.9 MPa) to minimize the presence of dissolved oxygen and finally pressurized with 100 psi (0.69 MPa) of air. It was then placed in a preheated sand bath at 425°C for the required reaction time, followed by quenching into cold water and then it was depressurized and the liquid sample was collected and used for analysis.

Samples for NMR analysis were prepared as 50% solutions in deuterated chloroform ($CDCl_3$ 99.96%D - Cambridge Isotopes Laboratory). Spectra were recorded on a Brucker WP200 instrument at a field strength of 200 MHz. A Hewlett Packard GC with mass selective detector was used for the GC-MS analysis. The temperature programme used was as follows: initial temperature: 40°C, initial isothermal holding time: 5 min, heating rate of 4°C/min to 280°C, and the final isothermal holding time 10 min. The split mode of injection was used.

Thermal Stressing of Neat Dodecane and Dodecane / Benzyl Alcohol Mixtures at 425°C.

^1H NMR Studies: The liquid sample was used for this study. Olefinic protons resonate between 6 and 4.5 ppm and this region can be very useful to monitor the formation and elimination of olefinic bonds. Figure 1 shows ^1H NMR spectra (6–4.5 ppm, all scale- expanded to the same degree) of dodecane thermally stressed under air for periods of 0, 20 min, 1, 3, 6, 12, 18 hours at 425° C. NMR resonances that can be attributed to internal and external alkenes are obvious and, in common with the infrared results, the concentration of alkenes appears to maximized at approximately 6 hours. Figure 21 shows ^1H NMR spectra (6– 4.5 ppm) of dodecane-benzyl alcohol mixtures thermally stressed under air after period of 0, 1, 3, 6, 12 and 18 hours. The trends observed for the olefinic resonances are consistent with those seen in the infrared results. More stimulating, however, is the fact that benzyl alcohol has a convenient characteristic resonance at 4.74 ppm attributable to benzylic protons. In the unstressed sample the spectrum is dominated by this intense line. Significantly, the intensity of this line at 4.74 ppm decreases as a function of thermal stressing, which verifies that benzyl alcohol is being consumed, but is still detected in the spectrum recorded after 6h at 425 °C. This implies that the benzyl alcohol is remarkably stable in the mixture and gradually transforms to benzylaldehyde (and other products) over a period in excess of 6h under air at 425° C. Furthermore, the amount of benzyl alcohol present after 12 h of thermal stressing at 425°C is insignificant. This, in turn, strongly suggests that as long as benzyl alcohol is present, the onset of the formation of carbonaceous solids is suppressed. These data are

strong supporting evidence to the results obtained from simple quantitative GC analyses of thermally stressed samples of dodecane and mixtures with benzyl alcohol as reported earlier.

GC-MS studies: All the liquid samples were qualitatively examined by GC-MS. The results obtained on stressing pure dodecane for 1, 3, 6, and 12h at 425°C indicate that in the first hour of stressing some cracking of dodecane to smaller alkanes and alkenes takes place. After stressing for 3h, alkylcycloalkanes are detected (predominantly alkylcyclohexanes and some alkylcyclopentanes). After stressing for 6h we begin to see C_2 to C_4 alkylbenzenes and some indane, in addition to alkylcyloalkanes and alkylcyclopentanes. This is illustrated in Figures 22(a) and 22(b) which show representative selective ion chromatograms (SIC) of ions m/z 83 and 105, respectively, obtained from samples of pure dodecane that had been stressed at 425°C for 6h. Fragment ions of m/z 83 are characteristic of alkylcyclohexanes and alkylcyclopentanes, while those of m/z 105 are characteristic of alkylbenzenes. After stressing for 12h we also observe the presence of alkylnaphthalenes. These results provide strong evidence that degradation of dodecane at 425°C proceeds as follows: initial cracking into lower alkanes and alkenes; cyclization reactions to form alkylcycloalkanes (and alkylcycloalkenes); dehydrogenation to form alkylbenzenes and finally condensation to form the polyaromatics that presumably result in the formation of carbonaceous solids. This result is consistent with the reaction pathways proposed in a recent study of solid formation from paraffinic jet fuels[3]. The analogous GC-MS results for the dodecane-benzyl alcohol (5% v/v) mixture that was stressed for 6h are shown in Figures 23(a) and 23(b). From the SIC corresponding to ions m/z 83 and 105, it is clear that in the presence of benzyl alcohol no significant amount of alkylcyclohexanes, alkyl cyclopentanes or alkylbenzenes are detected up to 6 h of thermal stressing at 425°C. 1-Octene is identified in the SIC (m/z 83) and the dominant peak in the SIC (m/z 105) is attributable to benzaldehyde—the byproduct of the oxidation of benzyl alcohol.

Mechanistic Implications: The mechanism that could explain the stabilization of dodecane by benzyl alcohol at temperatures above 400 °C is depicted in Scheme I. Thermolysis of dodecane initially leads to the generation of a secondary radical. In the presence of benzyl alcohol further reactions can follow either pathway A or pathway B. If pathway A is followed then the secondary radical could proceed, through a thermodynamically favored process, to abstract a benzylic proton from benzyl alcohol, thus regenerating the dodecane and producing a resonance stabilized benzylic radical. The O-H proton of the benzylic radical is then abstracted, probably via a second dodecane radical, to produce benzaldehyde. However, if pathway B is followed then the initially generated secondary radical could undergo a ß-scission to provide a terminal alkene and a primary radical. The primary radical would then abstract a benzylic proton from benzyl alcohol thereby regenerating a saturated hydrocarbon and the benzylic radical as discussed previously. Abstraction of an allylic proton from the terminal alkene produced from the ß-scission of dodecane would give an allylic

radical, which could either react with benzyl alcohol as before, or undergo further dissociative reactions. Consequently, we propose that benzyl alcohol has acted as a suicide free radical scavenger via proton donation during the thermal stressing of dodecane at 425 °C. Supporting evidence that benzyl alcohol donates hydrogen to the reaction system in the manner depicted above was obtained from studies using labelled dodecane which is reported earlier[1].

References

1. Technical Progress Report February 1993 -March 1993.
2. Coleman, M. M.; Selvaraj, L.; Sobkowiak, M. and Yoon, E., *Energy & Fuels*, **1992**, 6(5), 535.
3. Song, C.; Eser, S.; Schobert, H. H. and Hatcher, P. G., *Energy & Fuels*, **1993**, 7(2), 234.

Task 5. Exploratory Studies on the Direct Conversion of Coal to High Quality Jet Fuels.

1. The Thermal Decomposition of ^{13}C-Labeled Bibenzyl in the Presence of Additive Free Jet A-1 (Contributed by Lei Hou, David J. Clifford, Daniel E. McKinney, Jacqueline M. Bortiatynski, and Patrick G. Hatcher)

Introduction

Liquid fuels and the materials derived from them have been analyzed considerably by ^{13}C NMR in recent years due to improved instrumentation and analytical techniques. Cookson and Smith have reported the application of ^{13}C NMR to the study of numerous liquid fuels[1-10] such as petroleum, coal derived fuels, synthetic fuels, diesel fuels, jet fuels, and kerosene fuels. While high resolution ^{13}C NMR has been used to characterize liquid fuels, only McKinney et al.[11] has utilized the technique of ^{13}C labeling along with ^{13}C NMR to examine complex reactions that liquid fuels undergo when subjected to thermal stress. ^{13}C-labeling has been used to examine the reactivity of specific labeled molecules in complex organic systems[12-14].

From some of our recent studies involving the examination of a potential ^{13}C-labeled antioxidant,C-1 ^{13}C-labeled benzyl alcohol, along with studies involving the examination of the reactivity of pollutants such as 2,4-dichlorophenol with complex macromolecules such as humic substances, we have gained a great deal of expertise in the use of ^{13}C-labeled compounds to examine the reactivity of specific compounds in complex mixtures[11, 15]. Reactions involving the ^{13}C-labeled carbon leads to significant changes in the chemical shift of this carbon in ^{13}C NMR

spectra. By enriching a reactive compound with 100% ^{13}C at the one reactive site, a significant enhancement in the ^{13}C NMR sensitivity is realized for the labeled carbon. Other unlabeled carbons in the reactive molecule and the reacting substrate are reduced to near background levels in the spectra. Thus, reactions at or near the labeled site can be clearly differentiated from reactions of the unlabeled carbons.

This report along with a previous study[11], demonstrates the applicability of ^{13}C NMR labeling in combination with standard ^{13}C NMR experiments to examine thermally induced changes in a complex fossil fuel system, jet fuel. In this report, we have examined the reactivity of bibenzyl in the presence of a jet fuel under thermally stressed conditions. Previous model studies involving bibenzyl were used to characterize the reactions that resulting from benzyl radical species generated under coal liquefaction conditions[16-20]. Since benzylic radicals are also expected to be produced in the thermal stressing of jet fuel this study is a logical extension of the previous model studies. Using experimental conditions similar to those employed by McKinney et al.[11], we examined the fate of bibenzyl labeled with 100% ^{13}C at the two benzylic carbons with the expectation that any reactions involving these highly reactive labeled carbons could be clearly differentiated with ^{13}C NMR.

Experimental.

NMR Analysis. The ^{13}C NMR spectra were obtained on a Bruker WM 360 NMR spectrometer with a resonance frequency of 90.56 MHz. An inverse-gated pulse sequence with a 10 second delay between pulses, and a 45 ^{o} pulse angle was utilized to ensure the acquisition of quantitative spectral data. The spectral width used in these experiments was approximately 21 kHz, and 96 scans were collected for each experiment. The spectra were transformed using 1 Hz line broadening. The intense peaks in the spectra which result from the ^{13}C labeled carbons were identified using standard chemical shift tables[21]. The relative amount of each product present in the reaction mixture was obtained from the peak height of the ^{13}C labeled carbon.

Synthesis of Bibenzyl. Samples for this study were prepared from an essentially additive free Jet A-1 fuel supplied by the Air Force/ WRDC Aero Propulsion Laboratory (No. 90-POSF-2747). α, α-^{13}C-bibenzyl was synthesized using methods described by McMurry and Silvestri[22] (Scheme I). Titanium(III) chloride (2.3 g, 15.0 mmol) was weighed under N_2 in a glove bag and placed in a two-necked flask, equipped with a magnetic stir bar and 70 mL of dry dimethoxyethane under dry N_2. Quickly, $LiAlH_4$ (190 mg, 5.0 mmol) was added to the stirred solution. The resulting black suspension was stirred for 10 min. before use. 100% α-^{13}C-benzyl alcohol (0.52 mL, 5.0 mmol) in a few mL of dry dimethoxyethane was added to the solution and

refluxed for 16 hr. After cooling, the reaction mixture was quenched with dilute HCl followed by dilution with H_2O. The mixture was extracted with ether, and the ether extracts combined. The ether solution was washed with brine, dried ($MgSO_4$), filtered, and concentrated at the rotary evaporator. The resulting product, α, α-^{13}C-bibenzyl, was recrystallized, 78% yield, mp 52°C.

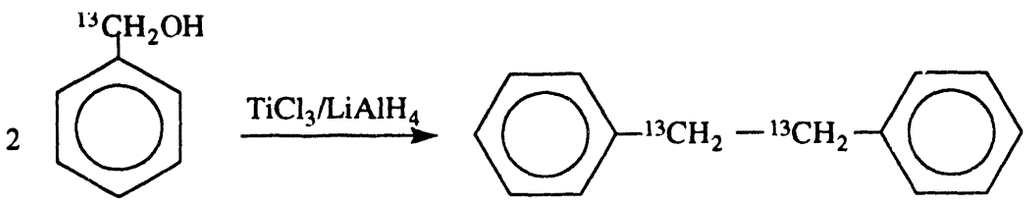

Scheme I

Thermal Stressing Experiments. The thermal stressing and sample preparations were carried out in similar fashion as that discussed by McKinney, et al.[11] with the following exception: 0.37 g of α, α-^{13}C-bibenzyl was added to 10 mL of jet fuel sample. It is important to mention that the bibenzyl still contained a small amount of unreacted benzyl alcohol. After each stressing period (10 min., 1 hr., 3 hrs., 6 hrs., 12 hrs., 24 hrs.), a 0.5 mL aliquot was removed and placed along with 0.5 mL of deuterated chloroform in an NMR tube and sealed. The reactor was resealed, repressurized and heated further until the next allotted time. This sampling process was administered in order to conserve the expensive ^{13}C-labeled material. Otherwise, larger volumes of the labeled material would have been needed in order to carry out a separate experiment for each thermal stressing period. Admittedly, if we had been attempting to mimic a real aircraft system, the reaction would have been performed differently. Because our purpose was to show the usefulness of the ^{13}C labeling approach, we deemed it unnecessary to completely mimic a natural system.

Results and Discussion

Figure XX displays the ^{13}C NMR spectra for the jet fuel sample laced with α, α-^{13}C-bibenzyl at time 0 hr., 1 hr., 6 hr., and 12 hr. From the examination of the spectrum obtained prior to thermal stressing (T = 0 hrs.) the most significant signals were due to the ^{13}C-labeled carbons of bibenzyl and benzyl alcohol which are located at approximately 38.2 ppm and 65.45 ppm, respectively. As the duration of the thermal stressing increases three important trends are observed. First, the concentration of benzyl alcohol decreases which is expected from the previously reported work found in McKinney et al. Second, the concentration of bibenzyl also decreases, and third, the concentration of toluene (21.4 ppm) in the reaction mixture increases. The graph of relative area vs heating time (425° C) for these three reactants is shown in Figure XX, and clearly displays the visible trends in the ^{13}C NMR spectra. Table XX contains the relative area of benzyl alcohol, bibenzyl, and toluene normalized to the area of one of the aliphatic

signals resulting from jet fuel. By normalizing the data in this manner, inconsistencies in sampling are corrected and the resulting areas can be compared from sample to sample.

Preliminary Conclusions

From the results of the ^{13}C NMR experiments were able to follow the decomposition of bibenzyl and benzyl alcohol and the formation of toluene as a result of thermal decomposition reactions. Throughout the course of the twenty-four hour experiment we were unable to detect the formation of any other ^{13}C-labeled reaction products. We were especially interested in the formation of high molecular weight aromatic compounds that may have been formed from the decomposition of the ^{13}C-labeled bibenzyl, which may have implicated the reactive benzylic radical as a precursor to the formation of carbonaceous solid deposits. However, no intense peaks could be noted in the aromatic region of the spectra, and therefore it was determined that the benzylic radicals acted as hydrogen scavengers and were capped to form toluene as the only significant product in the thermal stressing experiments.

References

1. Cookson, D. J. and Smith, B. E., *Org. Magn. Reson.* **1981**, 16 (2), 111-116.
2. Cookson, D. J. and Smith, B. E., *Fuel* **1982**, 61, 1007-1012.
3. Cookson, D. J. and Smith, B. E., *Fuel* **1983**, 62, 39-43.
4. Cookson, D. J. and Smith, B. E., *Fuel* **1983**, 62, 34-38.
5. Cookson, D. J. and Smith, B. E., *Fuel* **1983**, 62, 986-988.
6. Cookson, D. J. and Smith, B. E., *J. Magn. Reson.* **1984**, 57, 355-368.
7. Cookson, D. J. and Smith, B. E., *Anal. Chem.* **1985**, 57, 864-871.
8. Cookson, D. J., Latten, J. L., Shaw, I. M., and Smith, B. E., *Fuel* **1985**, 64, 509-519.
9. Cookson, D. J. and Smith, B. E., *Energy Fuels* **1987**, 1, 111-120.
10. Cookson, D. J. and Smith, B. E., *Energy Fuels* **1990**, 4, 152-156.
11. McKinney, D. E., Bortiatynski, J. M., and Hatcher, P. G., *Energy Fuels* **1993**, 7, 578-581.
12. Stothers, J. B. ^{13}C NMR Studies of Reaction Mechanisms and Reactive Intermediates. In *Topics in Carbon-13 NMR Spectroscopy*; Levy, G. C., Ed.; John Wiley & Sons: New York, 1974; vol.1, pp 229-279
13. McInnes, A. G., Walter, J. A., Wright, J. L. C., and Vining, L. C. ^{13}C NMR Biosynthetic Studies. In *Topics in Carbon-13 NMR Spectroscopy*; Levy, G. C., Ed.; John Wiley & Sons: New York, 1976; vol. 2, pp 125-179.

14. London, R. E. Carbon-13 Labeling Strategies in Macromolecular Studies: Application to Dihydrofolate Reductase. In *Topics in Carbon-13 NMR Spectroscopy*; Levy, G. C., Ed.; John Wiley & Sons: New York, 1984; vol. 4, pp 54-92.
15. Bortiatynski, J.M.; Hatcher, P.G.; Minard, R.D.; Dec, J. and Bollag J.M. *6th International Meeting of the International Humic Substances Society Abstracts*, **1992**, 293.
16. Virk, P. S., *Fuel*, **1979**, 58, 149-151.
17. Stein, S. E., *Fuel*, **1980**, 59, 900-901.
18. Petrocelli, F. P. and Klein, M. T., *Macromolecules*, **1984**, 17, 161-169.
19. Houser, T. J., Tsao, C., Dyla, J. E., Van Atten, M. K., and McCarville, M. E., *Fuel*, **1989**, 68, 323-327.
20. Camaioni, D. M., *J. Am. Chem. Soc.*, **1990**, 112, 9475-9483.
21. Breitmaier, E.; Voelter, W. "*Carbon-13 NMR Spectroscopy: high resolution methods and applications in organic chemistry and biochemistry* "; VCH Publishers: New York, **1987**
22. McMurry, J. E. and Silvestri, M., *J. Org. Chem.*, **1975**, 40, 2687.

2. Preliminary investigation into producing cycloalkanes from Dammar resin. (Contributed by Richard Dutta)

Introduction

One of the major reasons for the selection of the Blind Canyon coal for liquefaction is its high concentration of resinite. The resinite occurring in this coal is believed to exist as two fractions. One fraction consists of a high molecular weight polymer proposed to be that of polycadinene [1,2]. This structure is made up of substituted hydronaphthalene monomers that could be liberated upon liquefaction. The second fraction is composed of low molecular weight compounds shown by GC/MS to be dimers and trimers of cadinene and functionalized triterpenoids [3,4]. To optimize a process where cycloalkanes can be produced from resinite, it is necessary to study the reaction chemistry of the process. Due to the difficulty of obtaining enough resinite to carry out reactions, a suitable substitute has to be found that is commercially available in large quantities. Dammar resin has been shown to contain a polymer that is similar to that found in Utah resinite, and serves as a good model to study the liquefaction behavior of the resinite. The approach that will be taken in this investigation consists of, primarily, three tasks: (1) Preliminary investigation into behavior of dammar under conditions of liquefaction. (2) More detailed

investigation to ascertain the best conditions to produce bicyclic and monocyclic structures. (3) Hydrogenation of products to produce cycloalkanes.

This section of the report will discuss preliminary findings and also provide a foundation on which the following two tasks will follow.

Experimental

Dammar resin (obtained from Sigma Chemical Co.) was loaded into a 25mL tubing bomb reactor. The reactor was purged twice with nitrogen and then pressurized to 1000psi with hydrogen. Heating of the reactor was achieved using a fluidised sand bath. After reactions at 450°C and various times, the reactor was quenched and the products were extracted into hexane-solubles and -insolubles. This hexane-soluble fraction was analysed by GC/MS. Dammar resin was dissolved in methanol and the insoluble fraction separated by filtration. The soluble fraction was recovered by rotary evaporation. The methanol- insoluble fraction was liquefied for 60 minutes at 450°C as before.

Results

Figures 26-29 show the total ion chromatograms (TICs) of the hexane solubles from liquefaction of the whole dammar resin at 450° C for reaction times 10, 20, 40 and 60 minutes respectively. The major peak assignments are shown in Table 2.

The TICs can be broken up into four distinct sections:

1) RT 0-20 minutes. C_1–C_4 Benzenes.

2) RT 20-30 minutes. C_1–C_4 Indenes

3) RT 30-45 minutes. C_1–C_5 Naphthalenes/tetralins.

4) RT 60-80 minutes. Dimers and trimers of cadinene and other high molecular weight compounds.

After a reaction time of 10 minutes, peaks can be seen in all four sections. As time of reaction increases, the concentration of peaks in section 4 drops. After 40 minutes, all GC-amenable products that elute in section 4 are almost gone. Figure 30 shows qualitatively how the area percent of the TICs for each section changes with time. It can be seen that C_1–C_4 benzenes increase in concentration up to 40 minutes along with naphthalenes and indenes. Figure 29 shows the TIC of Dammar reacted for 60 minutes. The product distribution has changed significantly from that at 40 minutes. GC/MS identification of peaks show that C_2-biphenyl is being formed, as well as dimethylanthracene. This is in conjunction with a decrease seen in section 1 of the TIC. The concentration of toluene and other substituted benzenes has decreased in relation to other products. A thorough explanation at this stage of the investigation is difficult, but several possible ideas do emerge. The methylbenzenes could be reacting together to produce biphenyls. Dimethylanthracene can be produced by cracking of the large molecular weight dimers such as

bicadinane. These two reactions would only occur at high temperatures and long reaction times. The recombination reactions are undesirable, but cracking of the high molecular weight fraction of the resin is required if compounds are to be formed that can be upgraded to desirable cycloalkanes boiling in the jet fuel range. Scheme III shows a possible reaction mechanism (dashed arrows indicate product formation after one hour of reaction).

The TIC of the liquefied methanol insoluble fraction is shown in Figure 31. This fraction is the high molecular weight polymer, proposed to be polycadinene. Thermal stress causes the polymer to break down into monomeric, dimeric, trimeric and oligomeric cadinenes. Aromatization of the compounds released by depolymerization leads to the formation of cadalene via 1,6-dimethyl,4-isopropyltetralin. It has been reported previously that removal of the isopropyl group along with hydrogen atoms is possible under these conditions [5]. This is seen by the formation of dimethylnaphthalene in high concentration. Scheme IV shows a possible reaction mechanism of the depolymersiation reaction of polycadinene.

The formation of cadinane under these conditions can be explained in two ways. Cadinene released by depolymerisation reactions may hydrogenate to cadinane. Also, a cadinane moiety may exist in the polymeric structure, and upon release by depolymerisation, be thermally stable enough to resist dehydrogenation to cadinene and further, to dimethylnaphthalene. The second explanation is more likely under these conditions because hydrogenation to any great extent is less favorable than dehydrogenation, which is seen by the formation of dimethylnaphthalene.

Conclusions

Dammar resin consists of two fractions. If compounds are to be produced from dammar that can be upgraded to cycloalkanes, it is necessary to study the reactions of both fractions. The products that are seen in the reactions of the whole resin but not in the reactions of the polymeric component must have originated in the second fraction i.e. from low molecular weight dimers and trimers of cadinene. The chromatograms show that as time of reaction increases, the second fraction starts to crack from bicadinanes/tricadinanes to naphthalenes and benzenes. At long reaction times, undesirable recombination reactions are occuring but the second fraction has almost totally been converted to compounds that can be upgraded to cycloalkanes. The polymeric fraction is converted to dimethylnaphthalene and cadinane.

These preliminary findings do give some ideas on how resinite in coal would behave under liquefaction conditions. The sesquiterpenoid polymer that makes up Utah resinite would break apart to produce cadinene, which dehydrogenates and dealkylates to dimethylnaphthalenes, and to a smaller extent substituted decalins. The extent of the depolymerisation reaction is not known at this stage of the investigation, but this problem will be addressed later.

With this foundation to work on, future research will include reactions at lower temperatures, catalytic upgrading of the products and a more detailed investigation into the depolymerisation of polycadinene.

Refereneces

1 van Aarssen, B.G.K., Cox, H.C., Hoogendoorn, P., and de Leeuw, J.W. *Geochem. Cosmochim. Acta.* 54, 3021, **1991.**

2. Anderson, K.B. Winans, R.E., and Botto, R.E. *Org. Geochem.* 18(6), 829, **1992.**

3. Crelling, J.C., Pugmire, R.J., Meuzelaar, H.L.C., McClennen, W.H., Huai, H. and Daras, J. *Energy Fuels.* 5, 688, **1991.**

4. Meuzelaar, H.L.C., Huai, H., Lo, R., and Dworzanski, J.P. *Fuel. Proc. Technol.* 28, 119, **1991.**

5. Cocker, W., Cross, B.E., and McCormick. J. The elimination of non-angular alkyl groups in aromatisation reaction. Part 1. *J. Chem. Soc.* 72-77, **1952.**

3. Shape Selective Isopropylation of Naphthalene Over Zeolite Catalystss. (Contributed by Andrew D. Schmitz and Chunshan Song)

Introduction

This section of the report presents some results which derive largely from collateral work in our laboratories. The results are presented here because we recognize that economic feasibility for coal liquefaction can be enhanced by selective alkylation of 2-ring aromatic products, producing value-added aromatic chemicals. Conversion of even a small fraction of the 2-ring aromatics can significantly increase value of the total product slate, while the majority of the liquefaction product is converted to jet fuel. Thus an opportunity exists for enhancing the net economic feasibility of a coal-to-jet fuel process, via significantly enhanced by-product credits. Isopropylation of 2-ring aromatics is a viable process for producing dialkyl aromatics. Of particular interest are 2,6-dialkylnaphthalenes and 4,4'-dialkylbiphenyls which, when oxidized to the corresponding diacids, can be polymerized to produce high value engineered plastics. While alkylation of aromatics is a facile process, regioselective alkylation requires a shape-selective catalyst.

Mordenite zeolite is a high surface area crystalline material with one-dimensional channels formed from 8-atom rings. With an average channel diameter of 6.7 x 7.0 Å, mordenite affords regioselective alkylation of naphthalene at positions β to the fused-ring carbons, and 1,1'-biphenyl at the 4- and 4'-positions. Regioselectivity is sensitive to catalyst pretreatment and reaction parameters.

Summary

Selective alkylation of naphthalene (NAP) by 2-propene (P) has been studied over native and chemically modified commercial H-mordenites (HM). Experiments were performed in batch mode using a 30 mL tubing bomb reactor. This report summarizes experimental procedures and results for the systematic evaluation of the following reaction parameters.

Temperature: 200, 250 or 300°C;
Time: 3.5 h standard run, or a *short run* where the reaction was stopped when the total pressure ceased to decrease over ca. 15 min. interval (0.5-1.5 h);
NAP/P ratio: typically 0.5 (molar basis), but 1.0 also used;
Solvent: cyclohexane, decahydronaphthalene (decalin), or 1,3,5-trimethylbenzene (mesitylene); solvent volume: 0, 1, 6 or 15 mL.

The reaction products were primarily mono (MIPN), di (DIPN), tri (TRIPN) and tetra (TEIPN) isopropyl-substituted naphthalenes (IPN's). When no solvent was used, nearly all of the side products were alkylated naphthalenes other than *solely* isopropyl-substituted naphthalenes (RNAP's). Other minor products were propylene oligomers, tetralin and alkylated tetralin (RTET), phenanthrene, anthracene and binaphthyl (POLY). Generally, products derived from coupling and cracking of naphthalene were only observed at 300°C. The use of reaction solvents invariably led to other side-reaction products.

Saturated hydrocarbon solvents add to NAP, accounting for 8–20% of the product at 200°C. With cyclohexane, dimethyldecalins are produced, especially at 250 and 300°C, probably by Diels-Alder condensation of partially dehydrogenated cyclohexane and propylene dimer. RTET products were observed in significant amounts with decalin solvent at 200°C, and become significant with cyclohexane solvent at 250°C. Although mesitylnaphthalene products were not observed, isopropyltrimethylnapthalene compounds were produced in significant amount. Also, compared to the neat reaction, use of mesitylene solvent approximately doubles the fraction of RNAP products, apparently as a result of transalkylation/disproportionation reactions. Side reactions were minimized and selectivity for β-substitution was optimized by using only 1 mL reaction solvent. Yet, the highest 2,6/2,7 DIPN isomer ratios were obtained with 6 mL reaction solvent. Carbon numbering convention for naphthalene are described in Figure 32.

Use of a solvent diminishes the catalyst activity: NAP conversion and the extent of polyalkylation both decrease. However, there are benefits of solvent use. Presence of a solvent in the reactor leads to an increase in product recovery according to mass balance calculations. At 200°C reaction temperature, all solvents increase both the percentage of 2,6-isomer in DIPN's and

2,6/2,7 isomer ratio. At 250°C, mesitylene gives the same trend, but cyclohexane does not. Decalin was only tested at 200°C.

A reaction temperature of 200°C was found to be optimum as neither NAP conversion nor the percentage of alkylation at the β-positions of NAP increased at higher temperatures. At or above 250°C, the percentage of isopropylnaphthalenes in the product also decreased, while RNAP's became more prevalent, presumably as a result of thermal cracking, isomerization and transalkylation reactions. Alkylation by solvent (cyclohexane and decalin), and of solvent (mesitylene) also increased markedly at 250°C.

Effects of varying the reaction time were complex. The most significant conclusions are that both β-selectivity and ββ-selectivity increase with time, while optimization of 2,6-DIPN selectivity requires limiting the reaction time.

HM30 demonstrated the highest activity. Small amounts of K_2O or ZnO were deposited on the surface of HM30 to modify its surface acidity. Modified HM30 catalysts showed small decreases in activity and reactions leading to RNAP products, but native HM30 showed superior shape selectivity. HM20 showed the lowest activity of all the catalysts tested. The one experiment done with HM20 indicated that a higher percentage of β-alkylation is obtainable with HM30, but more data are required for proper comparison. Similarly, HM30 and modified HM30 catalysts produce significantly higher 2,6/2,7 DIPN isomer ratios than HM20.

Experimental

Catalyst Preparation. Both H-mordenite samples were supplied from The PQ Corporation, Zeolites and Catalysts Division, Valley Forge, PA: CBV 20A, lot AD29-1, molar $SiO_2/Al_2O_3 = 20$ (HM20); and CBV 30A, lot HM-6, molar $SiO_2/Al_2O_3 = 35$. Catalysts were prepared for use by calcination in an open-air muffle furnace according to conditions summarized in Table 3. During calcination, catalysts were contained in a 30 mL porcelain casserole.

1.35 % ZnO/HM30 Catalyst: 5.00 g fresh HM30 was impregnated with 5.2 mL of a 25 mL solution prepared by dissolving 0.3300 g ZnO (Johnson-Matthey, 99.999% Zn on metal basis) in 6*M* HNO_3, to just saturate the pores. The mixture was allowed to stand for 1 h, then nitric acid was removed using a rotary evaporator equipped with a cold-water aspirator, heating at 0.5 h at 35°C, then 0.5 h at 60°C. Subsequently the catalyst was dried in the muffle furnace at 250–270°C for 4 h, then calcined at 460°C for 10 h. Anhydrous zinc nitrate rapidly decomposes at 350°C. The catalyst was removed while hot, transferred to a stoppered vial, and stored in a desiccator over anh. $MgSO_4$. Zinc oxide content was determined by formulation.

4.80 % ZnO/HM30 Catalyst: This catalyst was prepared in a manner similar to the previous procedure. Thus, 1.0056 g ZnO was dissolved 6*M* HNO_3 to make 25 mL, and 6 mL of

the solution was added to 5.03 g fresh HM30. After removal of the nitric acid, the solid was dried, calcined at 350°C for 2 h, then 500–520°C for 14 h in the muffle furnace.

1.24% K_2O/HM30 Catalyst: 0.6769 g KNO_3 (Fisher, A.C.S. Cert. Rgt.) was dissolved in distilled water to make 25 mL, and 5 mL of the solution was added to 5.00 g fresh HM30. Water was rotary evaporated. In the muffle furnace, the solid was dried, then calcined at 460°C for 10 h, ramped to 550°C over 2 h, and held at 550°C for 0.7 h. The decomposition of anhydrous KNO_3 to K_2O is reported to occur at 530°C.[2]

Catalyst Testing. A 30 mL, stainless steel tubing bomb, batch reactor was used for all experiments. The reactor was charged with 1.0 g catalyst and 0.61–0.63 g (4.8–4.9 mmol) naphthalene (Aldrich, 99%). In some cases, solvent was then added. For the 15 mL solvent experiments, 15 mL of a solution prepared by dissolving NAP in the reaction solvent was added to the reactor. The charged reactor was sealed and leak-tested by pressurizing with N_2 (also functioning as a purge step). After venting N_2, propylene (Matheson, polymer purity, 99.5% min.) was added to achieve the desired naphthalene/propylene ratio (NAP/P). Propylene mass was determined by difference in reactor mass (typically 0.40 ± 0.02 g, 9.5 mmol). Propylene is soluble in hydrocarbon solvents, especially cyclohexane, so total pressure could not be used to monitor the amount of propylene added to the reactor.

The reactor was affixed to a moveable holder so that approximately two-thirds of the length of the reactor assembly was immersed in the fluidized sand-bath heater. Vertical agitation at 3.3 cps was commenced. Temperature was measured with a thermocouple inserted in the center of the bath and maintained to ± 2°C of the set-point by an electronic temperature controller.

At the end of the test, the reaction was quenched by immersing the horizontal member of the reactor in cold water, and the reactor was allowed to stand at room temperature overnight. The remaining gas headspace was vented and the reactor was opened. *n*-Tridecane internal standard was added into the reactor with 5–10 mL extraction solvent (usually acetone, toluene used in some cases). After stirring and allowing to stand for 0.5 h, the contents of the reactor were suction filtered and washed on a 0.45 μm polypropylene disk. Filtrate and washings were combined for GC analysis. The solid was dried and weighed to determine the amount of material remaining adsorbed on the catalyst. The initially colorless catalysts were typically brown or red-brown following reaction. The product solution color varied from nearly colorless to orange and was typically pale yellow.

Product Analysis. GC and GC-MS analyses were performed using a 30 m x 0.25 mm o.d. x 0.25 μm coating thickness DB-17 capillary open-tubular column (J&W Scientific). Oven temperature programming was as follows: initial temperature 40°C, ramped at 4°/min to 280°C, and held at 280°C for 10 min. The FID and split/splitless injector were held at 290°C. Helium

carrier gas flowrate was approximately 1 mL/min. Component identification was made by GC-MS and by comparison with retention times for known components.

$$RWR_{NAP} = \frac{m_{NAP} / A_{NAP}}{m_{IS} / A_{IS}}$$

where: m = *mass* (1)

A = *area*

IS = *internal standard*

Products were quantitated by internal standard. Standard solutions of NAP, 2-MIPN and 2,6-DIPN were prepared with both *n*-nonane and *n*-tridecane internal standards for measurement of FID relative weight response factors (RWR's). Calculation of RWR for NAP is shown in Equation 1. RWR values for other compounds are either from lists tabulated by W.-C. Lai or estimates based on RWR's for similar compounds. A list of RWR values appears in Table 4. The estimated error in RWR for NAP, MIPN's and DIPN's is ± 1%. RWR for components where calibration has not been performed is ca. ± 2%.

$$m_i = A_i \times RWR_i \times \frac{m_{IS}}{A_{IS}} \qquad (2)$$

It follows from Equation 1 that the mass m_i, or moles N_i, of any component in the analysis can be calculated as shown in Equation 2. Naphthalene conversion was calculated as shown in Equation 3. The subscript o denotes the initial amount of NAP charged into the reactor; whereas; subscript f is for moles NAP in the product solution extracted from the catalyst and reactor. Poor laboratory technique may lead to erroneously high conversions; consequently, careful product collection procedures were executed and most of the unrecovered NAP is assumed to be strongly adsorbed on the catalyst surface, either unreacted or as products.

$$\%NAP\ \ conversion = \frac{N_{NAP_o} - N_{NAP_f}}{N_{NAP_o}} \times 100 \qquad (3)$$

The overall selectivity to a given product S is the ratio of moles of that product to total moles of products derived from NAP. This calculation for 2-MIPN is shown in Equation 4. Overall selectivities and product yields Y (see example for 2-MIPN, Equation 5) are used in Table 3 which is a detailed listing of the reaction product distribution for each experiment.

$$\%S_{2-MIPN} = \frac{S_{2-MIPN}}{\sum_{i}^{n} N_{prod_i}} \times 100 \qquad (4)$$

$$\%Y_{2-MIPN} = \frac{Y_{2-MIPN}}{N_{NAP_o}} \times 100 \qquad (5)$$

The terms defined in Equations 6-8 give a measure of shape selectivity, where N_{DIPN_T} is the total moles of all diisopropylnaphthalene isomers. DIPN isomer substitution patterns are summarized in Table 5.

$$\beta\text{-}selectivity = \%2\ in\ MIPN = \frac{N_{2-MIPN}}{N_{2-MIPN} + N_{1-MIPN}} \times 100 \qquad (6)$$

$$\%2,6\ in\ DIPN = \frac{N_{2,6-DIPN}}{N_{DIPN_T}} \times 100 \qquad (7)$$

$$\beta\beta\text{-}selectivity = \%2,6+2,7\ in\ DIPN = \frac{N_{2,6-DIPN} + N_{2,7-DIPN}}{N_{DIPN_T}} \times 100 \qquad (8)$$

Results and Discussion

A detailed listing of experimental parameters and product distribution for each catalyst test are provided in Table 3. *Study* denotes identification numbers assigned to each experiment.

Catalyst Comparisons. Results for propylene addition to NAP at 200°C for each of the five catalysts used in this work are reported in Table 6. The symbol %TRIPN+ denotes the sum of IPN products where the degree of substitution is three or higher. Each of the runs was terminated when the total pressure ceased to decrease over ca. 15 min. Data are presented for HM30 calcined at 450-470°C for either 5.5 or 17 h. Regardless of calcination conditions, HM30 affords higher conversions and more polyalkylated IPN products than the other catalysts. Given that the relative error in the 2,6/2,7 ratio is approximately 2%, it is clear that catalysts based on HM30 offer the highest 2,6-DIPN yields. Selectivity for 2,6-DIPN is optimum early in the runs (see below), so these results are not expected to improve with time.

Metal oxides were deposited on the surface of HM30 as selective poisons in attempt to reduce side reactions (eg., isomerization, cracking and disproportionation and transalkylation). These catalysts offered a modest increase in the total IPN selectivity at 200°C. A more appreciable gain would be anticipated at higher temperatures. For example, at 250°C, total IPN selectivity for HM30 in a neat reaction drops to *ca.* 82%, whereas RNAP's increase from about 5% to 12%. Modified HM30 catalysts have not yet been tested at temperatures other than 200°C. The dramatic

decrease in β-substitution selectivity and concurrent drop in activity for modified HM30 catalysts indicates that the deposited metal oxides obstruct channel openings. Fewer accessible acid sites (lower turnover frequency) and a higher percentage of reaction taking place on non-selective external surface sites (lower β-substitution selectivity).

Fellmann et al. have established a basis for evaluating shape selectivity in isopropylation of NAP. A non-shape selective, amorphous SiO_2-Al_2O_3 (Grace) catalyst was used to achieve thermodynamic equilibrium of the products from reaction between NAP and propylene at 275°C. Propylene was delivered at a constant rate of 25 cm^3/min to a 300 cm^3 stirred autoclave reactor containing 90 g NAP and 10 g catalyst. Their results are summarized in Table 3.

As will be seen below, over HM30, both %2,6 in DIPN and 2,6/2,7 ratio drop significantly when temperature is increased. It is logical to expect that this shift is governed by equilibrium. Considering the data in Table 6, only HM30 (calcined 5.5 h) gives a diisopropyl product distribution significantly different than the 275°C equilibrium described by Fellmann. Shape selectivity is borderline for the other catalysts.

It is clear that calcination conditions dramatically effect the performance of HM30. Two additional comparison runs (Table 8) reinforce this conclusion. Calcination for 5.5 h at 450-470°C is sufficient to achieve high NAP conversion and optimum β-substitution selectivity. Long-term calcinaiton results in a dramatic decrease in %2,6-DIPN and 2,6/2,7 ratio, and a comparatively high concentration of TRIPN+. The shift in product distribution indicates strong participation by hyperactivated external surface sites that catalyze non-selective alkylation. A large amount of catalyst was used, making available a large external surface area.

Effect of Run Time. Regardless of catalyst composition, use or choice of reaction solvent, the 2,6/2,7 DIPN isomer ratio decreases with run time (Table 9). HM30 calcined 17 h has the highest isomerization activity, showing a 27% decrease in 2,6/2,7 over time. High (perhaps equilibrium) conversion is reached very quickly with native HM30, but conversion drops over time which suggest that the products undergo disproportionation and transalkylation. Reaction solvents cause decreases in both conversion and extent of polyalkylation. Conversion increases with time for catalysts deactivated by ZnO or solvent. Only when mesitylene is used do %2,6 and the 2,6/2,7 ratio in DIPN products remain essentially unchanged over time. Total IPN yield and selectivity are low when cyclohexane solvent is used due to the competing addition of solvent to NAP.

Fellman et al. have observed similar changes in DIPN product distribution with time. Table 10 lists their results for 90 g NAP and 1.0 g mordenite (SiO_2/Al_2O_3 = 25) catalyst in a 300 cm^3 stirred autoclave, constant 110 psig propylene, at 275°C. Both %2,6 in DIPN and 2,6/2,7 are significantly larger than what has been observed in the present work, and both decrease throughout the run. The catalyst was prepared by dealuminating synthetic mordenite by a

combined steaming (steam in helium at 400°C), acid leaching (4 h in refluxing 0.5 M HCl), and calcining procedure (500°C for 16 h in air). Whereas comparable activity and shape selectivity can be achieved by acid leaching and calcination alone, Fellman et al. argue steaming is necessary to produce a more robust catalystt.

Influence of Reaction Solvents on Product Distribution. Use of reaction solvents is examined more closely in Table 11. Again, it is seen that reaction solvents poison catalyst activity: both conversion and extent of polyalkylation decrease. With the exception of the 1 mL of mesitylene run, total IPN yields and selectivities are considerably higher without solvent.

Use of a solvent in 200°C runs increases %2,6 in DIPN and 2,6/2,7 ratio (2,6/2,7 ratio relative error ca. ± 2%). At 250°C, mesitylene may offer modest improvement in 2,6-DIPN selectivity, but cyclohexane does not (2,6/2,7 remains high, but %2,6 in DIPN is very low). Decalin solvent was not used in 250°C runs. Generally, β-selectivity in the MIPN products is comparable for runs with or without solvent, excepting the cases where the solvent is highly involved in side reactions. Understanding the mechanism by which the solvent influences the product distribution could enhance new catalyst development.

Solvents may influence several aspects of the catalysis. Since all of the solvent molecules examined are of sufficiently small dimension to enter the channel structure of mordenite, diffusion of NAP and products through the channels of the catalyst will be impeded. Products with substituents at the α-positions of NAP should be effected more than smaller diameter β-substituted products, leading to a higher percentage of β-substitution in the products.

Surface adsorption of solvent or coke deposits thereby derived will alter acid site strength, distribution and matrix effects on the catalyst surface. Mesitylene can also function as a Lewis base, resulting in adduct formation with acid sites. Enhanced shape selectivity could be the result of strong acid site poisoning. This is particularly important for the non-shape selective external surface of the catalyst.

A second mechanism for enhanced shape selectivity is a decrease in the mean channel dimension of the catalyst upon solvent adsorption and coke formation. Coke formation has been shown to enhance shape selectivity in the reactions of methylbenzenes on ZSM-5. The FCC literature indicates that cycloparaffins are particularly susceptible to coke forming reactions on zeolite acid catalysts.

Effects of changing solvent volume give evidence to support the importance of solvent adsorption and/or coke formation. Consider adduct formation between surface acid sites and mesitylene. At 200°C, 1 mL of mesitylene does not neutralize enough of the non-selective strong acid sites. Only a modest gain in 2,6-DIPN selectivity over the run without solvent is realized. When 6 mL mesitylene is used in the 3.5 h run, %2,6 in DIPN increases 21% and 2,6/2,7 ratio increases 26% over the run without solvent. At 250°C, the adduct is apparently destabilized and

15 mL of mesitylene is required to shift the equilibrium and cause significant gain in 2,6-DIPN selectivity.

Solvent Side-Reactions Over HM30. Concentrations of the most significant side products, for the same data set as in Table 11, are shown in Table 12. Saturated hydrocarbon solvents (cyclohexane and decalin) add to NAP to a significant extent. Tetralin and substituted tetralins (RTET) are also observed. It may be possible to discern whether RTET compounds originate from NAP or from reaction solvent using ^{13}C-labeling experiments. RTET products constitute less than 2% of the products when no solvent is used. Dimethyldecalin products are also produced from cyclohexane. These products arise solely from solvent and propylene, as explained below, and are not counted in overall product selectivity calculations.

At 200°C, the portion of converted NAP that reacts to form cyclohexylnaphthalene is approximately 20%, and at 250°C, as much as 40%. Cyclohexane solvent at 200°C does not add to the baseline RTET yield, but at 250°C RTET constitutes 10–20% of the products. Clearly, cyclcohexane is not a good reaction solvent.

The run with 6 mL decalin at 200°C shows an RTET yield of 5.2%, 10% of the total product yield. With only 1 mL decalin, RTET yield is less than unity. Both runs give approximately 5% decahydronaphthalenylnaphthalene yield, or *ca.* 9% of the product. Decalin, as with cyclohexane, contributes heavily to the byproduct yield and is not a good solvent for use with strongly acidic mordenites.

Mesitylene contributes to RNAP products: RNAP yield and selectivity are approximately doubled compared to runs without solvent. Mesitylene does not add to NAP, but mesitylene is activated by adsorption on the catalyst surface and does undergo isopropylation. Isopropyltrimethylnaphthalene products arise solely from solvent and propylene and are not counted in overall product selectivity calculations.

A reaction scheme that outlines possible routes to the observed products from cyclohexane is shown as Scheme V. A similar scheme could be used to describe reactions of decalin. Concerted pathways are emphasized (*eg.*, Diels-Alder reaction), but radical pathways can not be excluded. The initiation step in reaction of the solvent is dehydrogenation. Possible hydrogen acceptors are propylene or propylene oligomers, NAP or partially hydrogenated NAP, and the catalyst or carbonaceous deposits on the surface of the catalyst. The dimethyldecalin products are probably also involved in RTET formation, since both C_2- and C_3-substituted tetralins are observed.

Effect of Reaction Temperature. The effect of reaction temperature is examined in Table 13, which is an excerpt of data listed in the tables above. It is seen that there is no advantage in operating above 200°C with HM30. While conversion may increase, the total IPN

yield decreases at 250°C due to increased side reactions. Also, a more favorable product distribution is obtained at 200°C.

Effect of NAP/P Ratio. Results for NAP/P ratio 0.5 and 1.0 are compared in Table 14. The MIPN and DIPN isomer distributions remain roughly unchanged, but NAP conversion, total IPN yield and total IPN selectivity all decrease as a result of increasing the NAP/P ratio. Naphthalene-rich charge results in increased selectivity for RTET and RNAP compounds, and the production of 1,1'-binaphthyl.

Optimization of 2,6-DIPN Yield. At 25°C, the equilibrium isomer distribution for MIPN's is 98.5% β and 1.5% α (molar); 2-MIPN is the thermodynamic product. Over zeolite catalysts, β-MIPN concentration is dependent on the nature of the catalyst, catalyst charge, temperature, time and water content [4]. Typically, β-MIPN does not exceed 90% unless the catalyst and reaction conditions are optimized. Fellmann et al. showed that %2,6 in DIPN is only 39%, and 2,6/2,7 = 1 at equilibrium (see Table 7). It is apparent from the work of Fellmann et al. (see Table 10) and the present work (*cf.* Table 9) that increasing the 2,6-DIPN yield, relative to the 2,7 isomer, requires kinetic control of the second addition of propylene. The 2,6 isomer is more rapidly obtained from 2-MIPN than is the 2,7 isomer. In summary, selective production of 2-MIPN requires thermodynamic control: high temperature, high NAP/P ratio and long contact times. Selective 2,6-DIPN production requires first optimizing 2-MIPN yield, then kinetic control in the second alkylation: low temperature, low NAP/P ratio, and short contact times.

At first glance, direct preparation of 2,6-DIPN in a single reactor may seem impractical. However, partially dealuminated, external-surface deactivated mordenites can selectively produce 2-MIPN and will not promote $\beta \rightarrow \alpha$ isomerization. The 1-MIPN isomer is sufficiently large that it can not be produced within the mordenite channels. If the reaction temperature is low, the initial 2,6-DIPN selectivity should be very high; however, 2,6 $\leftarrow \rightarrow$ 2,7 DIPN isomerization is fast, and a mixture of isomers enriched in the 2,6 will nonetheless result.

Elevation of the reaction temperature is often required for adequate NAP conversion levels over mordenites deactivated by dealumination. An alternative approach to extensive dealumination is a combination of mild dealumination followed by deactivation of external surface sites, either by acid site blockage or acid site removal [4]. Selective modification of external surface acid sites can be accomplished with reagents that are incapable of internal surface diffusion, or by protecting intracrystalline pores. An example of the latter involves filling the pores with a hydrocarbon; whereafter, the protected catalyst is treated with an aqueous solution of a reagent suitable for removal or blockage of acid sites, but not soluble in the hydrocarbon [4].

Conclusions

This report summarizes some collateral efforts toward enhancing coal liquefaction economic feasibility through naphthalene isopropylation to product value-added chemicals, as well as some information obtained from the literature. Several parameters concerning the alkylation process have been investigated, and our conclusions are summarized below.

Preferential substitution at the β-positions of NAP is accomplished in the channels of mordenite. Optimizing 2,6-DIPN in the ββ-DIPN product requires kinetic control of the second propylene substitution. External surface acid sites are responsible for isomerization reactions, non-selective substitution and polysubstitution of NAP (TRIPN and TEIPN). Dealumination of mordenite with reagents such as mineral acids that are capable of internal surface diffusion has been shown by other workers to be an effective means for enhancing shape selectivity. However, this procedure results in a gross depletion of acid sites and a decline in activity. Additionally, complete inactivation of external surface sites may yet require further processing.

Deactivation or inactivation of external surface sites may be accomplished by selective blockage or removal. It is suggested here and elsewhere [4] that this procedure alone, or used in conjunction with mild dealumination, may lead to a superior catalyst.

Cycloparaffin reaction solvents are not suitable for use with strongly acidic mordenites at 200 °C or above due to side-reactions of the solvents. Their use may be possible at lower temperatures or with less acidic catalysts. At 200°C, all solvents enhanced selectivity for 2,6-DIPN. It has been suggested that the mechanism involves solvent adsorption and/or coke formation. Mesitylene affords the greatest increase in 2,6-DIPN and contributes only mildly to the byproducts.

Reference

1. Song, C., and Schobert, H.H., *Fuel. Proc. Technol.*, **1993**, 34, 157.
2. Addison, C.C., and Logan, N., *Adv. Inorg. Chem. Radiochem.*, **1964**, 6, 71.
3. Lai, W.-C, personal communication, Material Science and Engineering Dept., Fuel Science Program, Penn State University, University Park, PA 1993.
4. Fellmann, J.D., Saxton, R.J., Weatrock, P.R., Derouane, E.G., and Massioni, P., U.S. Patent No. 5,026,942, June 25, 1991.
5. Keading, W.W., Chu, D., Young, L.B., Weinstein, B., and Butter, S.A., *J. Catal.*, **1981**, 67, 159.
6. Kulkarni, S.J., Kulkarni, S.B., Ratnasamy, P., Hattori, H., and Tanabe, K. *Appl. Catal..*,**1981**, 8, 43.
7. Olah, G.A.and Olah, J.A., *J. Am. Chem. Soc.* **1976**, 98, 1839.

8. Handrick, K., Killing, G, and Kiedel, P., U.S. Patent No. 4,440,957, April 3. 1984.
9. Moreau, P., Finiels, A., Geneste, P., and Solofo, J., *J. Catal.* , **1992**, 136, 487.

APPENDIX I

TABLES

Table 1. Relative areas of the reactants and products of the thermal stressing of ^{13}C-labeled bibenzyl and benzyl alcohol in the presence of additive free JetA-1 fuel.

Time in hours	Relative area* of benzyl alcohol	Relative area* of bibenzyl	Relative area* of toluene
0.000	1.208	10.472	0.328
0.166	0.762	8.339	0.438
1.000	0.425	8.214	0.973
3.000	0.146	7.090	1.760
6.000	0.000	4.551	4.108
12.000	0.000	2.632	6.055
24.000	0.000	1.318	8.595

* area normalized to the area of a signal at 14 ppm.

Table 2. Major peak assignments of TICs of dammar resin hydrogenated at 450°C for various time

Peak Number	Retention time/min	Peak assignment
1	8.3	C2 Benzene
2	14.3	C3 Benzene
3	15.2	C4 Benzene (p-cymene)
4	18.3	C4 Benzene
5	23.6	C2 Indene
6	28.3	C3 Dihydroindene
7	33.6	C2 Naphthalene
8	38.0	C3 Naphthalene
9	40.7	Cadalene
10	44.2	C2 Biphenyl
11	49.7	C2 Anthracene
—	>60	Dimers + trimers e.g bicadinanes etc.

Table 3. Test Conditions and Results for Addition of Propylene to Naphthlene Over H-Mordenite Catalysts Using Various Solvents

				NAP	solvent	% NAP	PRODUCT DISTRIBUTION																											
							total MPNAP		total DIPN		2-MIPN		1-MIPN		%iB	total DIPN		2,7-DIPN		2,6-DIPN		%iBB	2,6/2,7	total TRIPN+		total TRIPN		total TETPN		total subt-NAP		total BINAP		total RIET		total POLY		total CRACK	
study	cat[1]	T/C	time/h	prep	ml/mL	core	Y	S	Y	S	Y	S	Y	S	act	Y	S	Y	S	Y	S	act	ratio	Y	S	Y	S	Y	S	Y	S	Y	S	Y	S	Y	S
HM30 - cyclohexane solvent																																					
m30cy20c	d	200	1.5	0.50	6.0	59.52	36.49	79.42	29.24	63.65	25.96	56.51	3.28	7.15	88.6	7.68	15.41	1.86	4.04	5.74	9.14	79.0	2.02	0.16	0.36	0.16	0.36	0.00	0.00	8.30	18.07	1.15	2.51	0.00	0.00	0.00	0.00	0.00	0.00
m30cy20d	d	200	3.5	0.50	6.0	62.06	36.24	74.83	29.20	61.90	27.23	57.71	1.98	4.19	93.2	6.90	14.64	2.09	4.43	3.48	7.37	88.6	1.66	0.14	0.29	0.14	0.29	0.00	0.00	9.99	21.17	0.91	1.93	0.03	0.07	0.00	0.00	0.00	0.00
m30cy25b[2]	a	250	3.5	0.049	~15	60.14	16.86	49.27	14.25	41.64	8.53	24.92	5.72	16.72	59.8	2.61	7.63	0.31	1.48	0.74	2.15	47.0	1.46	0.00	0.00	0.00	0.00	0.00	0.00	14.87	43.47	1.06	3.11	1.42	4.16	0.00	0.00	0.00	0.00
m30cy25c	b	250	3.5	0.57	~15	62.31	21.06	61.64	17.77	50.10	9.24	26.05	8.53	24.05	52.0	3.98	11.22	0.66	1.86	0.99	2.80	41.6	1.50	0.12	0.33	0.12	0.33	0.00	0.00	9.13	25.70	0.82	2.31	3.67	10.35	0.00	0.00	0.00	0.00
m30cy25d	c	250	3.7	0.40	~15	54.09	13.76	47.63	12.01	41.57	6.50	22.50	5.51	19.07	54.1	1.75	6.06	0.31	1.08	0.48	1.66	45.1	1.53	0.00	0.00	0.00	0.00	0.00	0.00	10.49	36.31	1.63	5.64	3.01	10.42	0.00	0.00	0.00	0.00
m30cy25e	c	250	3.6	0.51	6.0	55.43	9.16	37.30	8.20	33.49	5.28	21.54	2.93	11.95	64.3	0.95	3.88	0.20	0.80	0.30	1.21	31.7	1.51	0.00	0.00	0.00	0.00	0.00	0.00	9.14	37.32	10.86	7.41	4.36	17.80	0.00	0.00	0.00	0.00
HM30 - decalin solvent																																					
m30de20a	c	200	1.5	0.50	6.0	54.06	38.70	73.96	30.16	59.18	22.78	44.54	7.46	14.64	75.3	8.30	16.28	2.17	4.26	4.25	8.33	77.3	1.96	0.25	0.49	0.25	0.49	0.00	0.00	4.86	9.53	2.19	4.29	5.21	10.22	0.00	0.00	0.00	0.00
m30de20b	d	200	3.5	0.50	1.0	78.09	57.48	88.99	36.64	56.66	34.19	52.88	2.45	3.79	93.3	19.78	30.66	5.94	9.19	9.63	14.89	78.7	1.62	1.06	1.65	1.06	1.63	0.00	0.00	5.15	7.97	1.16	1.80	0.87	1.34	0.00	0.00	0.00	0.00
HM30 - mesitylene solvent																																					
m30me20a	c	200	3.5	0.51	6.0	68.65	47.97	91.30	32.45	61.82	29.33	56.25	2.93	5.57	91.0	15.35	29.25	4.23	8.05	8.75	16.68	84.6	2.07	0.17	0.32	0.17	0.32	0.00	0.00	0.00	0.00	4.52	8.61	0.00	0.00	0.00	0.00	0.00	0.00
m30me20b	c	200	1.5	0.49	6.0	56.34	41.49	91.11	28.96	63.59	23.96	52.60	5.01	11.00	82.7	12.41	27.25	3.25	7.14	6.96	15.28	82.3	2.14	0.12	0.27	0.12	0.27	0.00	0.00	0.00	0.00	4.05	8.89	0.00	0.00	0.00	0.00	0.00	0.00
m30me20c	d	200	3.5	0.49	1.0	82.07	63.21	96.12	35.05	53.06	32.44	49.61	2.61	3.45	93.5	26.27	40.17	9.75	14.92	11.67	17.85	81.6	1.20	1.90	2.90	1.90	2.90	0.00	0.00	0.00	0.00	2.50	3.82	0.94	0.96	0.00	0.00	0.00	0.00
m30me25a	b	250	3.5	0.57	~15	62.03	36.41	80.40	28.45	62.82	26.43	58.37	2.01	4.45	92.9	7.96	17.58	3.27	7.23	3.45	7.61	84.4	1.05	0.00	0.00	0.00	0.00	0.00	0.00	0.00	0.00	8.88	19.60	0.00	0.00	0.00	0.00	0.00	0.00
m30me25b	c	250	3.7	0.43	~15	74.17	32.82	81.66	22.61	37.65	20.92	53.54	1.69	4.31	92.5	9.21	23.50	3.36	8.57	4.34	11.07	83.6	1.29	0.20	0.52	0.20	0.52	0.00	0.00	0.00	0.00	7.19	18.36	0.00	0.00	0.00	0.00	0.00	0.00
m30me25c	c	250	3.6	0.49	6.0	68.35	38.01	79.46	30.63	62.78	28.51	58.57	2.11	4.33	93.1	8.01	16.41	3.38	6.93	3.19	6.52	82.0	0.94	0.17	0.35	0.17	0.35	0.00	0.00	0.00	0.00	10.05	20.58	0.00	0.00	0.00	0.00	0.00	0.00
HM30 - no solvent																																					
m30me20b	c	200	3.6	0.51	none	78.54	60.35	96.45	36.21	59.05	34.04	56.27	2.17	3.58	94.0	22.03	33.11	6.31	10.43	10.33	17.07	83.1	1.64	2.11	3.49	1.36	2.25	0.75	1.24	0.00	0.00	2.00	3.44	0.07	0.11	0.00	0.00	0.00	0.00
m30me20c	c	200	1.2	0.50	none	87.46	66.65	96.48	34.00	49.18	30.03	44.30	3.37	4.88	90.1	36.40	43.97	8.51	12.31	15.74	22.77	79.8	1.85	2.25	3.25	2.25	3.25	0.00	0.00	0.00	0.00	2.47	3.57	0.02	0.03	0.00	0.00	0.00	0.00
m30me20d	d	200	0.7	0.49	none	91.29	67.29	95.11	27.00	39.01	18.43	26.05	9.17	12.96	64.0	32.06	45.34	7.07	11.13	13.06	18.46	65.2	1.66	7.61	10.76	6.62	9.36	0.99	1.40	0.00	0.00	3.04	4.30	0.00	0.00	0.42	0.59	0.00	0.00
m30me20e	d	200	3.5	0.50	none	90.28	64.01	96.03	28.71	43.07	25.02	38.09	2.79	4.18	90.3	28.93	43.41	9.04	13.56	10.93	16.40	69.0	1.21	6.37	9.55	5.64	8.47	0.73	1.09	0.00	0.00	2.66	3.98	0.05	0.08	0.00	0.00	0.00	0.00
m30me20f	d	200	3.7	1.09	none	56.98	25.05	88.53	19.49	68.87	17.55	62.02	1.94	6.85	90.1	4.61	16.29	1.27	4.50	1.45	5.12	59.1	1.14	0.95	3.37	0.88	3.09	0.00	0.28	0.00	0.00	2.17	7.68	0.56	1.98	0.53	1.88	0.00	0.00
m30me20g	d	200	3.7	1.01	none	57.41	27.07	89.39	21.57	69.17	19.41	62.26	2.15	6.91	90.0	5.48	17.57	1.63	5.22	1.95	6.27	65.4	1.26	0.83	2.65	0.73	2.35	0.09	0.30	0.00	0.00	1.93	6.18	0.52	1.68	0.86	2.75	0.00	0.00
m30me25e[3]	a	250	3.5	0.22	none	93.07	54.67	76.74	23.51	33.01	21.63	30.36	1.89	2.65	92.0	25.39	35.63	9.97	13.99	8.86	12.43	74.1	0.89	5.77	8.09	5.77	8.09	0.00	0.00	0.00	0.00	13.57	19.05	0.00	0.00	0.00	4.22	3.00	4.22
m30me25b	b	250	3.5	0.55	none	76.23	35.48	82.67	25.72	59.97	23.07	53.80	2.65	6.17	89.7	9.40	21.87	3.25	7.57	3.62	8.41	73.1	1.11	0.36	0.83	0.36	0.83	0.00	0.00	0.00	0.00	5.67	13.20	1.42	3.32	0.00	0.00	0.35	0.81
m30me25c	c	250	3.7	0.49	none	83.97	46.95	85.82	29.79	54.46	27.29	49.89	2.50	4.56	91.4	16.15	29.48	6.12	11.18	6.20	11.33	76.4	1.01	1.04	1.89	1.04	1.88	0.00	0.00	0.00	0.00	6.53	11.94	0.94	2.72	0.00	0.00	0.28	0.52
HM20 - no solvent																																					
m20me20a	e	200	0.5	0.50	none	68.40	56.14	96.36	36.95	63.41	32.77	56.24	4.18	7.17	88.7	17.07	29.30	4.90	8.41	6.94	11.92	69.4	1.42	2.12	3.65	1.86	3.20	0.26	0.45	0.00	0.00	2.04	3.50	0.00	0.14	0.00	0.00	0.00	0.00
1.24% K2O/HM30 - no solvent																																					
mkme20a	f	200	0.5	0.51	none	78.09	59.67	96.64	32.55	52.72	20.83	33.74	11.72	18.98	64.0	21.70	35.15	4.14	6.71	7.66	12.41	54.4	1.85	5.42	8.77	4.78	7.73	0.64	1.04	0.00	0.00	2.07	3.36	0.00	0.00	0.00	0.00	0.00	0.00
1.33% ZnO/HM30 - no solvent																																					
mzme20c	f	200	0.5	0.50	none	77.74	53.85	93.99	29.71	51.86	19.03	34.61	9.88	17.25	66.7	19.38	33.83	4.40	7.68	7.54	13.16	61.6	1.71	4.75	8.30	4.10	7.16	0.65	1.14	0.00	0.00	3.44	6.01	0.00	0.00	0.00	0.00	0.00	0.00
4.8% ZnO/HM30 - no solvent																																					
mzme20a	f	200	0.8	0.51	none	83.98	59.99	96.63	32.20	51.86	20.19	32.51	12.01	19.35	62.7	24.05	38.73	5.57	8.97	10.62	17.11	67.3	1.91	3.75	6.04	3.38	5.44	0.37	0.60	0.00	0.00	2.09	3.37	0.00	0.00	0.00	0.00	0.00	0.00
mzme20b	f	200	3.7	0.52	none	89.83	66.10	97.17	31.30	46.01	28.07	30.68	10.43	15.33	66.7	29.97	44.05	7.47	10.98	12.84	18.88	67.9	1.72	4.83	7.11	4.33	6.37	0.50	0.74	0.00	0.00	1.93	2.84	0.00	0.00	0.00	0.00	0.00	0.00

[1] 1 g of catalyst calcined (a) 500°C for 15 h, (b) 450-460°C for 4 h, (c) 450-470°C for 5.5 h, (d) 450-470°C for 17 h, (e) 525°C for 4 h, or (f) calcined according to procedure described in text

[2] n-Tridecane added before reaction.

Table 4. RWR and Other Constants for GC Quantitative Product Analysis

compound_name	rwr_nonane	rwr_tridecane	mw	group	rwr estimated
BIPH	1.000	1.047	154.21	CRACK	y
BIPH, C1	1.000	1.047	168.24	CRACK	y
BIPH, C2	1.000	1.047	182.27	CRACK	y
BZ, C1	0.959	1.004	92.14	CRACK	n
BZ, C2	0.920	0.963	106.17	CRACK	n
BZ, C3	0.950	0.994	120.19	CRACK	n
BZ, C4	0.952	0.997	134.22	CRACK	n
BZ, C5	1.000	1.047	148.25	CRACK	y
BZ, C6	1.004	1.051	162.27	CRACK	n
CYHX	0.951	0.996	84.16	SOLV	y
CYHX, Me	1.380	1.444	98.19	SOLV	n
DEC	0.990	1.036	138.25	SOLVIPR	n
DEC, C1	1.000	1.047	152.28	SOLVIPR	y
DEC, C2	1.000	1.047	166.31	SOLVIPR	y
Indan	1.111	1.163	118.18	CRACK	n
Indan, 1-Me	1.000	1.047	132.21	CRACK	y
Indan, 2-Me	1.000	1.047	132.21	CRACK	y
iPrOH	1.980	2.072	60.10	RGT	n
MES, iPr	1.004	1.051	162.28	SOLVIPR	n
NAP	0.911	0.871	128.17	RGT	n
NAP, 1-iPr	0.980	0.935	170.25	MIPN	n
NAP, 1-Me	0.980	0.935	142.20	RNAP	n
NAP, 2,6-diiPr	0.993	0.946	212.33	DIPN	n
NAP, 2,7-diiPr	0.993	0.946	212.33	DIPN	n
NAP, 2-iPr	0.980	0.935	170.25	MIPN	n
NAP, 2-Me	0.980	0.935	142.20	RNAP	n
NAP, C2	0.980	0.935	156.23	RNAP	y
NAP, C3	0.993	0.946	170.25	RNAP	y
NAP, C4	0.993	0.946	184.28	RNAP	y
NAP, C5	0.993	0.946	198.31	RNAP	y
NAP, C6	0.993	0.946	212.33	RNAP	n
NAP, C7	1.000	1.047	226.36	RNAP	y
NAP, C8	1.000	1.047	240.39	RNAP	y
NAP, C9	1.000	1.047	254.42	RNAP	y
NAP, CYHX	0.993	0.946	210.32	SOLVNAP	y
NAP, DECA	0.993	0.946	264.19	SOLVNAP	y
NAP, DECA, iPr	1.000	1.047	306.23	SOLVNAP	y
NAP, diiPr	0.993	0.946	212.33	DIPN	n
NAP, Me-CYHX	1.000	1.047	224.36	SOLVNAP	y
NAP, Me-CYHX, iPr	1.000	1.047	267.43	SOLVNAP	y
NAP, tetiPr	0.993	0.946	296.50	TEIPN	y
NAP, triiPr	0.993	0.946	254.42	TRIPN	y
nonane	1.000	0.959	128.26	IS	n
PHEN	1.139	1.192	178.23	POLY	n
PHEN, C1	1.000	1.047	192.26	POLY	y
PHEN, C2	1.000	1.047	206.29	POLY	y
TET	1.000	1.047	132.21	TET	n
TET, C1	1.000	1.047	146.23	TET	y
TET, C2	1.000	1.047	160.26	TET	y
TET, C3	1.000	1.047	174.29	TET	y

Table 5. Diisopropylnaphthalene (DIPN) Isomers

isopropyl substituent positions[1]	molecular size[2] (nm)	substitution pattern	number of isomers
2,6	0.65 x 1.32	ββ	2
2,7	0.65 x 1.25		
1,3	0.88 x 1.04	αβ	3
1,6	0.71 x 1.18		
1,7	0.88 x 1.10		
1,4	0.73 x 1.07	αα	2
1,5	0.71 x 1.16		

[1] *ortho*-Substitution of naphthalene is improbable due to steric hinderance.

[2] Taken from Katayama, Atsuhiko; Toba, M.; Takeuchi, G.; Mizukami, F.; Niwa, S.-i.; Mitamura, S.; *J. Chem. Soc., Chem. Commun.* **1991**, 39.

Table 6. Performance Comparison for Native HM20 and HM30, and HM30 Catalysts in Short Runs at 200°C

							Product Distribution (molar basis)							
							overall total IPN's		%	%	%	%2-	%2,6-	2,6/2,7
catalyst	study	T (°C)	time (h)	N/P (molar)	solvent	%NAP conv	%Y	%S	MIPN	DIPN	TRIPN+	in MIPN	in DIPN	ratio
HM30[1]	m30ne20d	200	0.7	0.49	none	91.3	67.3	95.1	41.0	47.7	11.3	66.8	40.7	1.66
HM30[2]	m30ne20c	200	1.2	0.50	none	87.5	66.6	96.4	51.0	45.6	3.4	90.1	51.8	1.85
HM20[3]	m20ne20a	200	0.5	0.50	none	68.4	56.1	96.4	65.8	30.4	3.8	88.7	40.7	1.42
1.24%K2O/HM30	mkone20a	200	0.5	0.51	none	78.1	59.7	96.6	54.5	36.4	9.1	64.0	35.3	1.85
1.35% ZnO/HM30	mzne20c	200	0.5	0.50	none	77.7	53.8	94.0	55.2	36.0	8.8	66.7	38.9	1.71
4.80% ZnO/HM30	mzne20a	200	0.8	0.51	none	83.9	60.0	96.6	53.7	40.1	6.3	62.7	44.2	1.91

[1] Calcined 450-470°C, 17 h.

[2] Calcined 450-470°C, 5.5 h.

[3] Calcined 525°C, 4 h.

Table 7. Equilibrium Product Distribution Over SiO_2-Al_2O_3 at 275°C from Ref. 4

	Equilibrium Product Distribution (molar basis)				
%NAP conv	% MIPN	% DIPN	% TRIPN+	% 2,6- in DIPN	2,6/2,7 ratio
23.4	91.9	8.1	0.0	36.8	1.00
94.2	31.1	51.5	17.4	38.5	1.03

Table 8. Effect of Calcination Time on HM30 Performance in Long Run at 200°C

							Product Distribution (molar basis)							
		T	time	N/P		%NAP	overall total IPN's		%	%	%	% 2-	% 2,6-	2,6/2,7
catalyst	study	(°C)	(h)	(molar)	solvent	conv	% Y	% S	MIPN	DIPN	TRIPN+	in MIPN	in DIPN	ratio
HM30[1]	m30ne20b	200	3.6	0.51	none	78.5	60.3	96.5	60.0	36.5	3.5	94.0	46.9	1.64
HM30[2]	m30ne20e	200	3.5	0.50	none	90.3	64.0	96.0	44.8	45.2	10.0	90.3	37.8	1.21

[1] Calcined 450-470°C, 5.5 h.
[2] Calcined 450-470°C, 17 h.

Table 9. Effect of Run Time on Product Distribution for Native HM30, With or Without Solvent, and Modified HM30, at 200°C

									Product Distribution (molar basis)					
		T	time	N/P		%NAP	overall total IPN's		%	%	%	%2-	%2,6-	2,6/2,7
catalyst	study	(°C)	(h)	(molar)	solvent	conv	%Y	%S	MIPN	DIPN	TRIPN+	in MIPN	in DIPN	ratio
HM30[2]	m30ne20c	200	1.2	0.50	none	87.5	66.6	96.4	51.0	45.6	3.4	90.1	51.8	1.85
HM30[2]	m30ne20b	200	3.6	0.51	none	78.5	60.3	96.5	60.0	36.5	3.5	94.0	46.9	1.64
HM30[1]	m30ne20d	200	0.7	0.49	none	91.3	67.3	95.1	41.0	47.7	11.3	66.8	40.7	1.66
HM30[1]	m30ne20e	200	3.5	0.50	none	90.3	64.0	96.0	44.8	45.2	10.0	90.3	37.8	1.21
HM30[2]	m30me20b	200	1.5	0.49	6 mL mesy	56.3	41.5	91.1	69.8	29.9	0.3	82.7	56.1	2.14
HM30[2]	m30me20a	200	3.5	0.51	6 mL mesy	68.7	48.0	91.4	67.6	32.0	0.4	91.0	57.0	2.07
HM30[1]	m30cy20c	200	1.5	0.50	6 mL cyhx	59.5	36.5	79.4	80.1	19.4	0.4	88.8	52.8	2.02
HM30[1]	m30cy20d	200	3.5	0.50	6 mL cyhx	62.1	36.2	76.8	80.6	19.0	0.4	93.2	50.4	1.66
4.80% ZnO/HM30[3]	mznne20a	200	0.8	0.51	none	83.9	60.0	96.6	53.7	40.1	6.3	62.7	44.2	1.91
4.80% ZnO/HM30[3]	mznne20b	200	3.7	0.52	none	89.8	66.1	97.2	47.3	45.3	7.3	66.7	42.9	1.72

[1] Calcined 450-470°C, 17 h.
[2] Calcined 450-470°C, 5.5 h.
[3] See text

Table 10. Changes in Product Distribution Over Time for Mordenite (Si/Al=25) at 275°C, from Ref. 4

		Product Distribution (molar percent)				
time	%NAP				% 2,6-	2,6/2,7
(h)	conv	MIPN	DIPN	TRIPN+	in DIPN	ratio
0.0	-	-	-	-	-	-
0.5	27.1	83.1	16.4	0.0	69.8	3.02
1.5	46.9	73.1	27.0	0.0	66.2	2.84
2.5	55.0	65.7	33.8	0.5	62.6	2.44
3.5	77.6	52.4	46.5	1.1	61.5	2.57
4.5	85.0	44.7	53.7	1.6	60.1	2.52
6.5	92.2	32.4	64.6	2.6	52.9	2.39

Table 11. Isopropylnaphthalene Product Distribution for HM30 With or Without Reaction Solvent at 200 and 250°C

							Product Distribution (molar basis)							
		T	time	N/P		%NAP	overall total IPN's		%	%	%	% 2-	% 2,6-	2,6/2,7
catalyst	study	(°C)	(h)	(molar)	solvent	conv	% Y	% S	MIPN	DIPN	TRIPN+	in MIPN	in DIPN	ratio
200°C, short run, 6 mL solvent vs neat reaction														
HM30[2]	m30ne20c	200	1.2	0.50	none	87.5	66.6	96.4	51.0	45.6	3.4	90.1	51.8	1.85
HM30[2]	m30me20b	200	1.5	0.49	6 mL mesy	56.3	41.5	91.1	69.8	29.9	0.3	82.7	56.1	2.14
HM30[1]	m30cy20c	200	1.5	0.50	6 mL cyhx	59.5	36.5	79.4	80.1	19.4	0.4	88.8	52.8	2.02
HM30[2]	m30de20a	200	1.5	0.50	6 mL deca	54.1	38.7	76.0	77.9	21.4	0.6	75.3	51.2	1.96
200°C, long run, 6 mL solvent vs neat reaction														
HM30[2]	m30ne20b	200	3.6	0.51	none	78.5	60.3	96.5	60.0	36.5	3.5	94.0	46.9	1.64
HM30[2]	m30me20a	200	3.5	0.51	6 mL mesy	68.7	48.0	91.4	67.6	32.0	0.4	91.0	57.0	2.07
HM30[1]	m30cy20d	200	3.5	0.50	6 mL cyhx	62.1	36.2	76.8	80.6	19.0	0.4	93.2	50.4	1.66
200°C, long run, 1 mL solvent vs neat reaction														
HM30[1]	m30ne20e	200	3.5	0.50	none	90.3	64.0	96.0	44.8	45.2	10.0	90.3	37.8	1.21
HM30[1]	m30me20c	200	3.5	0.49	1 mL mesy	82.1	63.2	96.1	55.4	41.6	3.0	93.5	44.4	1.20
HM30[1]	m30de20b	200	3.5	0.50	1 mL deca	78.7	57.5	88.9	63.7	34.4	1.8	93.3	48.7	1.62
250°C, long runs														
HM30[2]	m30ne25c	250	3.7	0.49	none	84.0	46.9	85.8	63.4	34.3	2.2	91.6	38.4	1.01
HM30[2]	m30me25c	250	3.6	0.49	6 mL mesy	68.3	38.8	79.5	78.9	20.6	0.4	93.1	39.7	0.94
HM30[2]	m30cy25e	250	3.6	0.51	6 mL cyhx	55.4	9.2	37.4	89.6	10.4	0.0	51.7	31.0	1.51
HM30[2]	m30me25b	250	3.7	0.43	15 mL mesy	74.2	32.0	81.7	70.6	28.8	0.6	92.5	47.1	1.29
HM30[2]	m30cy25d	250	3.7	0.40	15 mL cyhx	54.7	13.8	47.6	87.3	12.7	0.0	45.1	27.4	1.53

[1] Calcined 450-470°C, 17 h.

[2] Calcined 450-470°C, 5.5 h.

Table 12. Side Reaction Product Concentrations for Data in 7

							Overall Product Distribution (molar percent)							
		T	time	N/P		%NAP	total IPN's		solv-NAP		RNAP		RTET	
catalyst	study	(°C)	(h)	(molar)	solvent	conv	% Y	% S	% Y	% S	% Y	% S	% Y	% S
200°C, short run, 6 mL solvent vs neat reaction														
HM30[2]	m30ne20c	200	1.2	0.50	none	87.5	66.6	96.4	0.0	0.0	2.5	3.6	0.0	0.03
HM30[2]	m30me20b	200	1.5	0.49	6 mL mesy	56.3	41.5	91.1	0.0	0.0	4.0	8.9	0.0	0.00
HM30[1]	m30cy20c	200	1.5	0.50	6 mL cyhx	59.5	36.5	79.4	8.3	18.1	1.2	2.5	0.0	0.00
HM30[2]	m30de20a	200	1.5	0.50	6 mL deca	54.1	38.7	76.0	4.9	9.5	2.2	4.3	5.2	10.22
200°C, long run, 6 mL solvent vs neat reaction														
HM30[2]	m30ne20b	200	3.6	0.51	none	78.5	60.3	96.5	0.0	0.0	2.1	3.4	0.1	0.11
HM30[2]	m30me20a	200	3.5	0.51	6 mL mesy	68.7	48.0	91.4	0.0	0.0	4.5	8.6	0.0	0.00
HM30[1]	m30cy20d	200	3.5	0.50	6 mL cyhx	62.1	36.2	76.8	10.0	21.2	0.9	1.9	0.0	0.07
200°C, long run, 1 mL solvent vs neat reaction														
HM30[1]	m30ne20e	200	3.5	0.50	none	90.3	64.0	96.0	0.0	0.0	2.6	3.9	0.1	0.08
HM30[1]	m30me20c	200	3.5	0.49	1 mL mesy	82.1	63.2	96.1	0.0	0.0	2.5	3.8	0.0	0.1
HM30[1]	m30de20b	200	3.5	0.50	1 mL deca	78.7	57.5	88.9	5.2	8.0	1.2	1.8	0.9	1.34
250°C, long runs														
HM30[2]	m30ne25c	250	3.7	0.49	none	84.0	46.9	85.8	0.0	0.0	6.5	11.9	0.9	1.72
HM30[2]	m30me25c	250	3.6	0.49	6 mL mesy	68.3	38.8	79.5	0.0	0.0	10.0	20.5	0.0	0.00
HM30[2]	m30cy25e	250	3.6	0.51	6 mL cyhx	55.4	9.2	37.4	9.1	37.3	1.8	7.4	4.4	17.89
HM30[2]	m30me25b	250	3.7	0.43	15 mL mesy	74.2	32.0	81.7	0.0	0.0	7.2	18.3	0.0	0.00
HM30[2]	m30cy25d	250	3.7	0.40	15 mL cyhx	54.7	13.8	47.6	14.9	43.5	1.1	3.1	1.4	4.16

[1] Calcined 450-470°C, 17 h.

[2] Calcined 450-470°C, 5.5 h.

Table 13. Comparison of HM30 Performance at 200 and 250°C, Neat or With Mesitylene Solvent

							Product Distribution (molar basis)							
		T	time	N/P		%NAP	overall total IPN's		%	%	%	% 2-	% 2,6-	2,6/2,7
catalyst	study	(°C)	(h)	(molar)	solvent	conv	% Y	% S	MIPN	DIPN	TRIPN+	in MIPN	in DIPN	ratio
HM30[1]	m30ne20b	200	3.6	0.51	none	78.5	60.3	96.5	60.0	36.5	3.5	94.0	46.9	1.64
HM30[1]	m30ne25c	250	3.7	0.49	none	84.0	46.9	85.8	63.4	34.3	2.2	91.6	38.4	1.01
HM30[1]	m30me20a	200	3.5	0.51	6 mL mesy	68.7	48.0	91.4	67.6	32.0	0.4	91.0	57.0	2.07
HM30[1]	m30me25c	250	3.6	0.49	6 mL mesy	68.3	38.8	79.5	78.9	20.6	0.4	93.1	39.7	0.94

[1] Calcined 450-470°C, 5.5 h.

Table 14. Comparison of NAP/P Ratio for Catalysis by HM30 at 200°C

							Product Distribution (molar basis)							
		T	time	N/P		%NAP	overall total IPN's		%	%	%	% 2-	% 2,6-	2,6/2,7
catalyst	study	(°C)	(h)	(molar)	solvent	conv	% Y	% S	MIPN	DIPN	TRIPN+	in MIPN	in DIPN	ratio
HM30[1]	m30ne20e	200	3.5	0.50	none	90.3	64.0	96.0	44.8	45.2	10.0	90.3	37.8	1.21
HM30[1]	m30ne20g	200	3.7	1.01	none	57.4	27.9	89.4	77.4	19.7	3.0	90.0	35.7	1.20

[1] Calcined 450-470°C, 17 h.

APPENDIX II

FIGURES

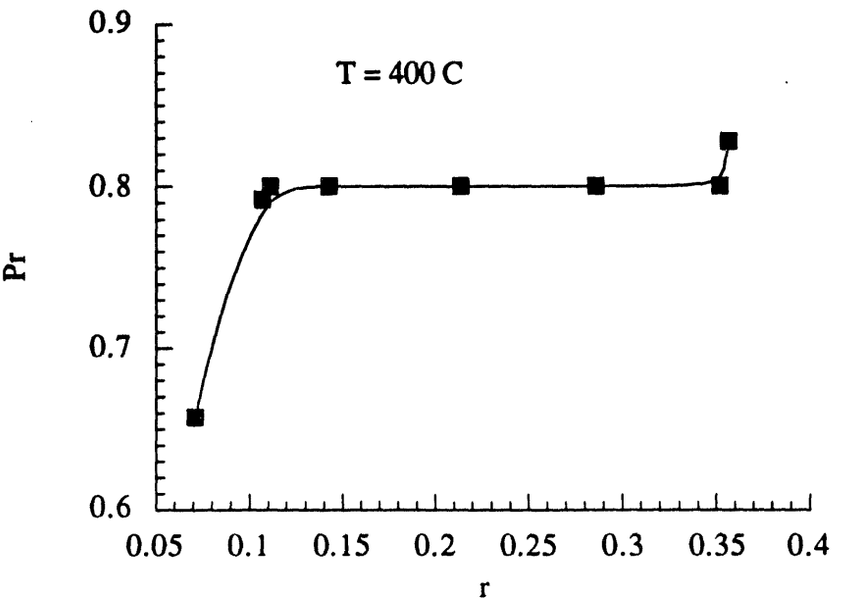

Figure 1. Calculated Reduced Pressure vs Loading Ratio for *n*-Tetradecane at 400 °C.

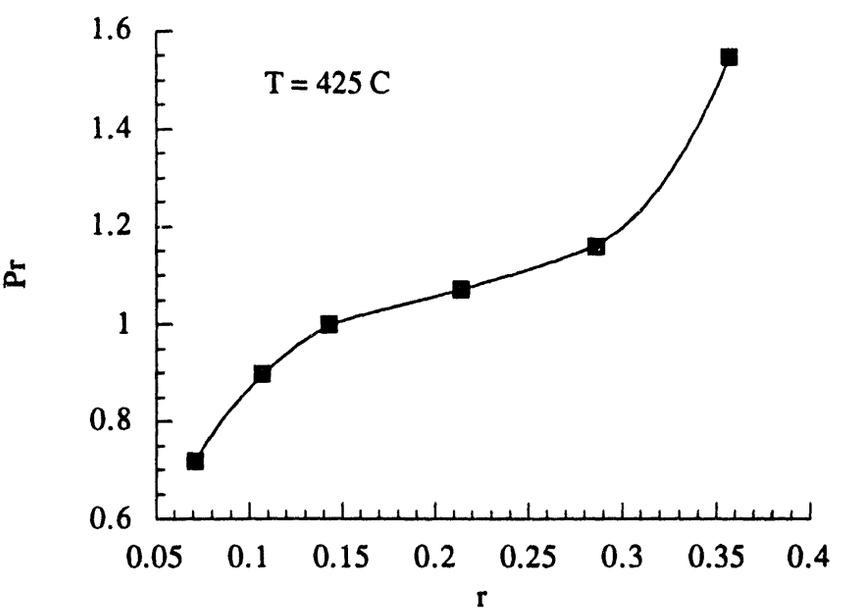

Figure 2. Calculated Reduced Pressure vs Loading Ratio for *n*-Tetradecane at 425 °C.

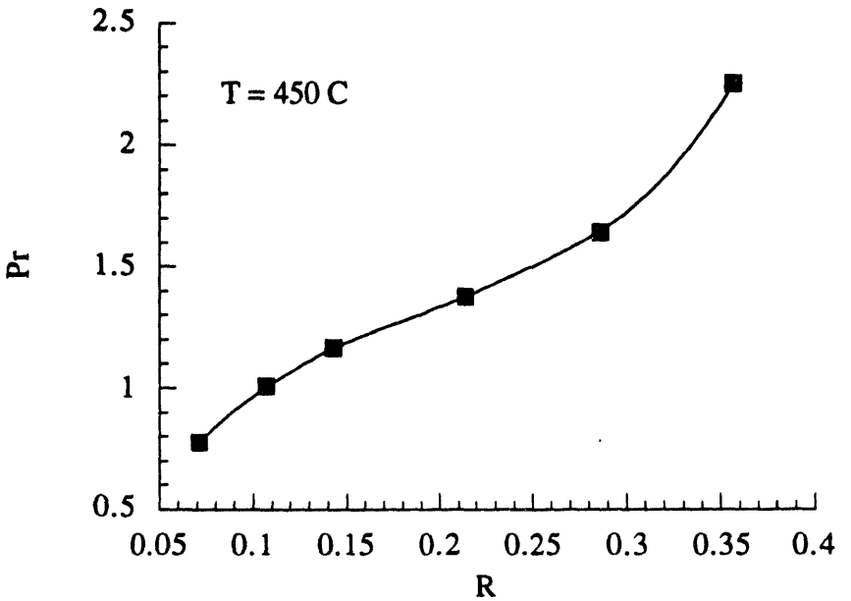

Figure 3. Calculated Reduced Pressure vs Loading Ratio for *n*-Tetradecane at 450 °C.

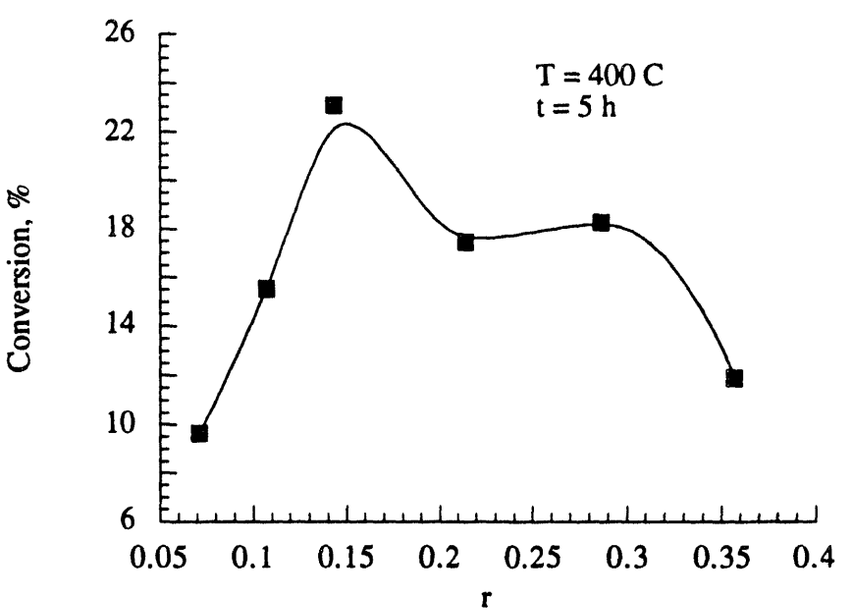

Figure 4. The *n*-Tetradecane Conversion (%) vs Loading Ratio Stressed at 400 °C for 5 h.

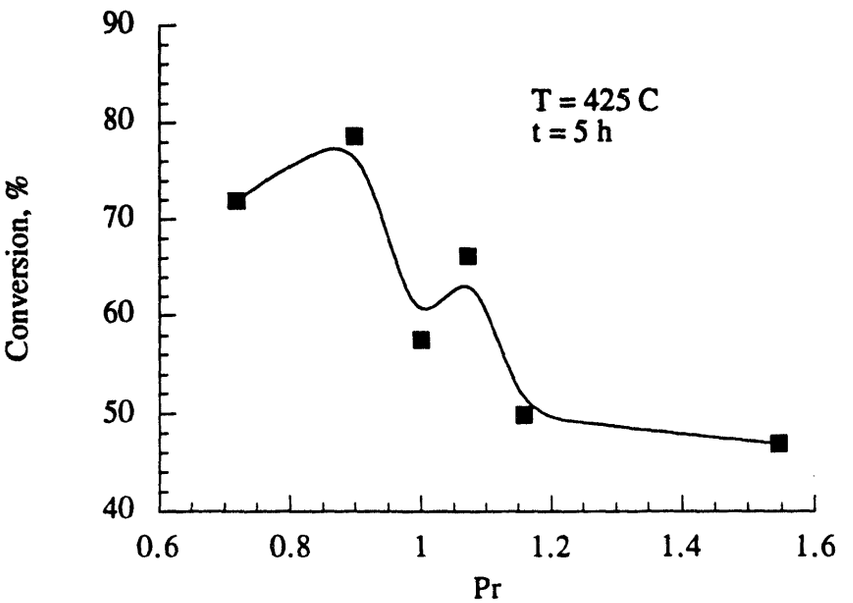

Figure 5. *n*-Tetradecane Conversion (%) vs Reduced Pressure Stressed at 425 °C for 5 h.

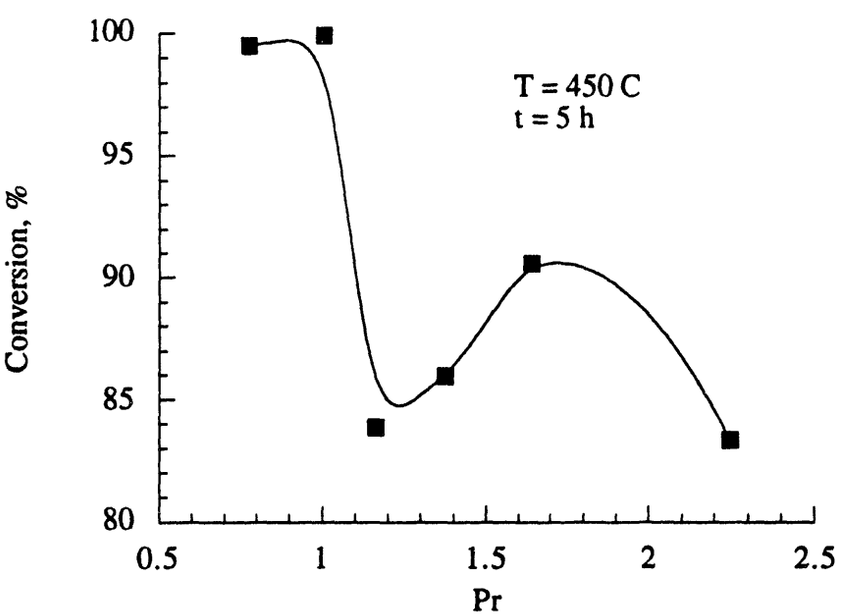

Figure 6. The *n*-Tetradecane Conversion (%) vs Reduced Pressure Stressed at 450 °C for 5 h.

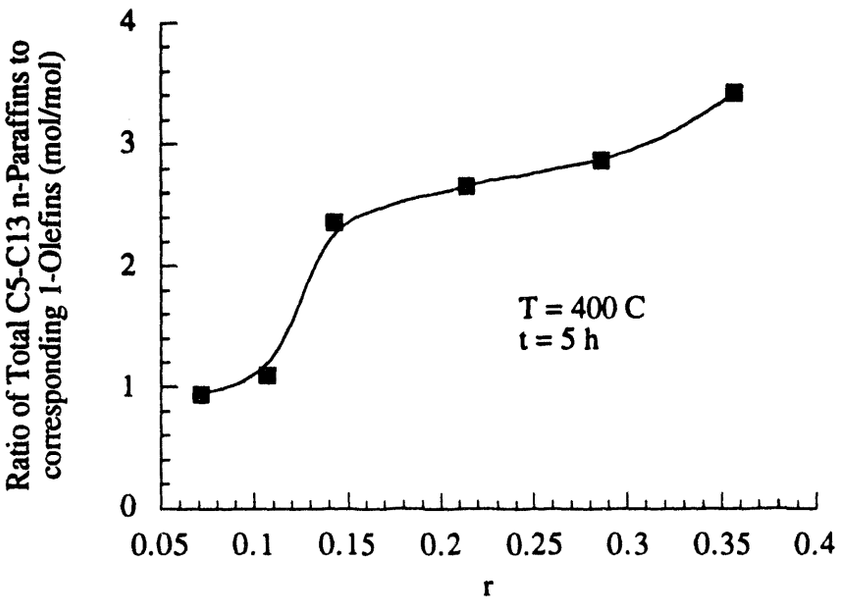

Figure 7. Overall Mole Ratio of C_5-C_{13} *n*-Alkanes to Corresponding1-Alkenes vs Loading Ratio from n-Tetradecane Thermal Decompersition at 400 °C for 5 h.

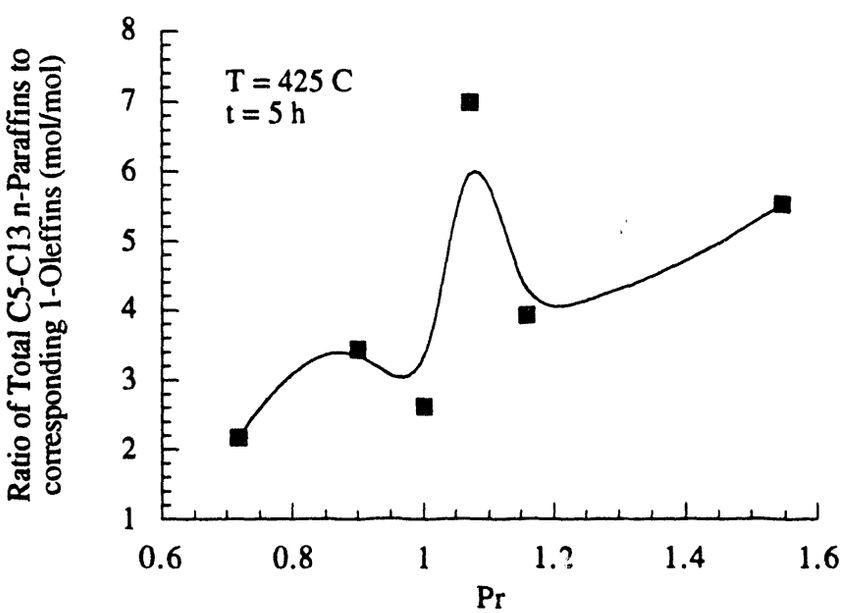

Figure 8. Overall Mole Ratio of C_5-C_{13} *n*-Alkanes to Corresponding1-Alkenes vs Loading Ratio from *n*-Tetradecane Thermal Decompersition at 425 °C for 5 h.

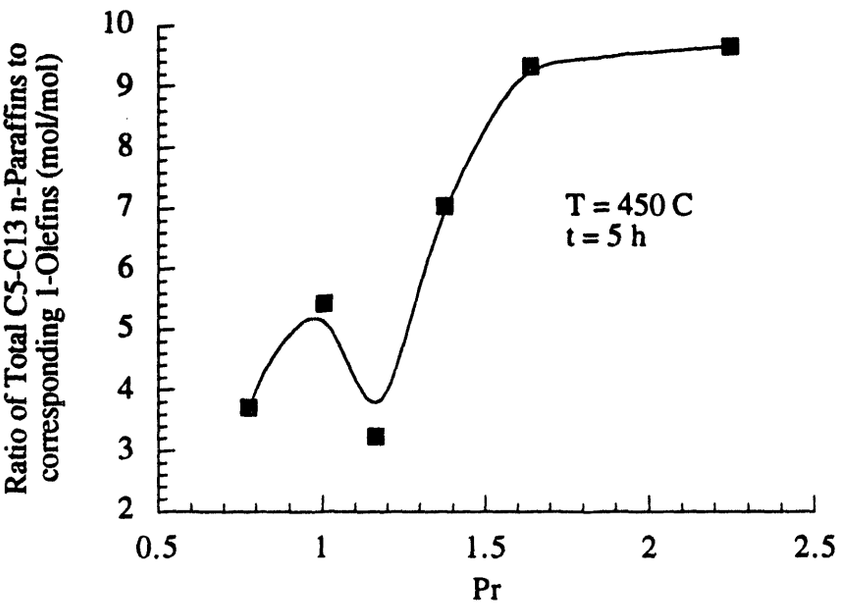

Figure 9. Overall Mole Ratio of C_5-C_{13} *n*-Alkanes to Corresponding1-Alkenes vs Loading Ratio from *n*-Tetradecane Thermal Decompersition at 450 °C for 5 h.

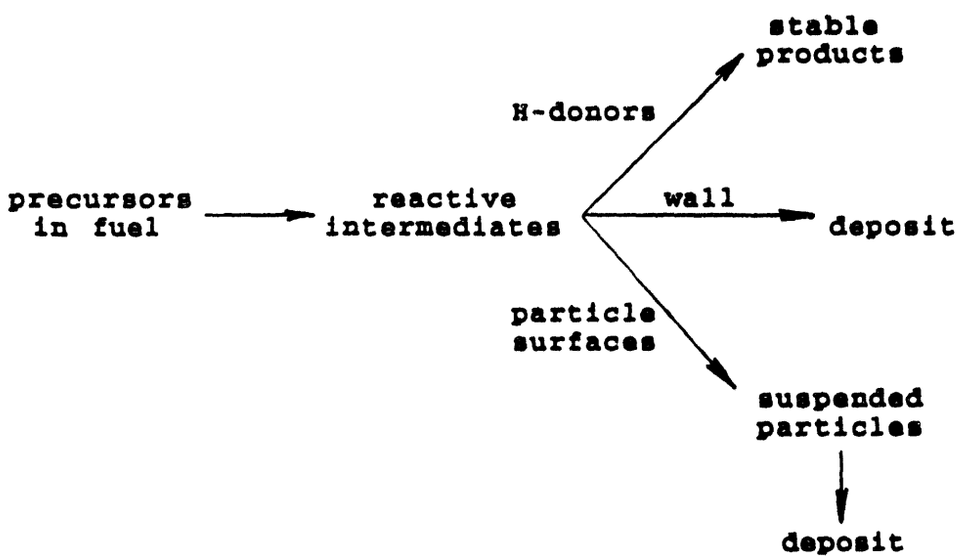

Figure 10. Simple Mechanism for Simultaneous Formation of Suspended Particles, Deposition of the Particles, and Formation of Deposits by Direct Addition of Reactive Species.

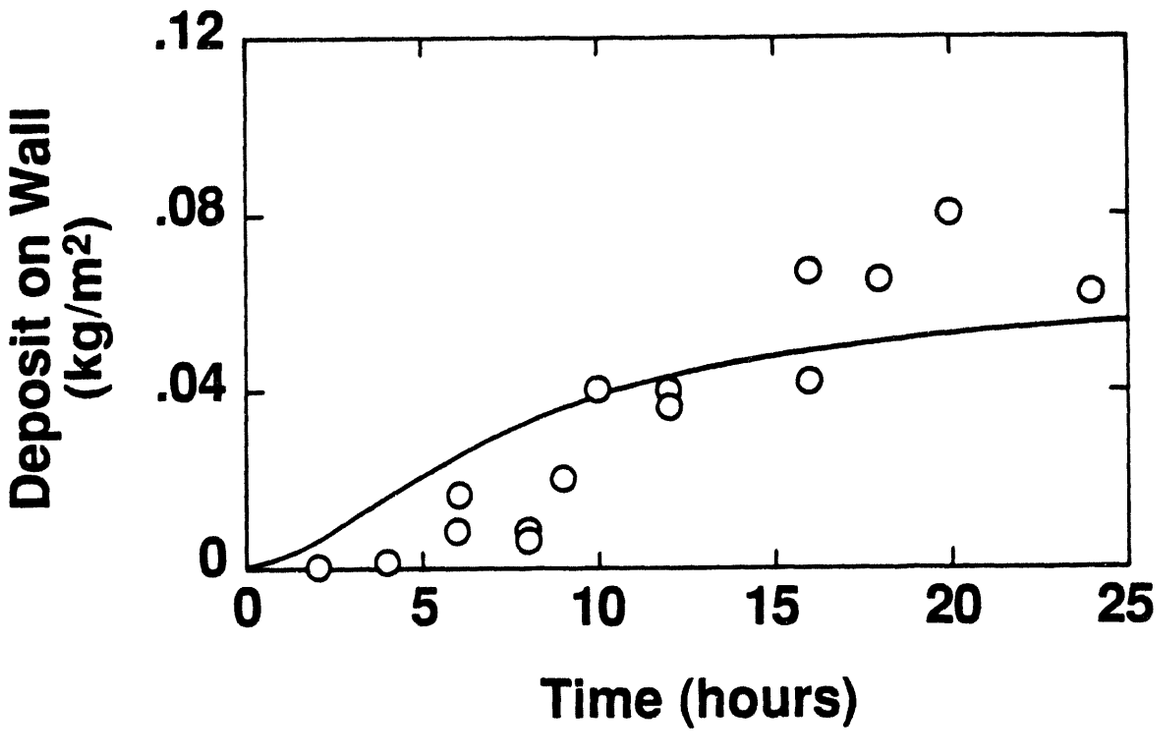

Figure 11. Measured Mass/Area of Deposits Formed on the Vertical Wall of the 20 ml Batch Reactor during Thermal Treatment of Mixtures of 81.5 wt% JP-8C and 18.5 wt% Tetradecane at 450°C under Nitrogen, and Comparison with the Calculated Growth of Deposits by Addition of Reactive Species.

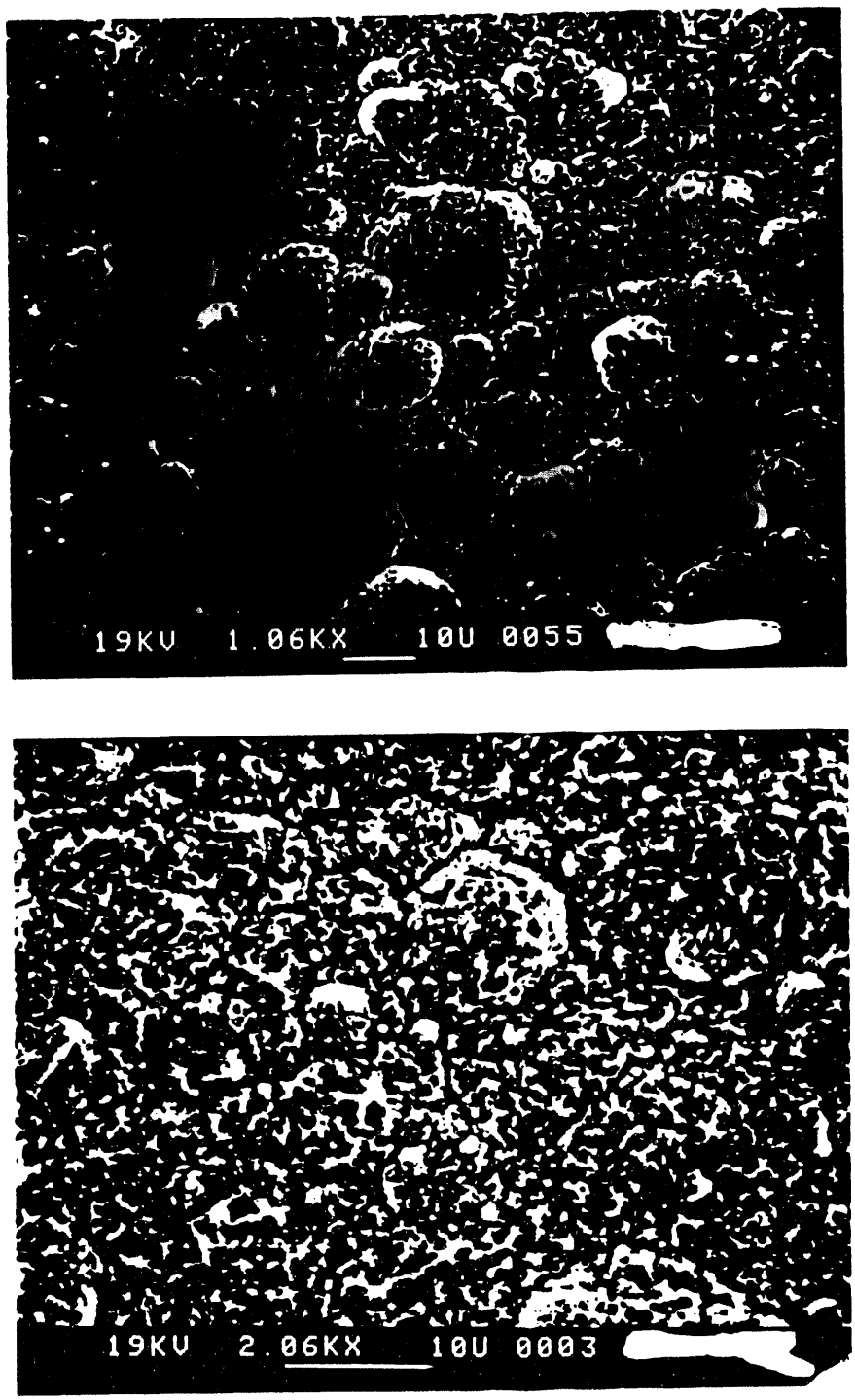

Figure 12. (a) Carbon Deposit on Top Nickel Coupon after 3 Hour Reaction at 450 °C, (b) Carbon Deposit on Bottom Nickel Coupon under the Same Condition.

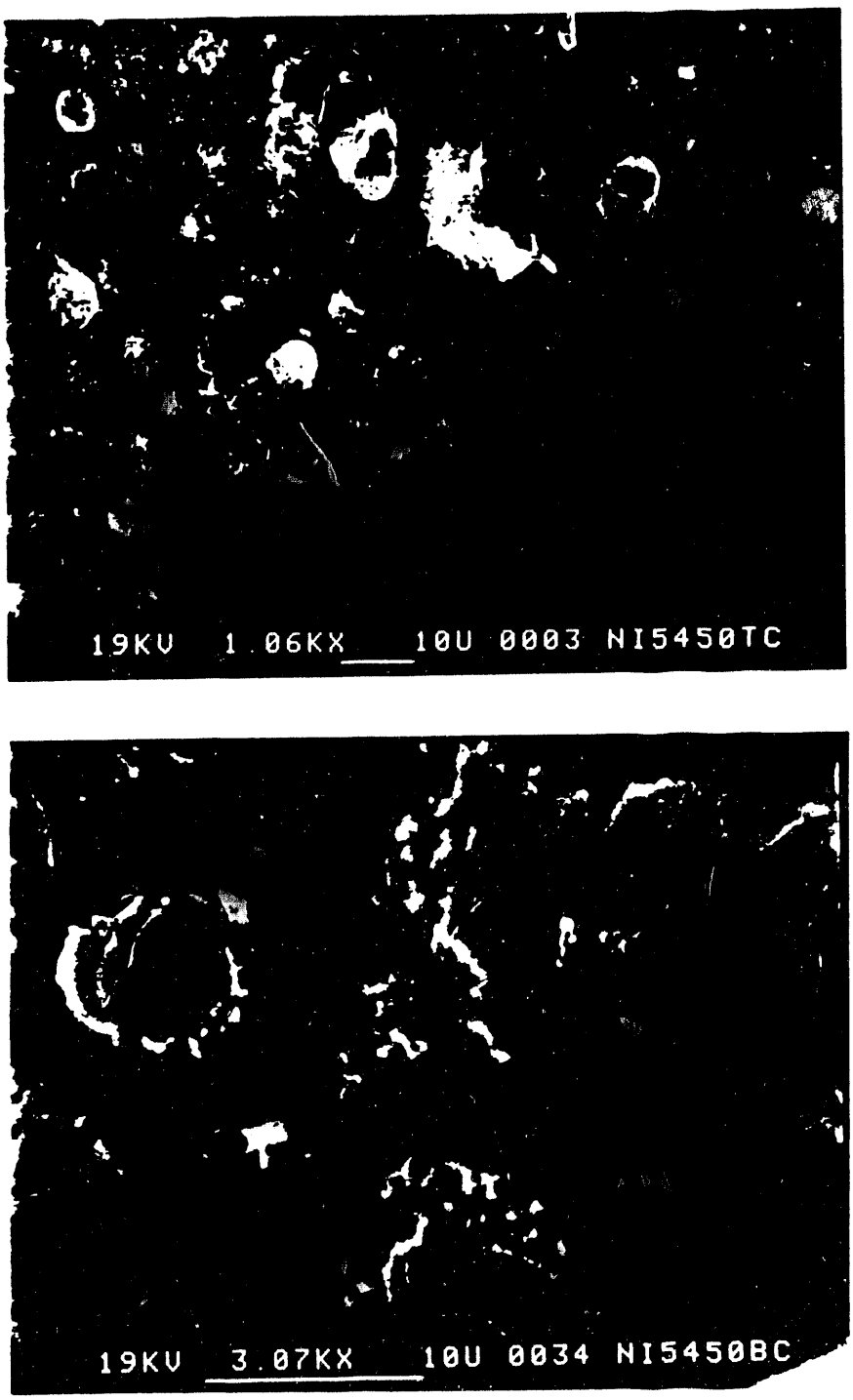

Figure 13. (a) Carbon Deposit on Top Nickel Coupon after 5 Hour Reaction at 450 °C, (b) Carbon Deposit on Bottom Nickel Coupon under the Same Condition.

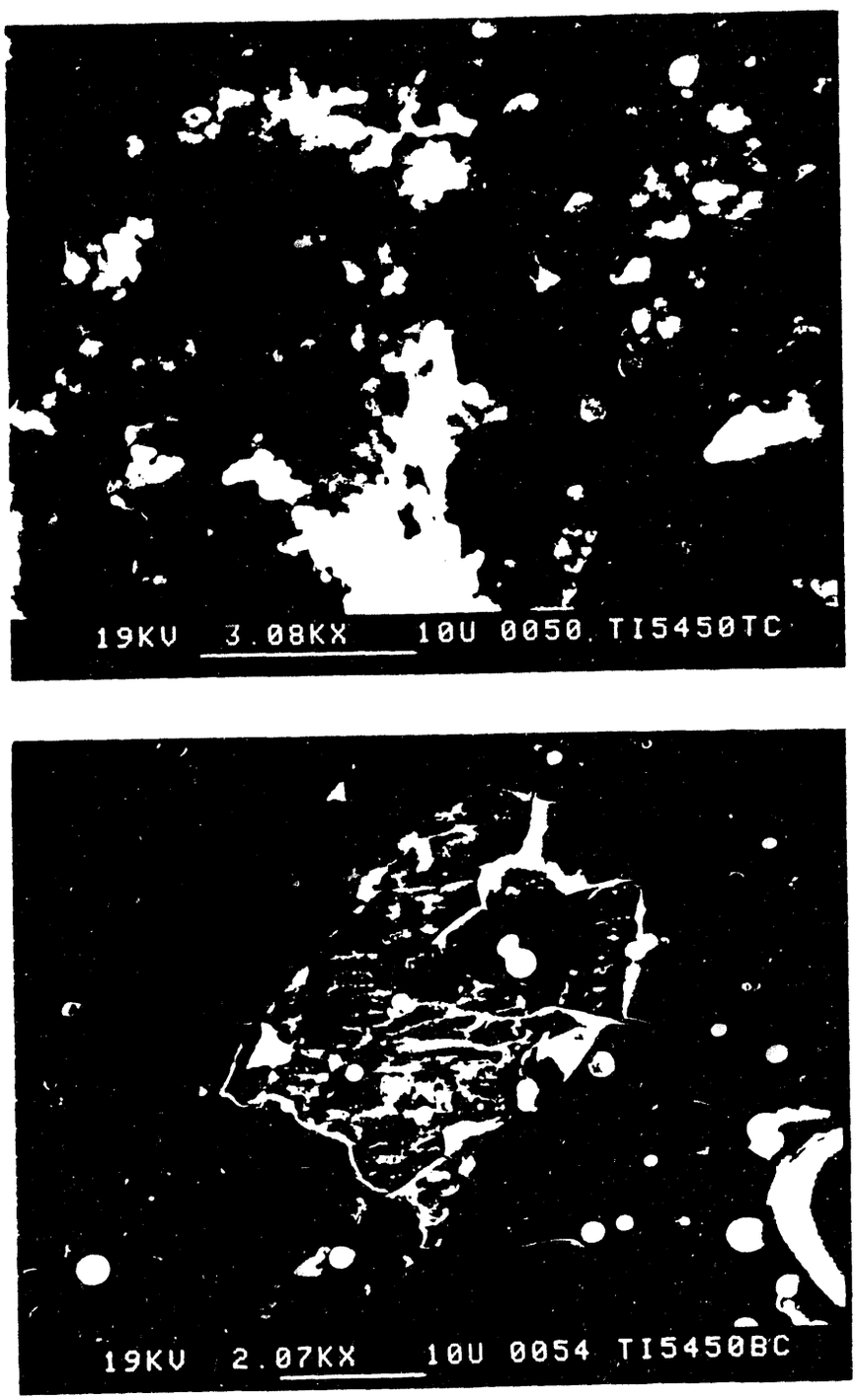

Figure 14. (a) Carbon Deposit on Top Titanium Coupon after 5 Hour Reaction at 450 °C, (b) Carbon Deposit on Bottom Titanium Coupon under the Same Condition.

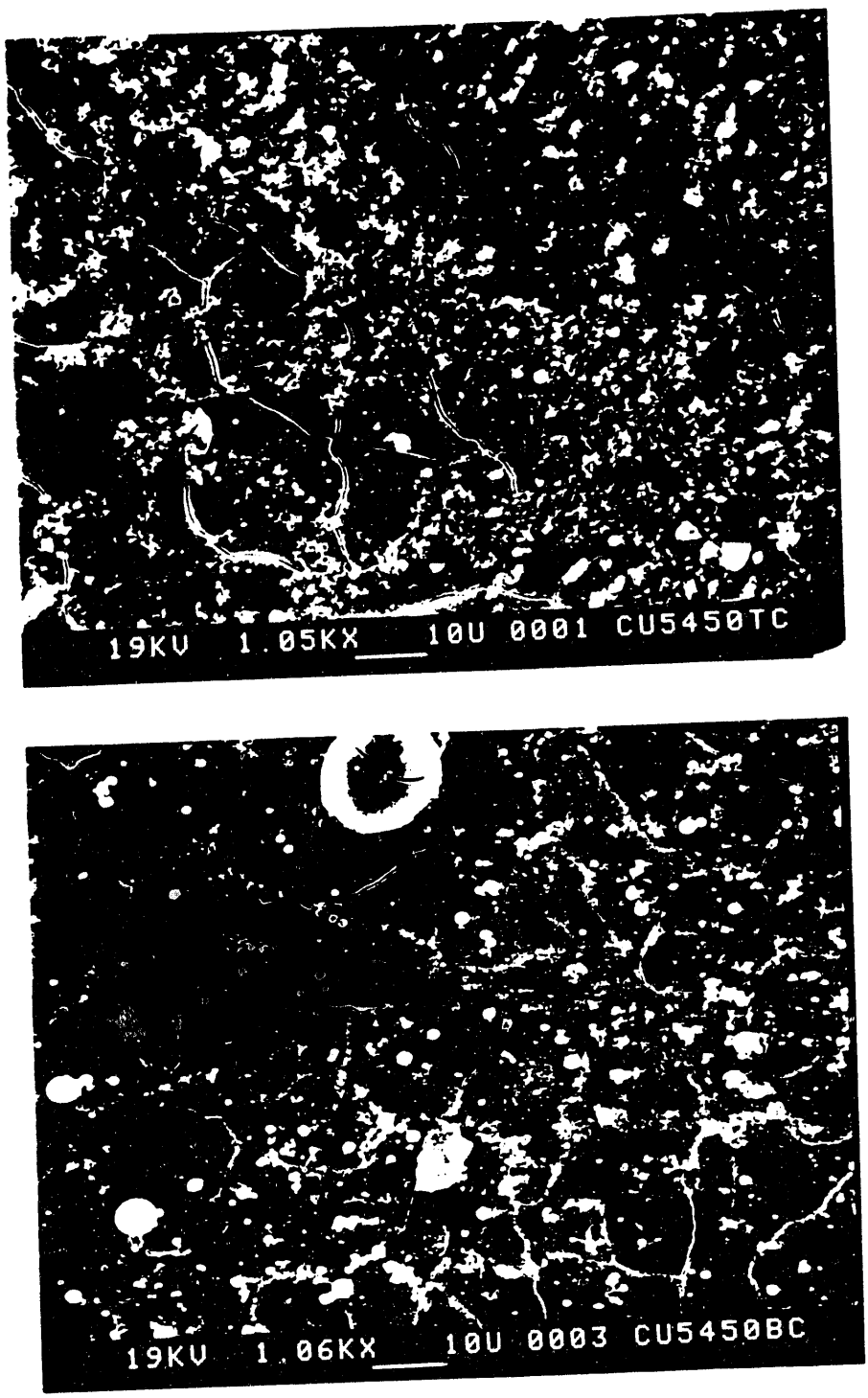

Figure 15. (a) Carbon Deposit on Top Copper Coupon after 5 Hour Reaction at 450 °C, (b) Carbon Deposit on Bottom Copper Coupon under the Same Condition.

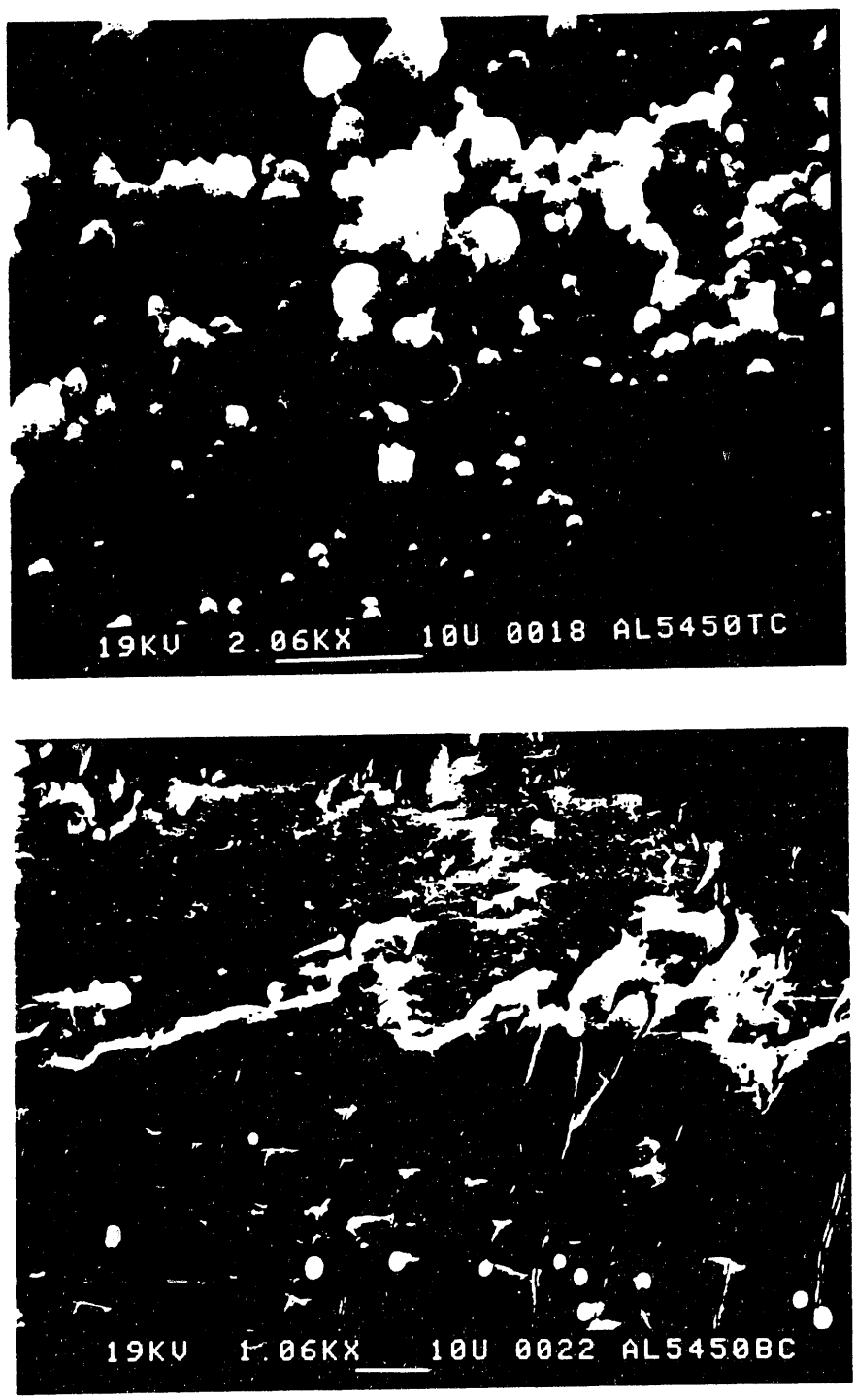

Figure 16. (a) Carbon Deposit on Top Aluminum Coupon after 5 Hour Reaction at 450 °C, (b) Carbon Deposit onBottom Aluminum Coupon under the Same Condition.

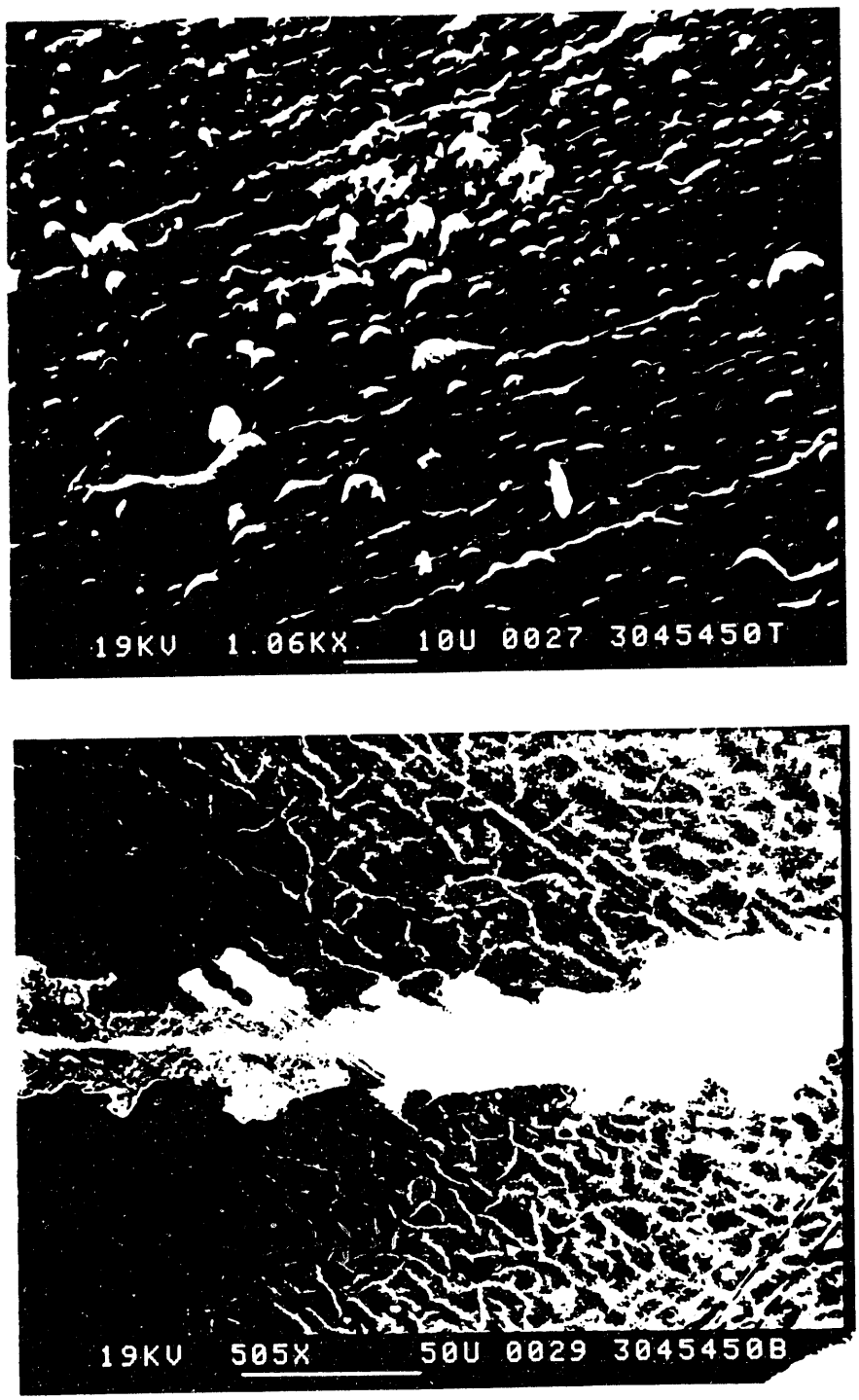

Figure 17. (a) Carbon Deposit on Top 304 Stainless Steel Coupon after 5 Hour Reaction at 450 °C, (b) Same Condition, on Bottom 304 Stainless Steel Coupon.

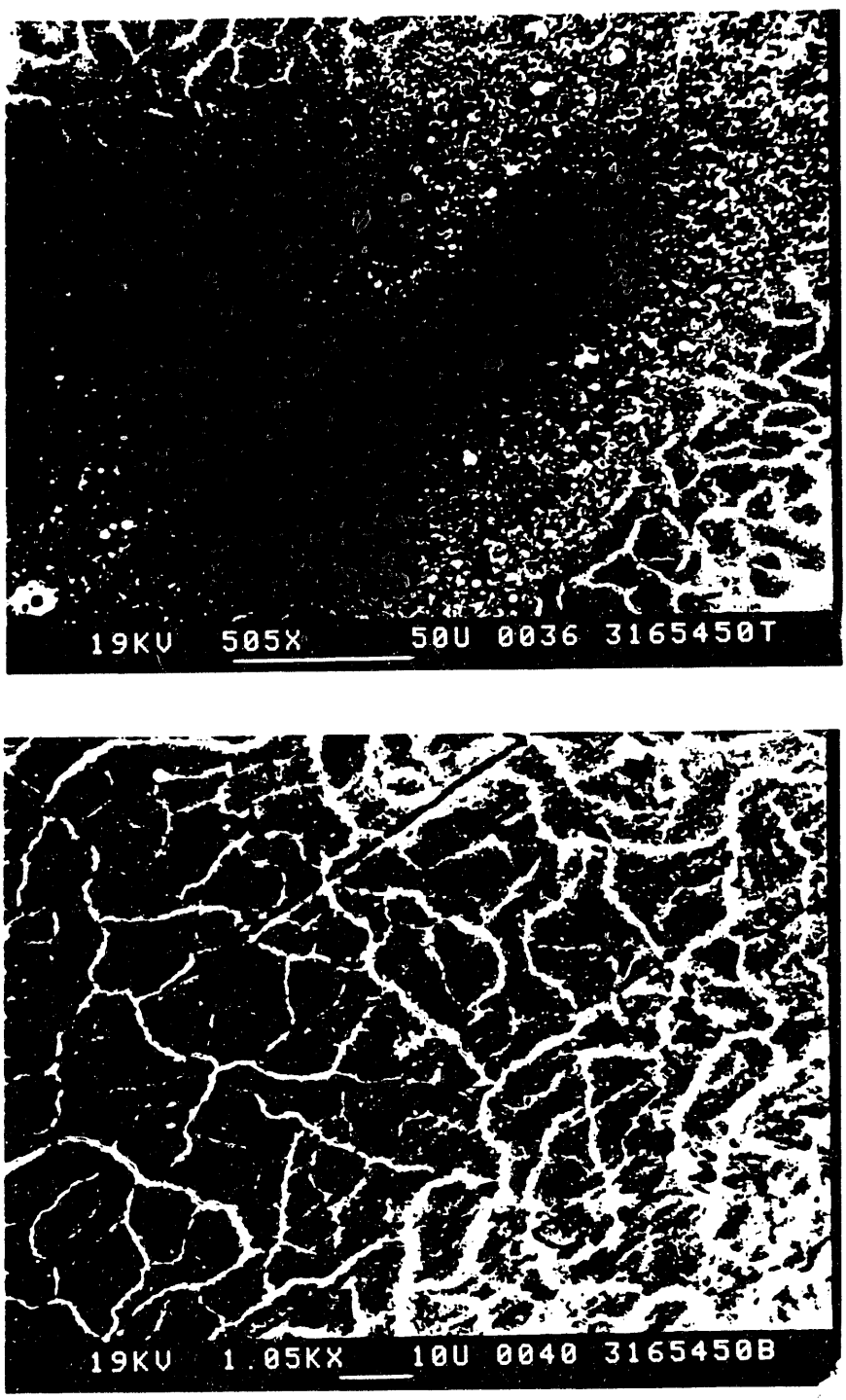

Figure 18. (a) Carbon Deposit on Top 316 Stainless Steel Coupon after 5 Hour Reaction at 450 °C, (b) Same Condition, on Bottom 316 Stainless Steel Coupon.

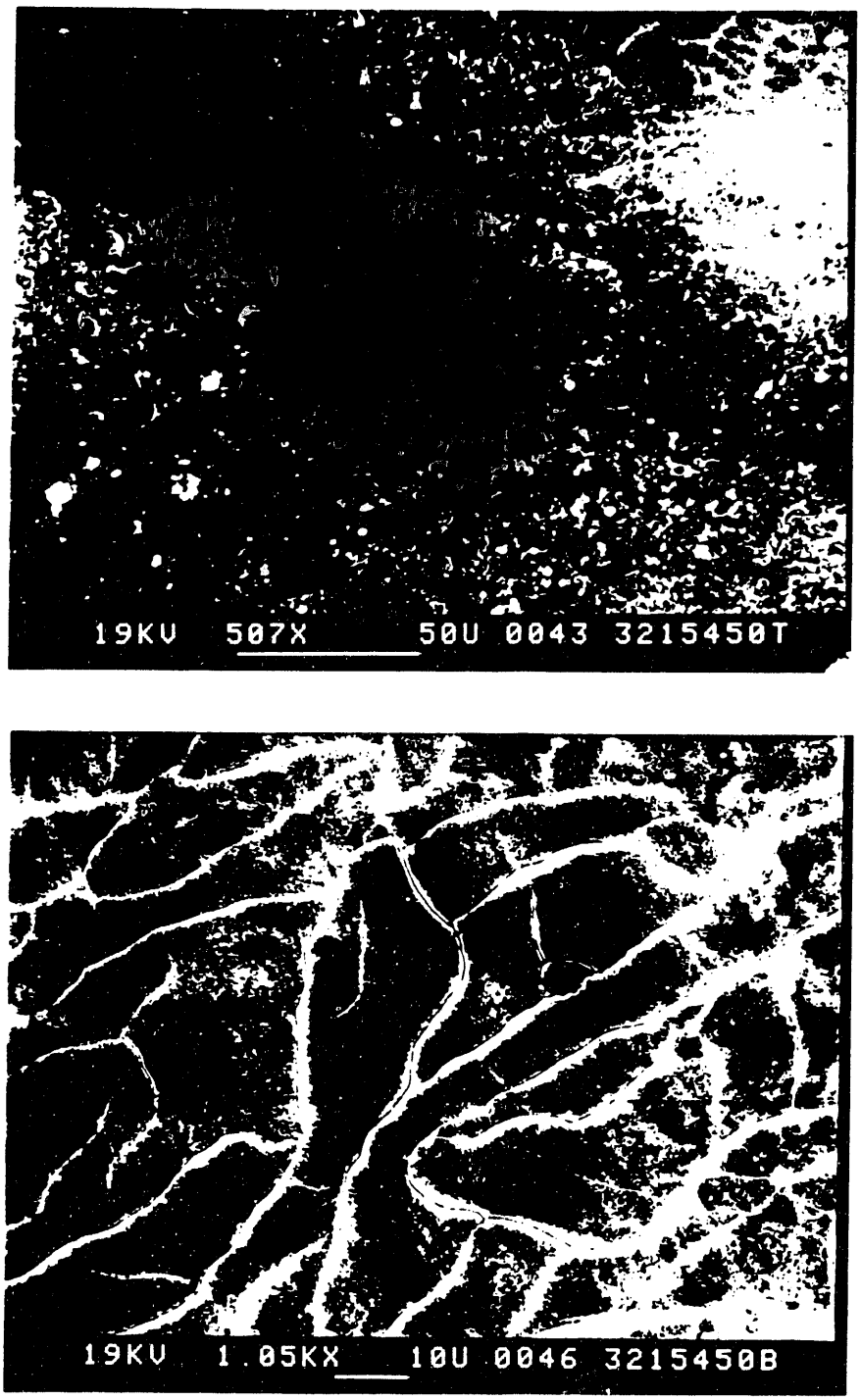

Figure 19. (a) Carbon Deposit on Top 321 Stainless Steel Coupon after 5 Hour Reaction at 450 °C, (b) Same Condition, on Bottom 321 Stainless Steel Coupon.

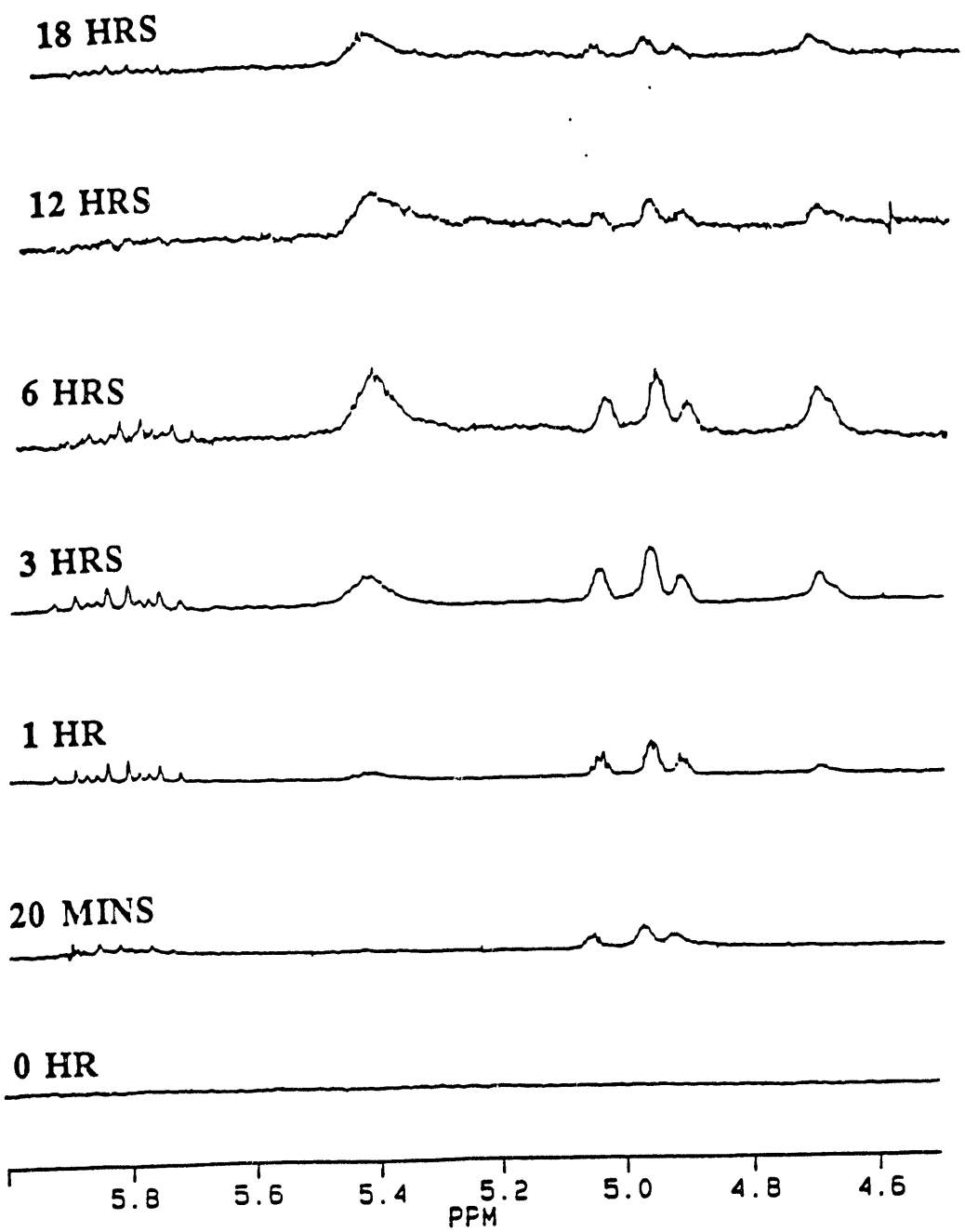

Figure 20. Scale expanded ^{1}H NMR spectra in the olefinic region of neat dodecane thermally stressed for the times indicated under air at 425° C.

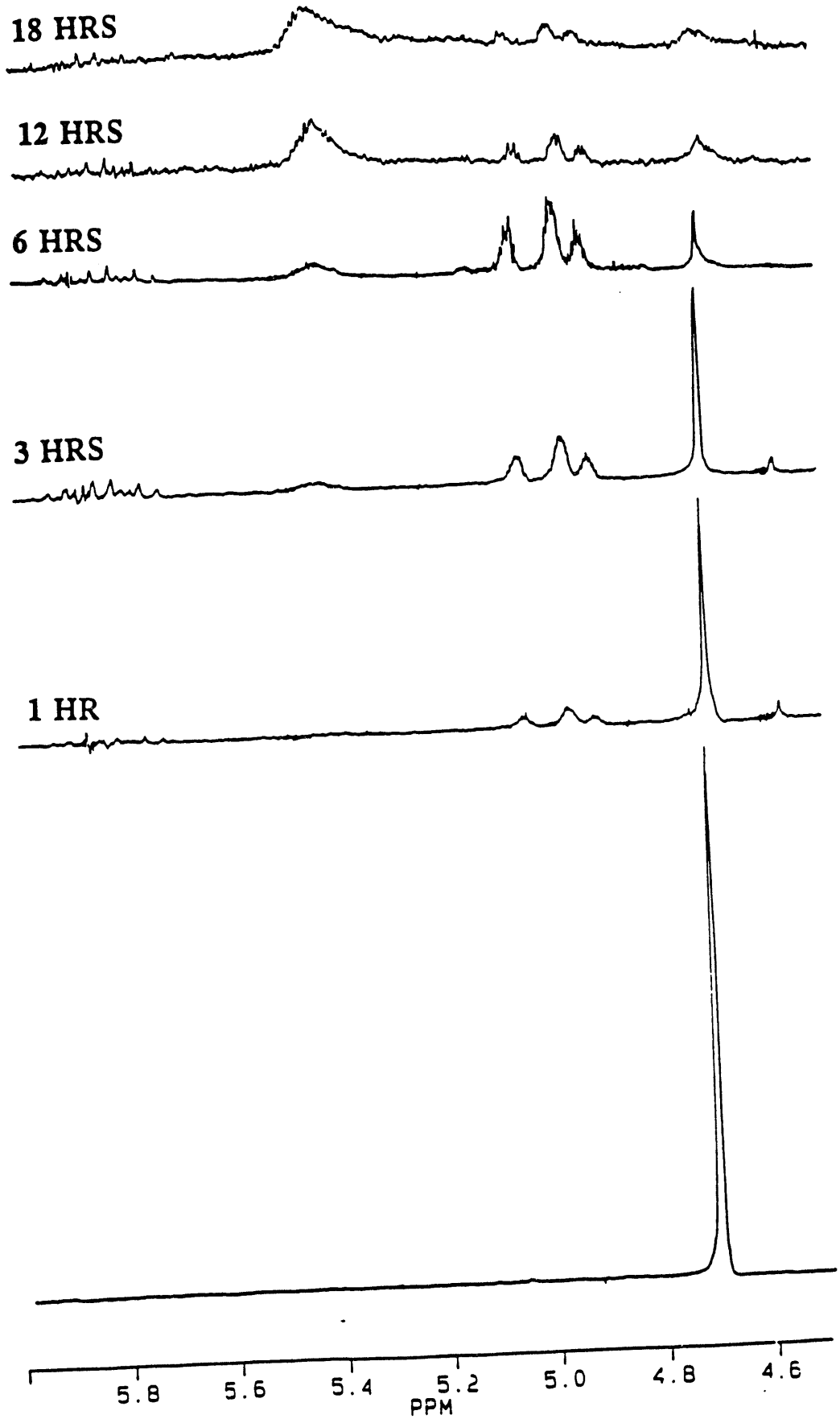

Figure 21. Scale expanded ^{1}H NMR spectra in the olefinic region of dodecane containing 5% benzyl alcohol thermally stressed for times indicated over air at 425°C.

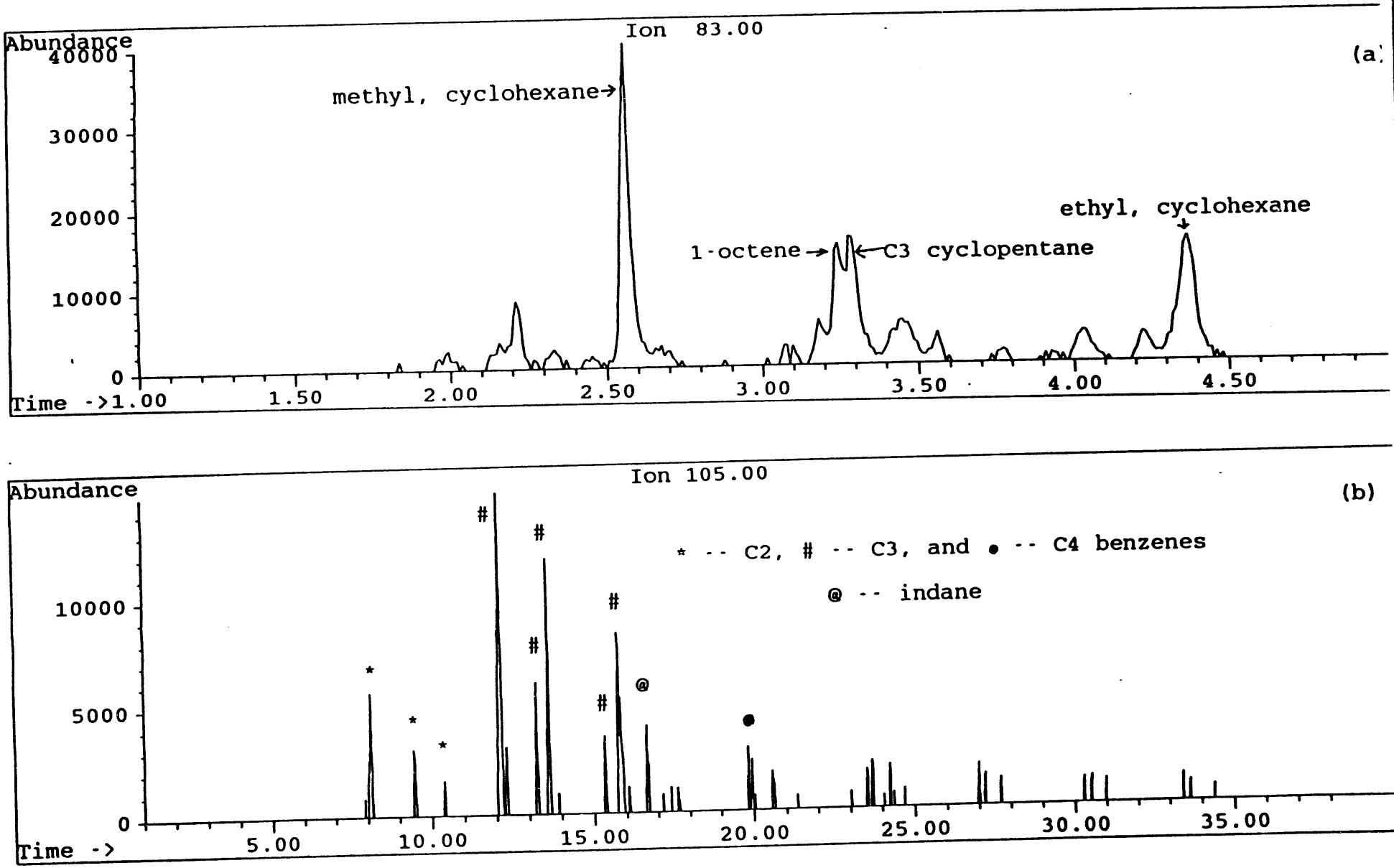

Figure 22. Selective ion chromatograms of (a) m/z 83 and (b) m/z 105 from GC/MS analyses of pure dodecane after thermal stressing at 425°C under 100 psi air for 6h.

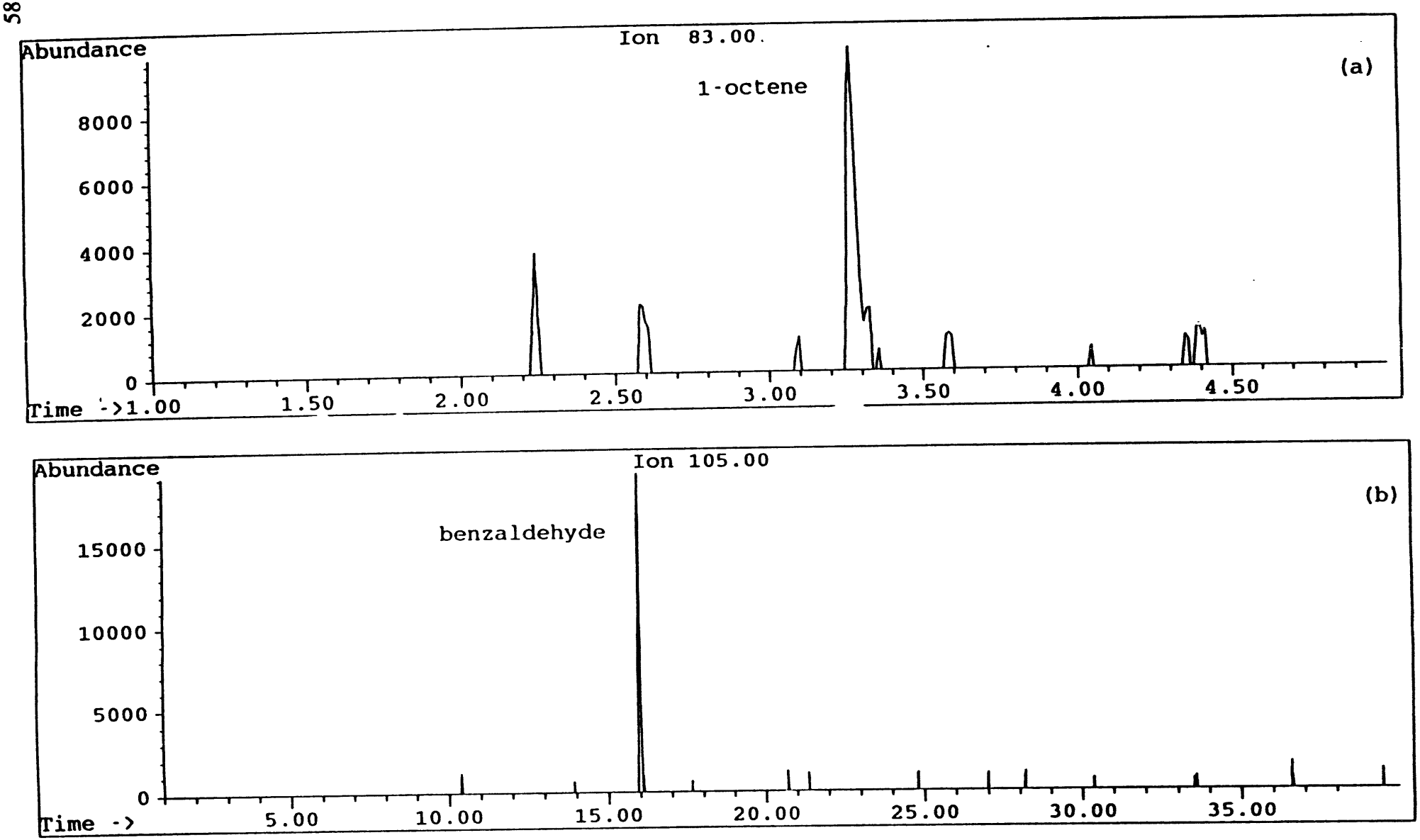

Figure 23. Selective ion chromatograms of (a) m/z 83 and (b) m/z 105 from GC/MS analyses of dodecane containing 5% benzyl alcohol after thermal stressing at 425°C under 100 psi air for 6h.

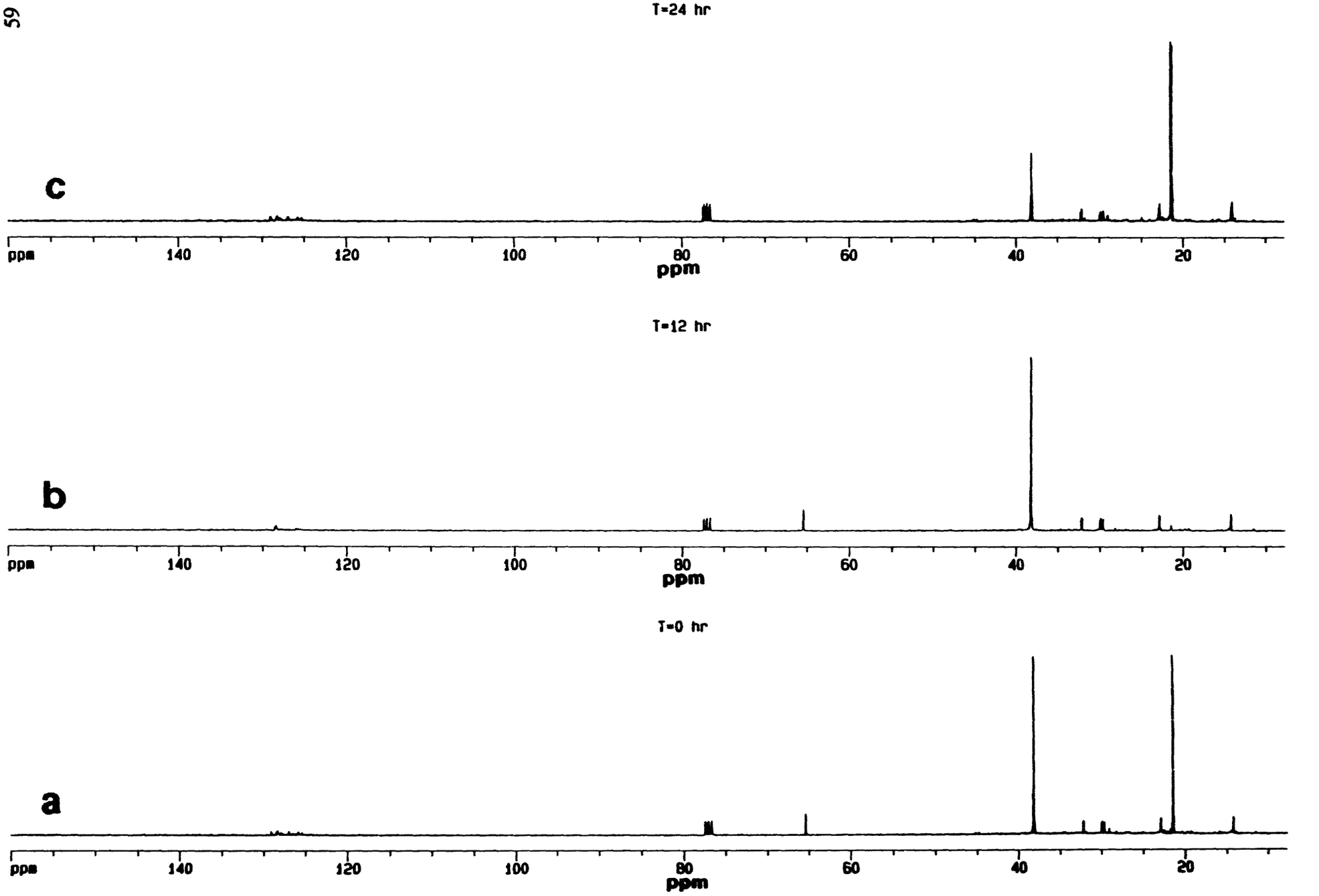

Figure 24. ^{13}C Inverse-Gated NMR Spectra Sampled of the Thermally Stressed Jet A-1 Fuel Mixture Containing Added ^{13}C-Labeled Bibenzyl and Benzyl Alcohol, (a) 0 hours, (b)12 hours, and (c) 24 hours.

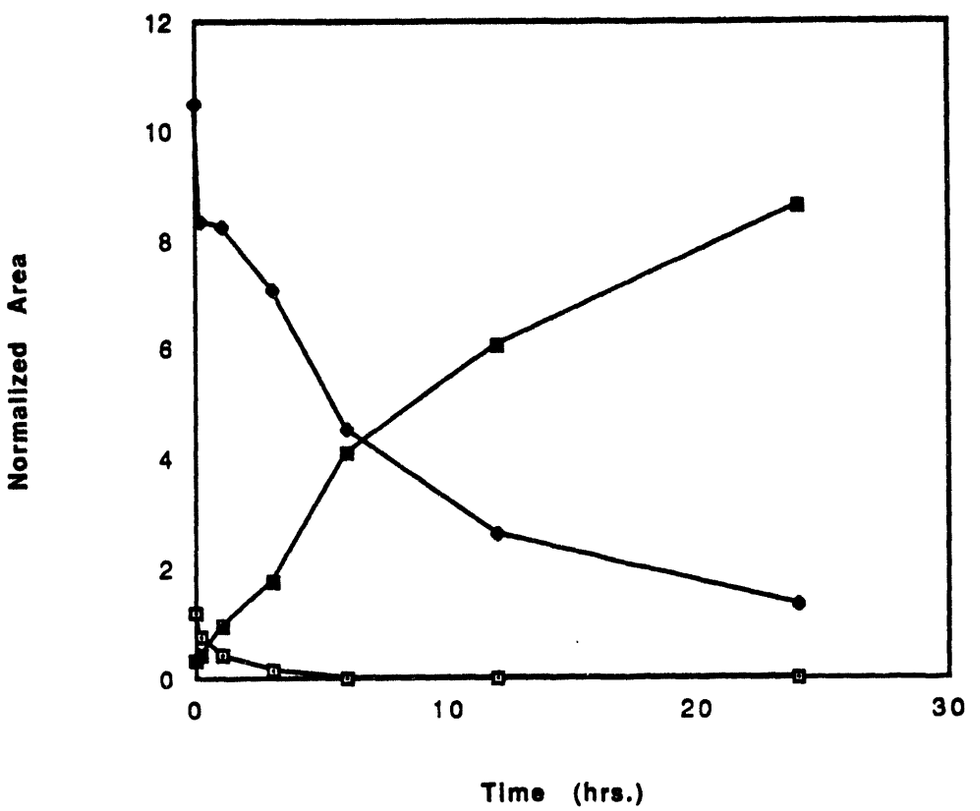

Figure 25. Plot of Relative Area versus Heating Time for the C-2, ^{13}C-Labeled Carbons of Benzyl Alcohol, Bibenzyl, and Toluene.

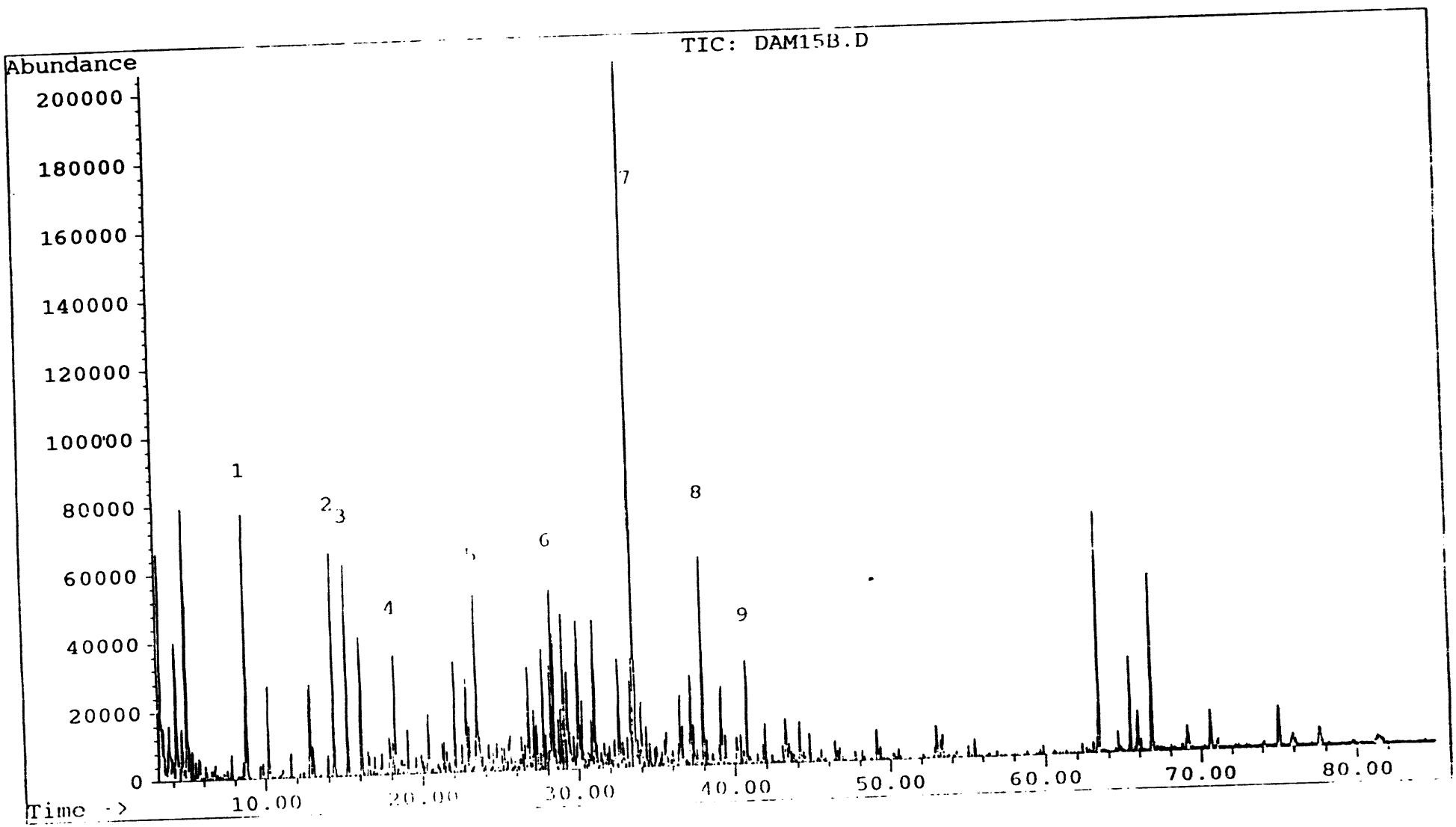

Figure 27. TIC of hydrogenated dammar resin — 450°C 20 minutes.

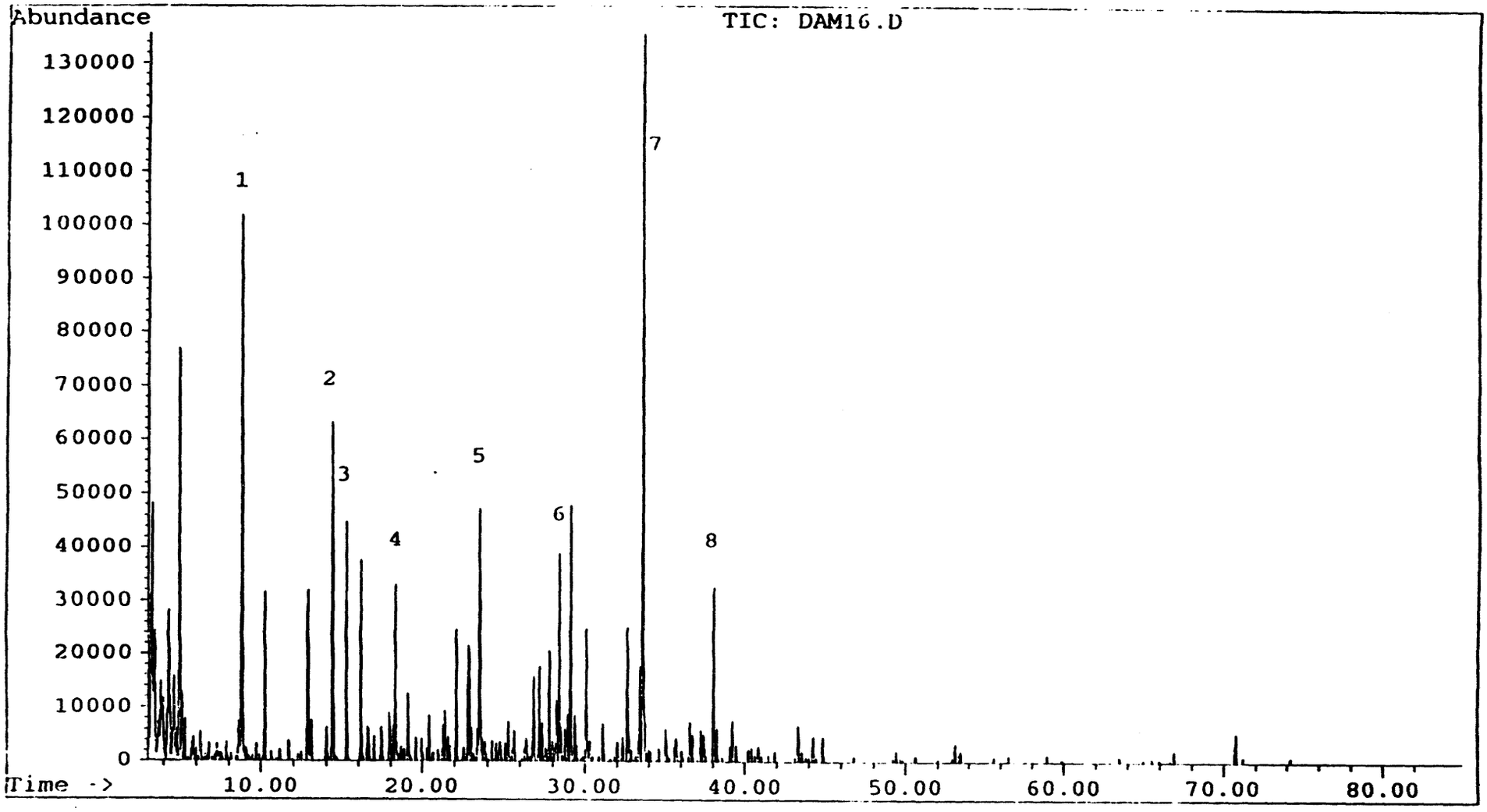

Figure 28. TIC of hydrogenated dammar resin — 450°C 40 minutes.

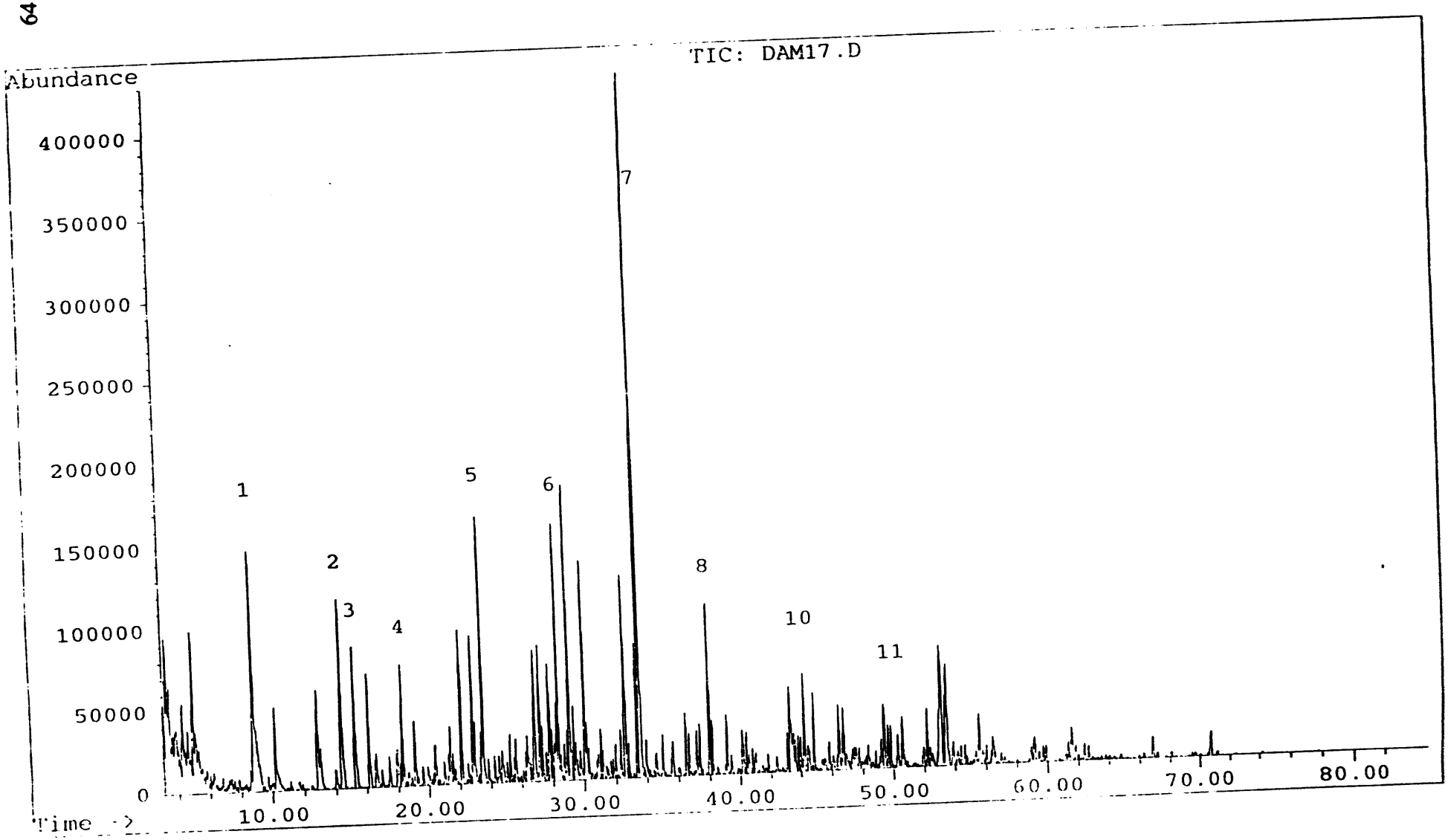

Figure 29. TIC of hydrogenated dammar resin — 450°C 60 minutes.

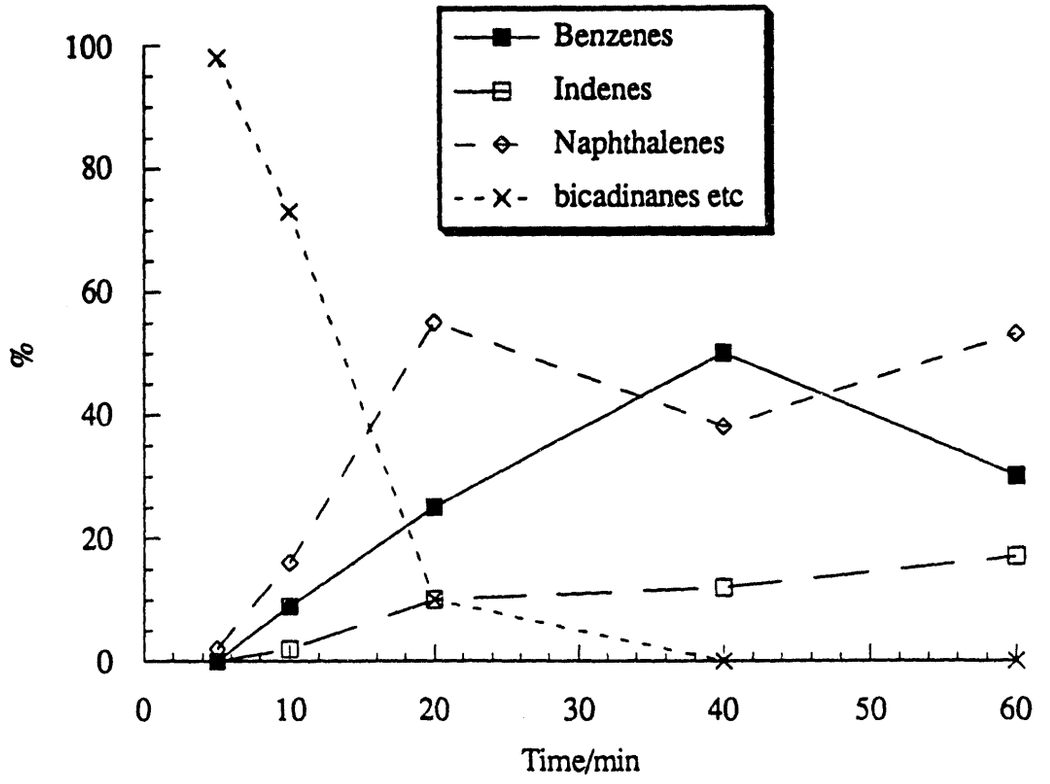

Figure 30. Hydrogenated dammar resin products vs time at 450°C.

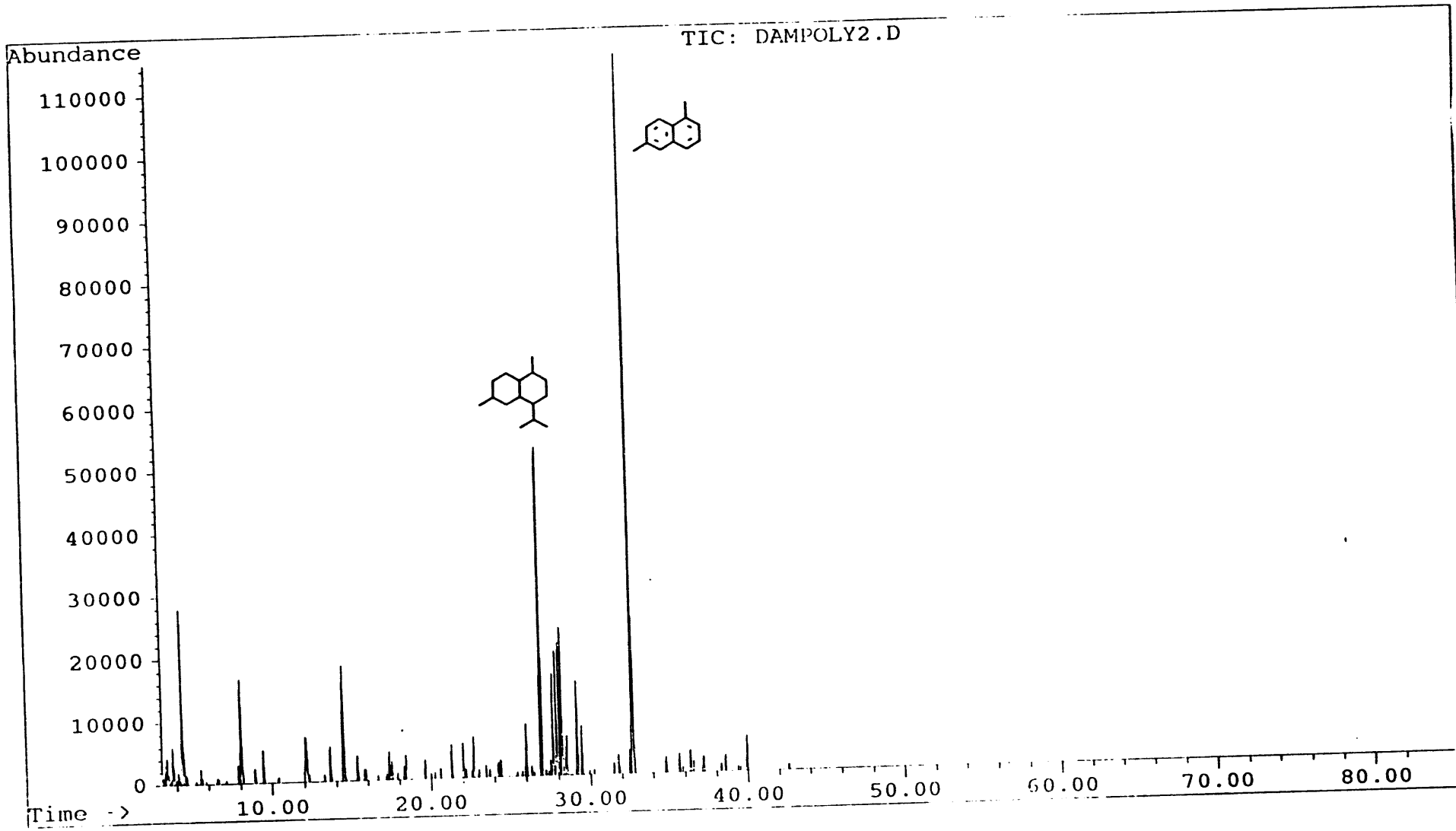

Figure 31. TIC of methanol insoluble fraction of dammar — 450°C 60 minutes.

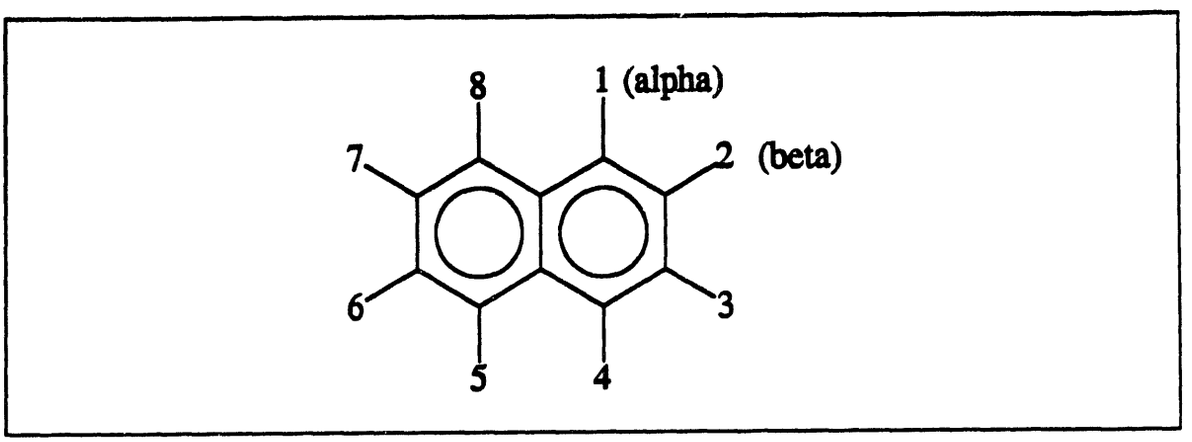

Figure 32. Carbon Numbering and Naming Conventions for Naphthalene.

APPENDIX III

SCHEMES

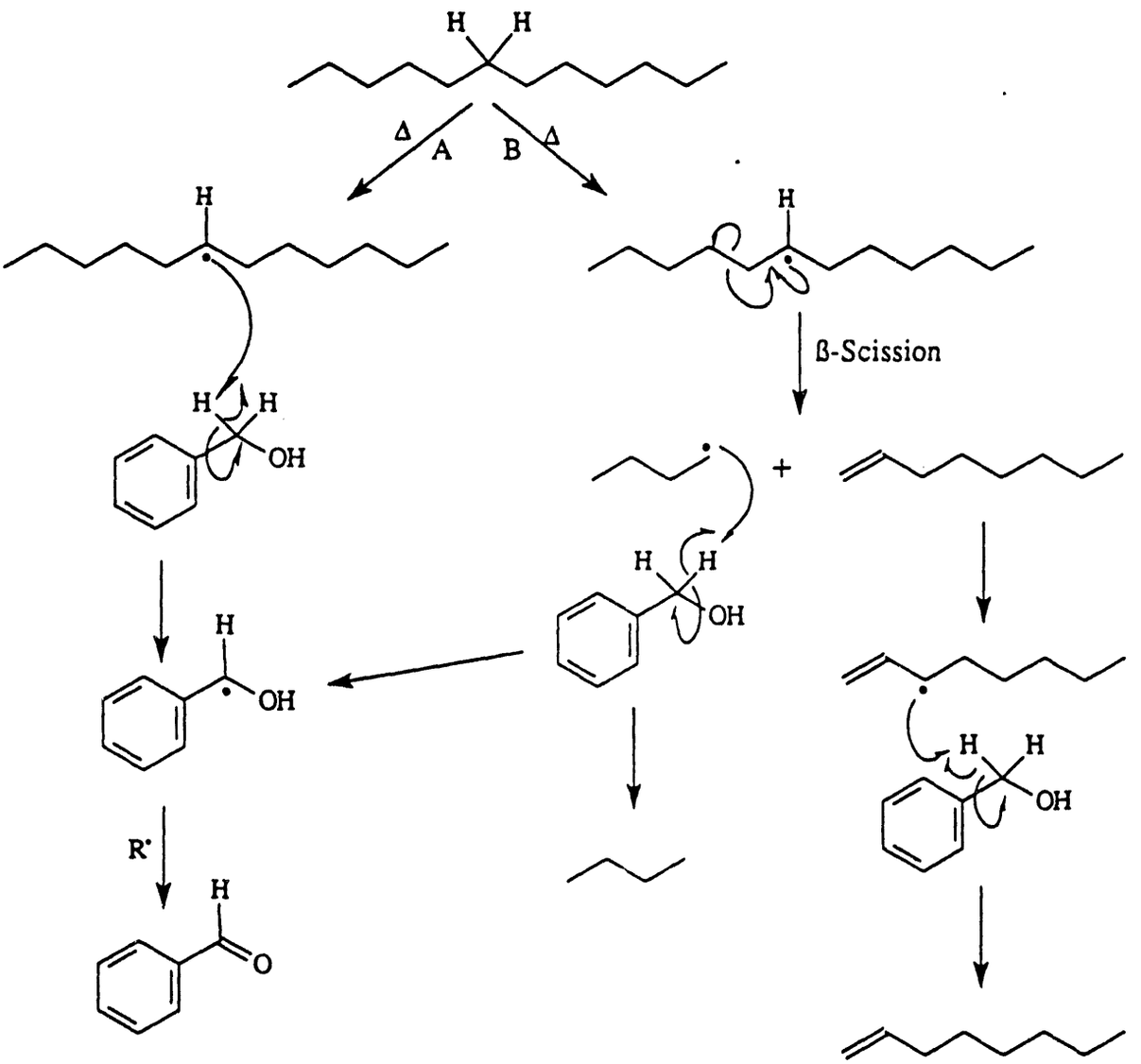

SCHEME I

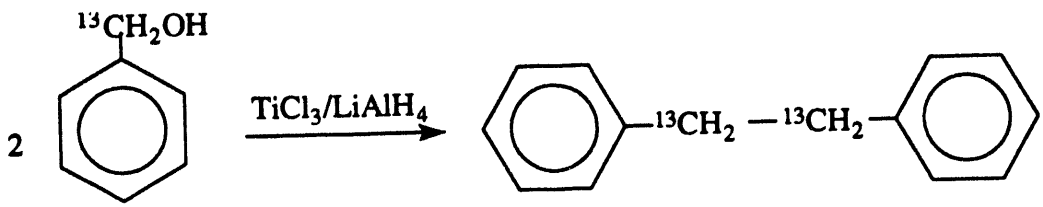

Scheme II

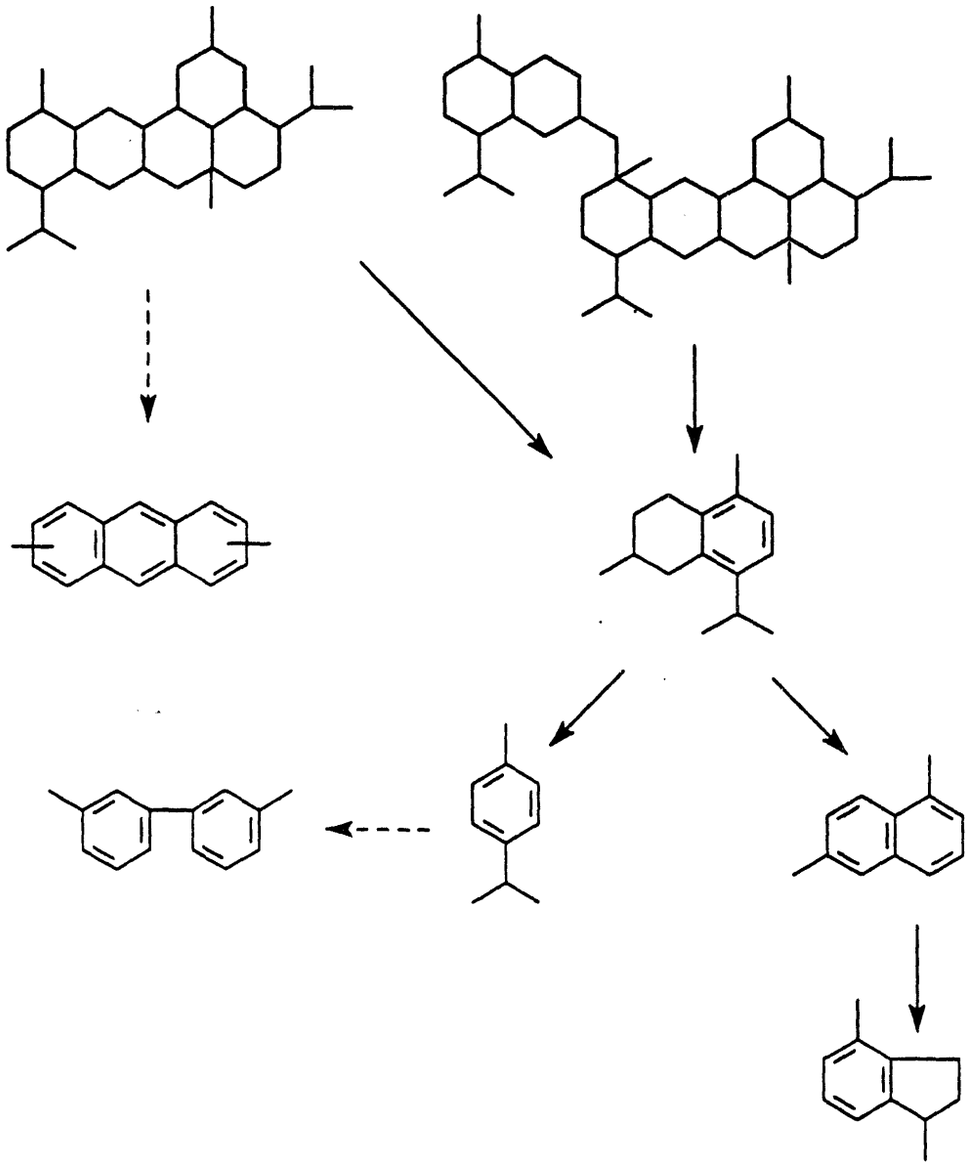

Scheme III. Possible reaction pathway of dimers and trimers of cadinene in dammar

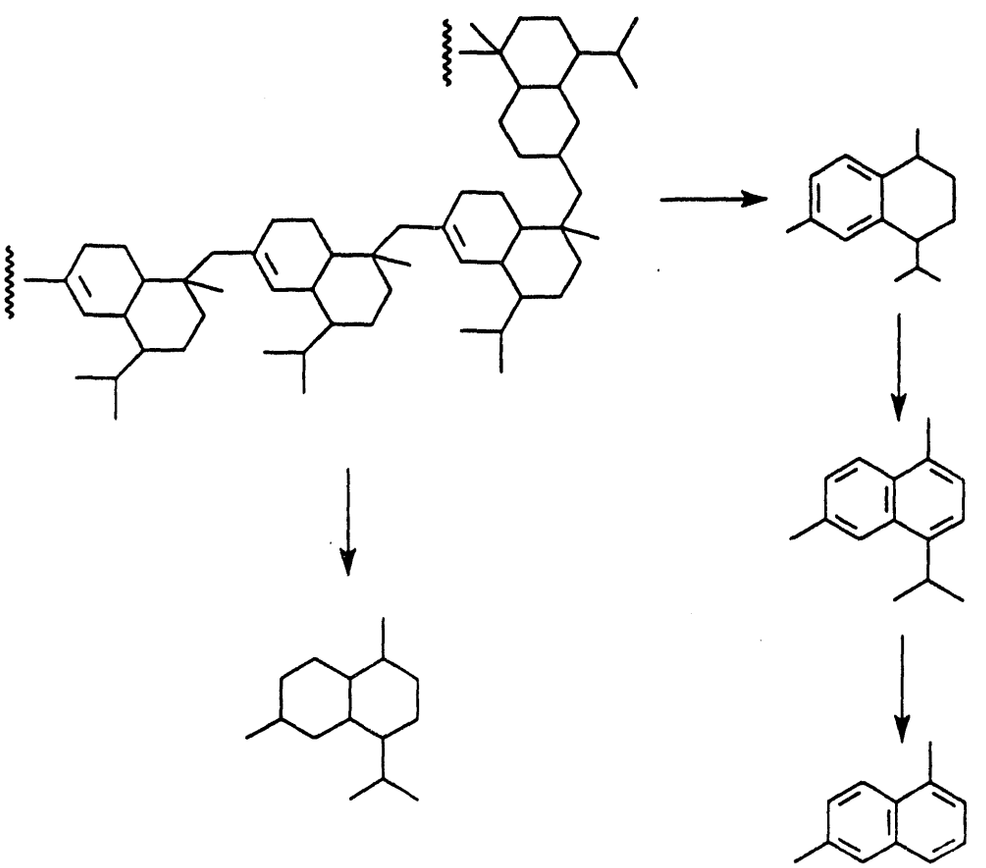

Scheme IV. Possible reaction pathway of polymeric component of dammar resin.

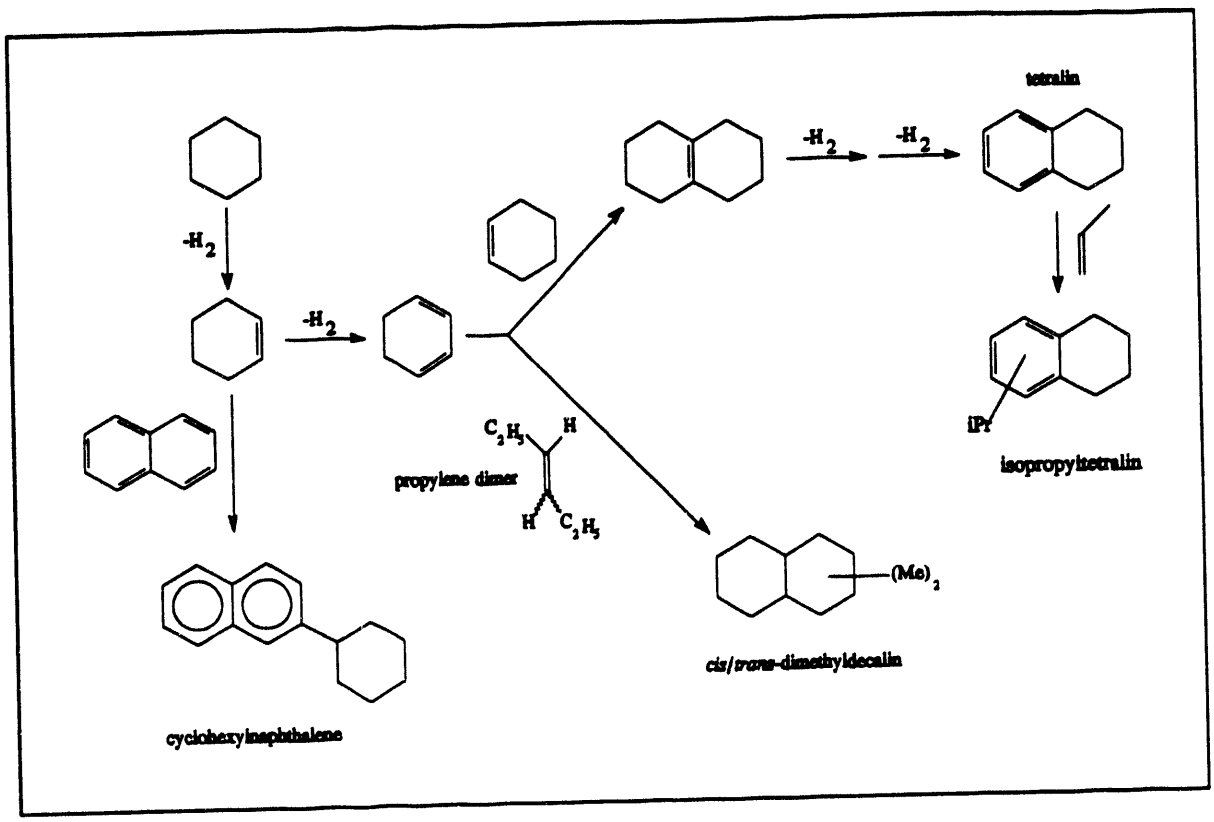

Scheme V. Proposed Scheme for Side Reactions of Cyclohexane Catalyzed by Mordenite.

APPENDIX IV

An unfortunate error occurred in the production of the previous quarterly report (92PC92104-TPR-5). After the report was printed and distributed, it was discovered that most copies were missing Section 2. Carbonaceous Deposit Formation on Metal Foils from thermal Stressing of n-Dodecane, contributed by Jun Li and Semih Eser . Therefore that section is being reprinted here.

2. Carbonaceous Deposit Formation on Metal Foils from Thermal Stressing of n-Dodecane (Contributed by Jun Li and Semih Eser)

Introduction

Previous study showed that the chemical composition of a metal surface (in the form of TEM grids and metal wires) as well as the types of reactants had a significant effect on carbon deposit formation during thermal stressing of Jet A and *n*-dodecane [1, 2]. This work continues the study of the surface effects in deposit formation. Instead of grids and wires, pure metal and stainless steel foils are used as substrates. Morphologies of the carbonaceous deposits generated on foil surface from *n*-dodecane at 450 °C for 1, 3 and 5 hours are studied with SEM.

Experimental

Thermal stressing of *n*-dodecane (Aldrich Chemical, > 99 %) was conducted isothermally in 20 mL stainless steel (316) tubing bomb reactors heated in a fluidized sand bath. A 5 mL sample was used for all the tests. The sample was deoxygenated by repetitive pressurization and purging (at least 5 times) with UHP nitrogen, and left with 0.69 MPa (100 psi) UHP N_2 as the initial pressure. At the end of the reaction, the reactor was quenched with cold water.

Ni, Cu, Al, Ti, and stainless steels 304 (Fe / Cr 18 / Ni 10), 316 (Fe / Cr 18 / Ni 8 / Mo 3), and 321 (Fe / Cr 18 / Ni 8 / Ti) foils were used as the substrate surface. The foils were 0.05 mm thick, except Cu foils which had a thickness of 0.025 mm. They were cut into coupons of 5 mm wide, and 10, 15, 20 and 30 mm long. The coupons were cleaned with acetone in an ultrasonic bath for 20 minutes, then dried and weighed. For each run, two coupons (5x10 and 5x20 mm) were hung on top of the reactor just below the reducer by a fine aluminum wire, and another two coupons (5x15 and 5x30 mm) were placed at the bottom of the reactor. To minimize the possible catalytic effects on deposit formation by the reactor walls, a quartz tube with a "fitting" size (14x16x64 mm) was placed inside the tubing bomb reactor to serve as an inert liner. After the reaction, coupons deposited with carbonaceous materials were rinsed with hexane, dried and weighed. Carbon morphologies were studied with an ISI ABT SX-40A electron microscope in the Materials Characterization Laboratory (MCL) at Penn State.

Observations and Discussion

1. Carbon deposition on nickel surface. A clean Ni foil consists of a rough side with numerous metal mounds ranging from 1–10 μm and a polished side with the mounds

being leveled. After 1 hour thermal stressing, there is no particulate deposit visible on either side of the Ni coupons; only some surface discoloration becomes noticeable. However, after 3 hours thermal stressing, heavy particulate carbon deposits were observed on both the top and bottom coupon surfaces. These particulates seem to bear the shape of the rough substrate surface. For the top coupon, they are surrounded by another kind of much smaller particulate deposits (Figure 31a), and for the bottom coupon, the large particulates usually encapsulate a number of smaller particles (Figure 31b). Also observed with the top coupon is the formation of numerous deposits rings with diameters of about 50 μm on deposit surface. As will be seen later, the formation of the rings on deposit surface is probably the only observed feature that is common to all the metal surfaces.

A filamentous carbon deposit is observed on Ni coupon which is placed at the bottom of the reactor after 5 hours of thermal stressing. The filaments are up to 5 μm long and 0.5 μm wide with Ni particles placed on their tips which are of the same size as the respective filaments (Figure 32a). The filamentous carbon is seen to be concentrated at one end of the coupon, while at the other end of the same coupon, deposit is seen to be particulate. Carbon deposit layer on top Ni coupons after 5 hours reaction is porous. This deposit consists of aggregates of small carbon particles (2 μm diameter) with a low degree of coalescence (usually only two to three particles coalesced, see Figure 32b).

2. Carbon deposition on copper surface. Copper surface is initially more reactive than Ni surface (or, probably, the induction period for deposition on copper surface is shorter). After 1 hour of reaction, a fibrous deposit is found both on top and bottom coupon surface (Figure 33). This kind of deposit is somewhat different from the classical filamentous carbon in that it does not have a metal particle on the tip of the deposit filament. These small fiber deposits are scattered somewhat randomly on Cu coupon. After 3 hours of reaction, the deposits appear in the form of rings on the surface (Figure 34a) and bulky deposits in the form of circles (200 μm in diameter). Deposit "particles" coalesced mostly along the perimeter of the ring (Figure 34b). It can also be seen that each ring contains bright tip(s) (carbonaceous material not metal particles) somewhere along the perimeter closing itself almost perfectly with a diameter of about 40–50 μm. It is not clear why these deposits, which appear to have grown on the surface conform to a ring shape.

After 5 hours of reaction, these rings have grown to an open diameter of 100–200 μm (Figure 35a). A closer look shows that these rings grow from coalescence of spherical particles (Figure 35b). Deposit layer also cracks into circular strips which peel off the substrate surface. In contrast to the rings, monticular carbon deposits are also observed,

which has a carbon particle growing out of the center of a loose ring to form a deposit mound.

3. Carbon Deposition on Aluminum and Titanium Surfaces. There are barely any carbon deposits formed on Al coupons after 1 hour reaction. However, after 3 hour reaction, both the top and bottom coupon surfaces are covered by bulk deposit layers. Deposits on top coupons are denser than those on bottom coupon surface, with deposit mound growing out of the bulk layer. One unique phenomenon for deposition on Al surface is that the bulk carbon layer on either top or bottom surfaces cracks quite evenly into straight strips (about 50 μm wide, Figure 36). These strips are likely to have been formed during the reaction process as opposed to the later processing stage because these strips are consistently observed for different reaction runs. Moreover, there are also numerous rings similar to those formed on Cu surface on the bulk carbon layer. These rings may cross the strips.

After 5 hours reaction, morphologies of the deposit do not seem to change too much, only that the strips become wider (Figure 37a). Rings are also formed by the aggregation of numerous coalesced spherical particles (Figure 37b).

For Ti coupons, after 3 hours reaction, thick bulky carbon layer is seen on both top and bottom coupon surface. Deposit particles on Ti surface have a high mobility, thus forming the highly coalesced bulk layer (Figure 38a). This deposit layer sticks to the substrate surface well so that it does not peel off the surface easily. It also cracks, but, unlike on Cu and Al surfaces, it cracks randomly into small fragments (Figure 38b). After 5 hours reaction, the morphologies of the deposit are similar, only that a lot of rings, most of them circular, some oval, are seen again on the surface of the bulky layer.

4. Carbon Deposition on Stainless Steel Surfaces. Three different stainless steel foils (304, 316, 321) were used in the experiments. No deposits were seen on any of the surface after 1 hour reaction. Those coupons deposited with carbon after three hour reaction were at first cleaned by acetone in an ultrasonic bath for 20 minutes. It is found that deposits cleaned in this way peel off the 316 and 321 coupons. Later this cleaning procedure was changed to just rinsing the coupons with hexane.

After 3 hours reaction, a lot of small carbon particles (up to 5 μm diameter) can be seen scattered randomly on the bottom 304 coupon surface (Figure 39). This probably reflects the initial deposition process on 304 surface. A solid carbon particle or droplet hits the bare metal surface, with no preference to any particular sites. Due to the low mobility of the particle on the surface or high wetability of the surface to the particle, this particle collapses and eventually forms a deposit ring. After 5 hours reaction, the metal surface is covered by bulky carbon layers. In this case, carbon deposits on top are denser

than those on bottom coupon surface. As have been seen on other metal surfaces, there are rings on the carbon layer.

After 5 hours reaction, particulate carbon deposits are seen on the bottom 316 coupons, which resemble those on bottom Ni coupon surface. The initial deposition process is unknown because the deposits on coupon surface after 3 hours reaction have peeled off after ultrasonic cleaning.

On the 321 coupon surface after 5 hours reaction, a bulky carbon layer covers the metal surface. Carbon layer on bottom coupon cracks into straight strips similar to those found on Al surface (Figure 40a). Oval carbon rings similar to those on Ti surface are also seen on top of 321 coupon surface (Figure 40b).

5. Discussion. Thermal stressing experiments using metal foils have shown new features relating to both the initial and subsequent deposit formation process. An important finding is the formation of filamentous carbon on a nickel surface under our jet fuel thermal stressing condition. Filamentous carbon formation on Group VIII metals such as Ni, Fe, Co has been widely studied (reviewed in [3]). However, most of the studies are carried out under reduced pressure with light aliphatic (up to C_4) or aromatic hydrocarbon reactants. Although not always necessary, H_2 is often introduced into the system, presumably to keep the surface clean to promote the formation of filaments. These conditions are dramatically different from our tubing bomb experiments. There has been no report on filamentous carbon formation from aliphatics as large as dodecane. This finding strongly suggests that the initial deposit formation from jet fuel range hydrocarbons such as dodecane is catalyzed by the presence of a nickel surface.

Initially, deposits formed on copper surface are fibrous. This may also relate to the catalytic effects of copper. The rate of deposit formation on copper surface is even higher than on the nickel surface. This may be due to the dissolved oxygen in the fuel or simply a shorter induction period.

The difference of the initial deposition among three stainless steel foils can not be identified at the moment. There is no apparent catalysis of initial deposition by different stainless steels (304, 316, 321). Carbon particles or droplets simply deposit on to the bare metal surface without any preferences. There are, however, some differences of the deposit morphologies on different stainless steel surfaces. Deposits on a 316 surface have a similar structure as on a nickel surface, while deposits on a 321 surface have a similar straight strip structure as on aluminum surface and the rings bear a shape similar to those on a titanium surface. Clearly, the initial deposition process on different stainless steel surfaces should be further studied.

The results from the foil experiments are consistent with the previous metal grid study. As suggested before, nickel surface can strongly catalyze the deposit formation. Copper surface also has some catalytic effects. The stainless steel surface seems to be inert in catalyzing the deposit formation from fuels such as dodecane.

Another feature that is almost common to all the metal surface studied is the formation of rings on the deposit layer. This is probably a process related to the subsequent deposit growth. Generally, more rings are formed on top of metal coupons. And those on the copper foil have a more regular shape than on the other metal surfaces. In all the cases, these rings have a diameter of about 50–200 μm depending upon the reaction time and are formed by the aggregation of coalesced spheres along the perimeter of the rings. The mechanism of the formation of these rings are intriguing. It is most likely related to the previously formed deposit surface because it is seen on almost all the deposit surface with different metals. Therefore, an understanding of the formation of rings on a deposit layer will certainly help to understand the growth mechanism of carbonaceous deposits.

Conclusions

Clear indications of both initial and subsequent deposit formation on different metal surface from dodecane thermal stressing have been identified. Initially, nickel surface can catalyze the deposition by forming filamentous carbon; copper surface probably can catalyze the deposition by forming fibrous carbon; a stainless steel surface, on the other hand, has no catalytic effects on deposit formation process. Eventually, the metal surface is covered by carbon layers with circular or oval rings on these carbon layers. This ring formation process is probably related to the steady-state growth of deposit on all the metal surface. The mechanism of ring formation is not understood currently.

References

1. H. H. Schobert, S. Eser, C. Song, P.G. Hatcher, P.M. Walsh, and M.M. Coleman, *Advanced Thermally Stable Jet Fuels*, Technical Progress Report, 92PC92104-TPR-1, 1993, p.18-23

2. J. Li, and S. Eser, Surface Effects on the Formation of Carbonaceous Deposits from Thermal Stressing of Jet Fuel and n-Dodecane, *21st Biennial Conference on Carbon, Extended Abstracts and Program,* June 13-18, 1993, p. 527-528

3. H. H. Schobert, S. Eser, C. Song, P.G. Hatcher, P.M. Walsh, and M.M. Coleman, *Advanced Thermally Stable Jet Fuels*, Technical Progress Report, 92PC92104-TPR-3, 1993, p.15-40

DATE
FILMED
9/19/94

END